# Hall D / GlueX
# Technical Construction Report

March 17, 2015

# Abstract

The Technical Construction Report describes the Hall D facility constructed as a part of the JLab 12 GeV Upgrade Project. The facility is dedicated to physics with linearly-polarized photon beam. Electron beam extracted from the CEBAF accelerator to the new Tagger Hall produces polarized photons by the coherent radiation. The photon beam is delivered to Hall D. The Hall D apparatus is optimized for light-meson spectroscopy - experiment GlueX. The main goal of GlueX is to search and map out the spectrum of light hybrid mesons with exotic quantum numbers.

M. Dugger, B. Ritchie and I. Senderovich
*Arizona State University, Tempe AZ 85281*

D. Fassouliotis, P. Ioannou, and Ch. Kourkoumelis
*University of Athens, Athens, Greece*

N.S. Jarvis, W. Levine, P. Mattione, W. McGinley, C. A. Meyer (GlueX spokesperson),
R. A. Schumacher, and M. Staib
*Carnegie Mellon University, Pittsburgh,PA 15213*

F. J. Klein, D. Sober, N. Sparks, and N. Walford
*Catholic University of America, Washington, D.C.*

D. Doughty
*Christopher Newport University (Newport News, VA)*

A. Barnes, R. Jones, J. McIntyre, F. Mokaya and B. Pratt
*University of Connecticut, Storrs, CT*

W. Boeglin, L. Guo, E. Pooser, and J. Reinhold
*Florida International University, Miami,FL*

H. Al Ghoul, V. Crede, P. Eugenio, A. Ostrovidov, and A. Tsaris
*Florida State University, Tallahassee,FL*

D. Ireland and K. Livingston
*University of Glasgow, Glasgow UK*

D. Bennett, J. Bennett, J. Frye, M. Lara, J. Leckey, R. Mitchell, K. Moriya, B. Schaefer and
M. Shepherd (GlueX Deputy Spokesperson),
*Indiana University, Bloomington,IN*

O. Chernyshov, A. Dolgolenko, A. Gerasimov, V. Goryachev, I. Larin, V. Matveev and
V. Tarasov
*ITEP Moscow, Moscow, Russia*

F. Barbosa, E. Chudakov (Hall D Leader), M. Dalton, A. Deur, J. Dudek, C. Cuevas,
H. Egiyan, S. Furletov, M. Ito, D. Lawrence, D. Mack, M. McCaughan, M. Pennington,
L. Pentchev, Y. Qiang, E. Smith, A. Somov, S. Taylor, T. Whitlatch, and B. Zihlmann,
*Jefferson Lab, Newport News, VA 23606*

R. Miskimen
*University of Massachusetts Amherst, Amherst, MA*

B. Guegan, J. Hardin, J. Stevens and M. Williams
*Massachusetts Institute of Technology, Cambridge, MA*

V. Berdnikov, G. Nigmatkulov, A. Ponosov, D. Romanov, S. Somov and I. Tolstukhin
*MEPHI, Moscow, Russia*

C. Salgado
*Norfolk State University, Norfolk, VA*

P. Ambrozewicz, A. Gasparian and R. Pedroni

*University of North Carolina A&T, A&T State, NC*

T. Black and L. Gan
*University of North Carolina, Wilmington, NC*

S. Dobbs, K. K. Seth, X. Ting and A. Tomaradze
*Northwestern University, Evanston, IL*

T. Beattie, G. Huber, G. Lolos, Z. Papandreou, E. Plummer, A. Semenov and I. Semenova
*University of Regina, Regina, Saskatchewan, Canada*

W. Brooks, H. Hakobyan, S. Kuleshov, O. Soto, A. Toro and I. Vega
*Santa Maria University, Valparaiso, Chile*

N. Gevorgyan, H. Hakobyan and V. Kakoyan
*Yerevan Physics Institute, Yervan, Armenia*

# Contents

# Chapter 1

# Overview

The Technical Construction Report describes the Hall D facility constructed as a part of the JLab 12 GeV Upgrade Project. The facility is dedicated to physics with linearly-polarized photon beam. Electron beam extracted from the CEBAF accelerator to the new Tagger Hall produces polarized photons by the coherent radiation. The photon beam is delivered to Hall D. The Hall D apparatus is optimized for light-meson spectroscopy - experiment GlueX. The main goal of GlueX is to search and map out the spectrum of light hybrid mesons with exotic quantum numbers.

## 1.1 Physics Motivation [1]

The primary motivation of the GlueX experiment is to search for, and ultimately study the pattern of gluonic excitations in the meson spectrum produced in $\gamma p$ collisions, in a mass range of 1.5-2.5 GeV/c$^2$. Recent lattice QCD calculations predict a rich spectrum of hybrid mesons that have both exotic and non-exotic $J^{PC}$ quantum numbers, corresponding to $q\bar{q}$ states ($q = u$, $d$, or $s$) coupled with a gluonic field.

### 1.1.1 Expectations for Exotic Hybrid Mesons

Lattice QCD calculations predict several nonets of exotic $J^{PC}$ quantum number states. The lightest supermultiplet of hybrid mesons contains four nonets with $J^{PC}$ quantum numbers $1^{--}$, $0^{-+}$, $1^{-+}$ and $2^{-+}$, where the $1^{-+}$ quantum numbers are exotic. In addition to the lowest mass states, the lattice calculations predict several nonets of excited hybrids. Those with exotic quantum numbers are $J^{PC} = 1^{-+}$, $J^{PC} = 0^{+-}$, and two nonets with $J^{PC} = 2^{+-}$. Several of the these states are discussed in Table 1.1. Also shown in the table are some of the possible decay modes for these mesons. While some of the final states are fairly simple, such as $\rho\pi$, $\omega\pi$ and $\eta'\pi$, most of them involve more complicated decays leading to several particles in the final state. Typical decays involve both charged particles and photons from the decays of $\pi^\circ$ and $\eta$ mesons. A primary goal of the GlueX detector is to be able exclusively reconstruct these final states with good efficiency and purity. This goal has been one of the primary drivers to the design of the experiment.

Not only do the lattice calculations predict the existence of hybrid mesons, but they also predict masses and nonet mixing angles. The mixing angles relate the amount of $s\bar{s}$ and $u\bar{u}+d\bar{d}$

---

[1] *SVN revision ID:* tcr_intro.tex 13927 2014-06-20 17:19:48Z cmeyer

Table 1.1: A compilation of exotic quantum number hybrid approximate masses and decay predictions. Masses are estimated from dynamical LQCD calculations with $M_\pi = 396$ MeV/$c^2$. (We consider $\eta$, $\eta'$, and $\omega$ to be stable final state particles.)

| | Approximate Mass (MeV) | $J^{PC}$ | Relevant Decays | Final States |
|---|---|---|---|---|
| $\pi_1$ | 1900 | $1^{-+}$ | $b_1\pi$, $\rho\pi$, $f_1\pi$, $a_1\eta$, $\eta'\pi$ | $\omega\pi\pi$, $3\pi$, $5\pi$, $\eta 3\pi$, $\eta'\pi$ |
| $\eta_1$ | 2100 | $1^{-+}$ | $a_1\pi$, $f_1\eta$, $\pi(1300)\pi$, $\eta\eta'$ | $4\pi$, $\eta 4\pi$, $\eta\eta\pi\pi$ |
| $\eta'_1$ | 2300 | $1^{-+}$ | $K_1(1400)K$, $K_1(1270)K$, $K^*K$ | $KK\pi\pi$, $KK\pi$, $KK\omega$ |
| $b_0$ | 2400 | $0^{+-}$ | $\pi(1300)\pi$, $h_1\pi$, $b_1\eta$, $f_1\rho$ | $4\pi$, $\omega\eta\pi$, $\eta 4\pi$ |
| $h_0$ | 2400 | $0^{+-}$ | $b_1\pi$, $h_1\eta$, $K(1460)K$ | $\omega\pi\pi$, $\eta 3\pi$, $KK\pi\pi$ |
| $h'_0$ | 2500 | $0^{+-}$ | $K(1460)K$, $K_1(1270)K$, $h_1\eta$ | $KK\pi\pi$, $\eta 3\pi$ |
| $b_2$ | 2500 | $2^{+-}$ | $a_2\pi$, $\omega\pi$, $\rho\eta$, $a_1\pi$, $h_1\pi$, $f_1\rho$, $b_1\eta$ | $\omega\pi$, $4\pi$, $\eta\pi\pi$, $\eta 4\pi$, $\omega\eta\pi$ |
| $h_2$ | 2500 | $2^{+-}$ | $b_1\pi$, $\rho\pi$, $\omega\eta$, $f_1\omega$ | $\omega\pi\pi$, $3\pi$, $\omega\eta 2\pi$ |
| $h'_2$ | 2600 | $2^{+-}$ | $K_1(1400)K$, $K_1(1270)K$, $K_2^*K$ | $KK\pi\pi$, $KK\pi$ |

in the isospin zero members of each nonet. For the exotic mesons listed in the table, the mixing is between the $\eta_1$ and $\eta'_1$, the $h_0$ and $h'_0$, and between the $b_0$ and the $b'_0$. These mixing angles can be measured experimentally by comparing the decay rates of each mesons to final states with and without kaons. The requirement to reconstruct exclusive final states involving several charged particles and photons requires a nearly hermetic detector with good momentum and energy resolution.

A thorough study of the hybrid spectrum, including the identification of the isovector triplet, with charges 0 and ±1, and both isoscalar members, $|s\bar{s}\rangle$ and $|u\bar{u}\rangle + |d\bar{d}\rangle$, for each predicted hybrid combination of $J^{PC}$, may only be achieved by conducting a systematic amplitude analysis of many different hadronic final states.

### 1.1.2 Photoproduction

Photoproduction provides certain advantages for the amplitude analysis of the final states in comparison with hadroproduction, say in $\pi^- p$ collision. In photoproduction the initial state interaction is suppressed. Also, photons can be linearly polarized. Photoproduction amplitudes involving unpolarized (or circularly polarized) photons can depend on the center of mass energy, $\sqrt{s}$, as well as the angle between the produced meson system and the initial photon direction (the polar angle, $\theta$). The use of linearly-polarized photons defines a second direction (along the polarization axis), and the corresponding production amplitudes can also depend on the angle to this axis—effectively the azimuthal angle, $\phi$. The extra information from this angle ultimately simplify the amplitude analysis. For the same statistical precision, a factor of two change in the degree of linear polarization mapping into a factor of two change in needed statistics. In addition to the simplification, for $t$-channel production of mechanisms, there is a one-to-one mapping between the naturality of the exchanged particle (natural parity exchange has $J^P = 0^+, 1^-, 2^+, \cdots$, while unnatural exchange has $J^P = 0^-, 1^+, 2^-, \cdots$) and the orientation of the linear-polarization direction in the event.

## 1.2 The Hall-D Complex and the GlueX Detector

The Hall-D complex consists of a tagger hall where incident $12\,GeV$ electrons produce a beam of linearly polarized photons, and the experimental hall, where the photons interact in an experimental target and the resulting interactions are recorded by the GlueX detector. A schematic of the complex, including the tagger area and the GlueX experiment, is shown in Figure 1.1. More information on the production, tagging and monitoring of the photon beam can be found in Chapter 2. The GlueX detector is described in detail in Chapter 3.

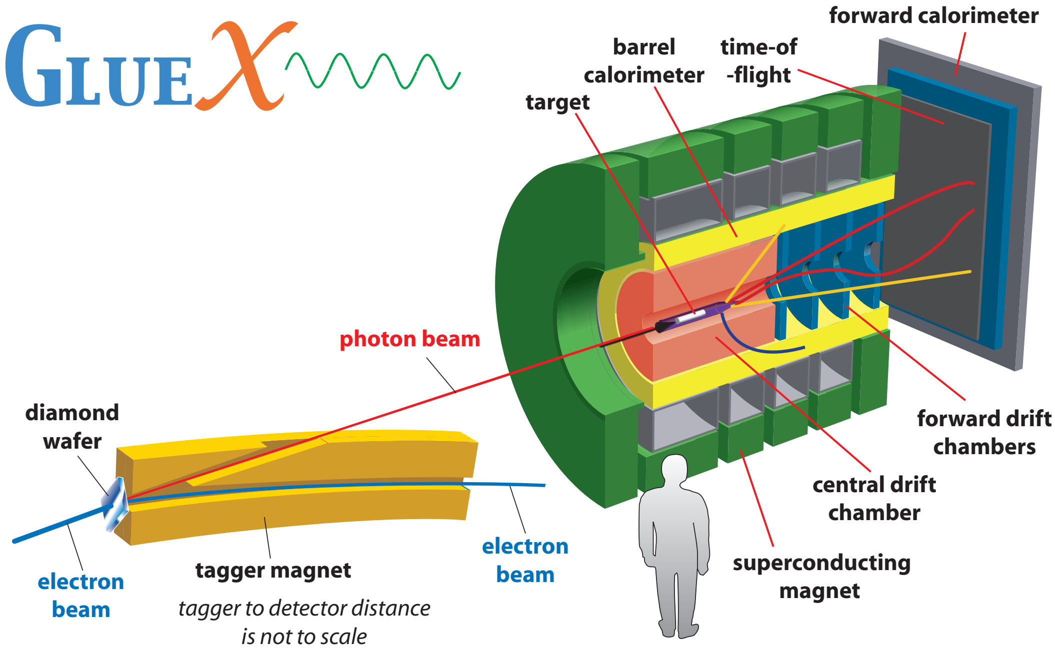

Figure 1.1: A cut-away drawing of the GlueX detector in Hall D.

### 1.2.1 Experimental Description

As seen in Figure 1.1, the $12\,GeV$ electron beam passes through a thin diamond wafer, where bremsstrahlung photons are produced. The electrons are then deflected by the tagger magnet. Non-radiating electrons are sent to a beam dump, while the electrons which have radiated more than a half of their energy are detected by a pair of hodoscope arrays. These arrays are aligned such that each detector element maps onto a narrow momentum range in the deflected electrons, and hence, a narrow energy range in the produced photons. Thus, the energy of each photon is “tagged” and known in the experiment. The photon beam then travels about $80\,m$ to the experimental hall, where prior to entering the experiment, it is collimated, and monitored using both a polarimeter and a pair spectrometer.

The photons can then interact in the target in GlueX. Much of the experimental apparatus is inside a solenoidal magnet with central filed of $2\,T$. The charged particles produced by the interacting photons are tracked by the start counter immediately outside the target (not shown in the figure), and then a pair of tracking systems. The central drift chamber is based on 28 layers of axial and stereo straws. The forward drift chambers are 24 drift chambers planes with both cathode and anode readout. The flight-time of charged particles are measured using a combination of the start counter and the time-of-flight wall in the forward direction, and the start counter and the barrel calorimeter inside the solenoid.

The final-state photons are detected in a pair of calorimeters. The barrel calorimeter, located inside the solenoid, consists if layers of scintillating fiber alternating with lead sheets. The forward calorimeter is downstream of the time-of-flight wall, and consists of 2800 lead-glass blocks.

### 1.2.2 Experimental Requirements

In order to be able to exclusively reconstruct events with final states given in Table 1.1, accurate reconstruction of the incident photon, as well as the produced charge particles and photons is necessary.

The linear polarization of the incident photon beam is produced through the coherent bremsstrahlung process. These coherent photons have energies in the range of 8.4 to $9\,GeV$, and will be about 40%, after the beam collimation to $\sim 25\ \mu$rad with respect to the incoming electron direction. For these linearly-polarized photons, it is necessary to accurately know the photon energy, both for the exclusive final state reconstruction and also to accurately determine the photon polarization on an event-by-event basis. In GlueX, this energy is known to an accuracy of 0.1% of the incident photon energy.

In order to exclusively reconstruct multi-particle final states, the GlueX detector needs be nearly hermetic with good momentum and energy resolution for both charged particles and photons. In order to be able to carry out the needed amplitude analysis, the detector acceptance needs to be reasonably uniform, and well understood and modeled in simulation. Typical momentum resolution for charged particles 1–2%, while for very-forward high-momentum particles, it is somewhat worse at around 8-9%. For high-momentum charged particles, the tracking system has nearly hermetic acceptance for polar angles from about 2° to 150° in the lab. Because of target material, protons with momentum below about $350\,MeV/c$ are not detected, and pions with momentum under $200\,MeV/c$ can have spiraling trajectories in the detector, which make reconstruction challenging.

For photons, the typical energy resolution is $(5\,\text{to}\,6\%)/\sqrt{E_\gamma}$. There is some variation in the barrel calorimeter resolution, depending on the incident angle of the photon, but generally, photons above about $50\,MeV$ are detected in the BCAL. The interaction point along the beam direction is determined by comparing the information from the readouts on the upstream and downstream ends of the detector. The forward calorimeter can reconstruct photons whose energy is larger than $100\,MeV$, with uniform resolution across the face of the detector. There is an overlap region between the calorimeters at around 11°. Both photon detection efficiency and energy resolution is degraded in this region.

### 1.2.3 Data Requirements

In addition to the ability to reconstruct exclusive final states, the GlueX experiment will need to collect sufficient statistics to carry out amplitude analyses in small bins of meson invariant mass, and in momentum transfer, $|t|$. Large production cross sections for reactions of interest are $10\,\mu b$, while more typical final-state cross sections are a few hundred $nb$. The GlueX experiment has been built with a data acquisition system capable of collecting data using photon beams with $10^8\,\gamma/s$ in the coherent peak. However, the experiment may be limited by electromagnetic backgrounds in the detector, and force to run at photon rates smaller than the design limit.

Expected raw event sizes are 15kilobytes, and the data acquisition limit is expected to be $20\,kHz$. The level-1 hardware trigger alone will allow the experiment to run at in incident photon rate of $10^7\,\gamma/s$ in the coherent peak. Of the $20\,kHz$ event rate, about $2\,kHz$ corresponds to hadronic interaction with photon in the coherent peak. In order to run at higher beam intensities, the level-3 software trigger is needed to keep the rate of events to tape limited to $20\,kHz$. Including the events where the energy of the interacting photon is above $9\,GeV$ roughly doubles the number of interesting hadronic events.

The typical final states listed in Table 1.1 are expected to range from 3.5% of the hadronic events for $\gamma p \to p3\pi$ to under 1%. Assuming an 85% reconstruction efficiency per final state particle, and that 60% of the final state protons are detectable, Table 1.2 shows the number of reconstructed events per hour assuming a total hadronic rate of $2\,kHz$ for events with photon energies in the coherent peak. These events are ultimately binned in both an meson invariant mass, as well as momentum transfer, $|t|$, but for most of these channels 40 days of running at 50% efficiency would produce about a factor of 500 times the number listed in the table.This is sufficient for an initial amplitude analysis on many of these channels. Phase IV running of GlueX anticipates 200 days of running with $5 \times 10^7$ photon beam intensity, a factor of 25 over the above estimate.

Table 1.2: PYTHIA predictions for the fraction of hadronic events in some final states interesting for exotic hybrid meson searches. The superscript on $(n\pi)^{0\pm}$ indicates the net electric charge of the $n$ pions. The specific final state column looks are one particular charge combination, and the event rate column show the number of reconstructed events per second assuming $10^7$ incident photons per second, and 85% reconstruction efficiency for each detected particle.

| Reaction | Fraction | Specific f.s. | Events/hour |
|---|---|---|---|
| $\gamma p \to p(3\pi)^0$ | 3.5 % | $p\pi^+\pi^-\pi^0$ | $87 \times 10^3$ |
| $\gamma p \to n(3\pi)^+$ | 2.0 % | $n\pi^+\pi^+\pi^-$ | $58 \times 10^3$ |
| $\gamma p \to p(2\pi)^0\omega$ | 1.8 % | $p2\pi^+2\pi^-\pi^0$ | $35 \times 10^3$ |
| $\gamma p \to n(2\pi)^+\omega$ | 1.0 % | $n2\pi^+\pi^-2\pi^0$ | $28 \times 10^3$ |
| $\gamma p \to p(3\pi)^0\eta$ | 2.0 % | $p\pi^+\pi^-\pi^0\eta$ | $14 \times 10^3$ |
| $\gamma p \to n(3\pi)^+\eta$ | 1.0 % | $n\pi^+\pi^+\pi^-\eta$ | $7 \times 10^3$ |
| $\gamma p \to p(2\pi)^0\eta$ | 1.0 % | $p\pi^+\pi^-\eta$ | $8 \times 10^3$ |
| $\gamma p \to n(2\pi)^+\eta$ | $< 1$ % | $n\pi^+\pi^0\eta$ | $< 13 \times 10^3$ |
| $\gamma p \to p\pi^0\omega$ | $< 1$ % | $p\pi^+\pi^-2\pi^0$ | $< 19 \times 10^3$ |
| $\gamma p \to n\pi^+\omega$ | $< 1$ % | $n2\pi^+\pi^-\pi^0$ | $< 33 \times 10^3$ |

## 1.3 Infrastructure [2]

The gross features of the infrastructure for the Hall D complex are given.

Table 1.3: General Hall D Tagger Building Infrastructure

| Feature | Value |
|---|---|
| Electron beam energy | $\lesssim$ 12 GeV |
| Width and length of Tagger Hall | 7.5 ×27.6 $m^2$ |
| Beam height above floor | 1.8 m |
| Low Conductivity Water (LCW) flow (130 psi supply, 70 psi drop, 90 deg F) | 40 gal/min |
| Chilled Water flow, includes collimator (80 psi supply, 30 psi drop, 45 deg F) | 10 gal/min |
| Floor Load capacity (designed for hydrostatic forces) | See facilities |
| Distance from radiator (the goniometer vacuum vessel center) to collimator (the front face) | 75.29 m |
| Distance tagger magnet center to electron dump | $\sim$ 24 m |
| Power deposition in electron dump | $<$ 60 kW |

Table 1.4: Collimator and Hall D Infrastructure

| Feature | Value |
|---|---|
| Photon beam energy | $\lesssim$ 12 GeV |
| Size of collimator alcove | 4.5×12.5 $m^2$ |
| Beam height above floor in collimator | 1.0 m |
| Beam power deposition in collimator alcove | $<$ 10 W |
| Size of Hall D | 15×29.5 $m^2$ |
| Crane (20 US tons) hook height above floor | 11 m |
| Electrical power installed Hall D Complex | 1 MVA |
| Floor Load capacity (designed for hydrostatic forces) | See facilities |
| Beam height above floor in Hall D | 3.5 m |
| Low Conductivity Water (LCW) flow (130 psi supply, 70 psi drop, 90 deg F) | 129 gal/min |
| Chilled Water flow, includes collimator (80 psi supply, 30 psi drop, 45 deg F) | 128 gal/min |
| Power deposition in photon dump | $<$ 2 W |

Table 1.5: Overall parameters for detector performance.

| Feature | Value |
|---|---|
| Solenoidal magnet | $\lesssim$ 2 T |
| Charged particle momentum resolution, $\sigma$ | $\sim$ 1-3% |
| Photon energy resolution, $\sigma_E/E$ | $\sim 5.5\%/\sqrt{E}$ |

---

[2] *SVN revision ID:* tdr_summary_infr.tex 13853 2014-06-12 03:42:44Z gen

# Chapter 2

# Hall D Photon Beam

## 2.1 Tagger Spectrometer

### 2.1.1 Tagger Magnet Summary

#### Tagger Magnet Summary [1]

The basic design or as-built parameters for the tagging magnet and the tagging spectrometer are given in Tables 2.1 and 2.2. The assembly drawing for the tagging magnet is D000001900-1000.

Table 2.1: Parameters for the tagging magnet.

| | |
|---|---|
| Radius of curvature | 26.7 m |
| Full-energy deflection | 13.4° |
| Field at 12 GeV | 1.5 T |
| Maximum Field | 1.75 T |
| Gap height | 3.0 cm |
| Flat pole tip width | 32.5 cm |
| Length of yoke | 6.146 m |
| Weight | 65 US tons |
| Length of focal plane (25% to 98% of $E_0$) | 9.10 m |
| Coil resistance | 0.564 Ω |
| Coil power at 12 GeV | 28 kW |
| Current at 12 GeV | 223 A |
| Vacuum | $10^{-5}$ Torr |
| Pole tip profile | Rogowski contour |
| Photon beam pipe diameter in yoke | 0.94 in. ID |

Table 2.2: Geometrical parameters of the tagging spectrometer for $E_0 = 12$ GeV : Bend = deflection angle; Drift = distance from exit edge to focal plane; Angle = angle between electron path and focal plane; cm/%$E_0$ = dispersion in units of cm per percent of the incident energy

| k (GeV) | Bend (deg) | Drift (m) | Angle (deg) | cm/%$E_0$ perp.to ray | cm/%$E_0$ along FP |
|---|---|---|---|---|---|
| 6 | 17.29 | 3.19 | 9.24 | 1.59 | 9.90 |
| 7 | 17.95 | 2.89 | 9.90 | 1.77 | 10.30 |
| 8 | 18.89 | 2.56 | 10.84 | 2.04 | 10.86 |
| 9 | 20.31 | 2.20 | 12.26 | 2.49 | 11.71 |
| 10 | 22.79 | 1.77 | 14.74 | 3.36 | 13.21 |
| 11 | 28.66 | 1.23 | 20.61 | 5.91 | 16.78 |

---

[1] *SVN revision ID:* tdr_summary_taggermagnet.tex 13854 2014-06-12 04:42:15Z gen

### 2.1.2 Tagger Microscope Summary

#### Tagger Microscope Summary [2]

The main parameters and properties of the Tagger Microscope (TAGM) are given in Tables 2.3 and 2.4. The assembly drawing for the tagger detectors installation is D000000002-1008.

Table 2.3: TAGM properties.

| Item | Value |
|---|---|
| Energy range, $E_\gamma$ | 8.1 - 9.1 GeV |
| Energy resolution (r.m.s.) | 5 MeV |
| Maximum counter rate | 3 MHz |
| Number of scintillators | array of 102×5 |
| Scintillator fibers | 2×2 mm$^2$ BCF-20 |
| Scintillator fiber length | 20±2 mm |
| Light guide fibers | 2×2 mm$^2$ BCF-98, ≈1 m long |
| Operating temperature | 20°C, forced air cooling |

Table 2.4: TAGM channel counts.

| Item | Description | Quantity |
|---|---|---|
| Light sensor | Hamamtsu S10931-050P MPPC (50 $\mu$m pixel size) | 510 |
| MPPC Bias supply | Wiener MPV8120l MPOD | 1 |
| Readout channels | 97 (column sums) + 5 individual columns | 122 |
| Flash ADCs | JLab fADC250-MHz, 16 ch | 8 |
| Discriminator | JLab leading edge, 16 ch | 8 |
| TDCs | JLab F1TDC V2, 32 ch, 60 ps | 4 |

---

[2] *SVN revision ID:* tdr_summary_microscope.tex 13854 2014-06-12 04:42:15Z gen

### 2.1.3 Tagger Hodoscope Summary

#### Tagger Hodoscope Summary [3]

The main parameters and properties of the Tagger Hodoscope (TAGH) are given in Tables 2.5 and 2.6. The assembly drawing for the tagger detectors installation is D000000002-1008. The assembly drawing for the TAGH counter is D000000103-1030.

Table 2.5: TAGH properties.

| Item | Value |
|---|---|
| Energy range, $E_\gamma$ | |
| continuous coverage | 9.1 - 11.78 GeV |
| $30-50\%$ sampling | 3.048 - 8.1 GeV |
| Total number of counters | 218 originally installed<br>(mounting slots for 274 counters) |
| Counter energy bin $\Delta E_\gamma$ (MeV) | |
| counter 1-22 (21 mm wide) | 10.2 - 23.7 |
| counter 23-40 (16 mm wide) | 18.4 - 29.5 |
| counter 41-64 (10 mm wide) | 18.7 - 26.8 |
| counter 65-81 (8 mm wide) | 21.7 - 26.0 |
| counter 82-131 (5 mm wide) | 16.4 - 22.2 |
| counter 132-151 (4 mm wide) | 16.6 - 17.2 |
| counter 152-218 (3 mm wide) | 13.7 - 20.3 |
| Scintillator thickness/height | $6\times40$ mm$^2$ |
| Scintillator material | EJ-228 |
| Maximum counter rate | 3 MHz |
| Light guide type | cylindrical shape, UVT PMMA |

Table 2.6: TAGH channel counts.

| Item | Description | Quantity |
|---|---|---|
| Light sensor | Hamamtsu R9800 PMT<br>JLab designed divider, divider based amplifier (gain $\sim 8$)<br>two signal outputs | 218 |
| HV for PMTs | CAEN A1535SN, 24 ch | 10 |
| Flash ADCs | JLab fADC250-MHz, 16 ch | 15 |
| Discriminator | JLab leading edge, 16 ch | 15 |
| TDCs | JLab F1TDC V2, 32 ch, 60 ps | 8 |

---

[3] *SVN revision ID:* tdr_summary_hodoscope.tex 13854 2014-06-12 04:42:15Z gen

## 2.2 Pair Spectrometer

### 2.2.1 Pair Spectrometer Magnet Summary

**Pair Spectrometer Magnet Summary** [4]

The main parameters and properties of the Pair Spectrometer Magnet are given in Table 2.7. The assembly drawing for the Pair Spectrometer Magnet is D000001500-1000.

Table 2.7: Pair Spectrometer magnet properties.

| Item | Value |
|---|---|
| Magnet type 18D36 | Water-cooled dipole |
| Maximum current | 1375 A |
| Nominal field for 12 GeV endpoint, at the center | 1.8 T |
| Current at 1.8 T | 990.0 A |
| Coil power at 990 A | 29.7 kW |
| Radius of curvature at B=1.8T, $E_{e^+/e^-}$=6 GeV | 11.14 m |
| Deflection at B=1.8T, $E_{e^+/e^-}$=2.8 GeV | 9.9° |
| Number of coil turns | 52 |
| Coil resistance (upper/lower/total) at 22.2$^{\rm O}$C | 15.20/15.11/30.31 mΩ |
| Original gap height/width/length | 6 inch / 18 inch / 36 inch |
| 2 iron pole tips added height/width/length | 3.89 cm / 45.47 cm / 91.4 cm |
| 2 iron pole tips material | AISI 1006 |
| Modified gap height/width/length | 7.62 cm / 45.7 cm / 91.4 cm |
| Iron yoke size height/width/length | 110.5 cm / 209.6 cm / 91.4 cm |
| Coils dimension along Z-axis | 118.9 cm |
| Original design weight | 17.5 US tons (Copper: 1.1 ton) |

---

[4] *SVN revision ID:* tdr_summary_psmagnet.tex 13854 2014-06-12 04:42:15Z gen

### 2.2.2 Pair Spectrometer Detector Summary

#### Pair Spectrometer Detector Summary [5]

The main parameters and properties of the Pair Spectrometer Detector are given in Tables 2.8 and 2.9. The assembly drawing for the high-granularity counters is D000001500-1007.

Table 2.8: Pair Spectrometer properties.

| Item | Value |
|---|---|
| High-granularity hodoscope (PS) | |
| $E_\gamma$ energy range | 6. - 12.5 GeV |
| $e^\pm$ energy range (two detector arms) | 3. - 6.25 GeV |
| $E_\gamma$ energy resolution | $\sim$ 30 MeV |
| Converter thickness | $5 \cdot 10^{-4}$ - $10^{-2}$ $X_0$ (TBD) |
| Rate per counter for ( $10^{-3}$ $X_0$ converter) | $>$ 1kHz |
| Number of scintillator tiles per detector arm | |
| tiles 1×10×30 mm$^3$ EJ-212 | 40 |
| tiles 2×10×30 mm$^3$ EJ-212 | 105 |
| Light collection | 1×1 mm$^2$ double-clad WLS fibers, BCF-92 |
| Low-granularity counters (PSC) | |
| Number of counters per detector arm | 8 |
| Scintillator size | 2×4.4×6 cm$^3$, EJ-200 |
| Light Collection | Fish-tail light-guide, UVT PMMA |

Table 2.9: Pair Spectrometer channel counts.

| Item | Description | Quantity |
|---|---|---|
| High-granularity counters (PS) | | |
| Light sensor | Hamamatsu S10931-050P MPPC (50 $\mu$m pixel size) | 2×145 |
| MPPC bias | ISEG EHS 201P-F-K, 16 ch, 10 mA for 5 MPPC/ch | 4 |
| MPPC LV | MPOD MPV8008, 8 ch | 1 |
| Operating temperature | room temperature, air cooling | |
| Flash ADCs | JLab fADC250-MHz, 16 ch | 19 |
| Low-granularity counters (PSC) | | |
| Light sensor | Hamamatsu H7415 PMT assembly with tapered divider | |
| Flash ADCs | JLab fADC250-MHz, 16 ch | 1 |
| Discriminator | JLab Leading edge discriminator, 16 ch | 1 |
| TDCs | JLab F1TDC V2, 32 ch, 60 ps | 1 |

---

[5] *SVN revision ID:* tdr_summary_ps.tex 13854 2014-06-12 04:42:15Z gen

# Chapter 3

# The GlueX Detector in Hall D

## 3.1 Superconducting Solenoid

### 3.1.1 Solenoid Summary [1]

The superconducting solenoid is used as the spectrometer magnet and also contains the $e^+e^-$ pairs produced by the photon beam in the target and other material inside. The magnet consists of 4 separate coils, each in its own helium bath and in its own vacuum vessel, and of an iron yoke. The cryogens are delivered from a distribution vessel above the magnet. The assembly drawing for the solenoid is D000000402-1000.

Table 3.1: The main parameters of the superconducting solenoid.

| | Value | |
|---|---|---|
| Inside diameter of coils | 80 in | 203.2 cm |
| Clear bore diameter | 73 in | 185.4 cm |
| Overall length along iron | 479.5 cm | |
| Number of turns | 4608 | |
| Operating temperature (actual) | 4.5°K | |
| Maximal allowed current at 4.5°K | 1350 A | |
| Nominal current at 4.5°K | 1300 A | |
| Maximal central field at 1350 A | 2.08 T | |
| Inductance at 1350 A | 26.4 H | |
| Energy at 1350 A | 24.1 MJ | |
| Total conductor length | 117600 ft | 35.84 km |
| Total conductor weight | 29000 lbs | 13.15 t |
| Substrate material | Copper | |
| Copper-to-filament ratio (grade A) | 20:1 | |
| Copper-to-filament ratio (grade B) | 28:1 | |
| Number of separate coils | 4 | |
| Longitudinal arrangement of coils | 2-1-3-4 | |
| Turns per coil 1 / conductor grade | 1428 | B |
| Turns per coil 2 / conductor grade | 928 | B |
| Turns per coil 3 / conductor grade | 776 | B |
| Turns per coil 4 / conductor grade | 1476 | A |
| Coil resistance at $\sim$ 300°K | 15.3 Ω | |
| Coil resistance at $\sim$ 10°K | $\sim$0.15Ω | |
| Coil cooling scheme | helium bath | |
| Total helium volume (including reservoir) | 3200 $\ell$ | |
| Protection circuit limiting voltage | 90 V | |
| Protection circuit resistor | 0.061 Ω | |
| Inside iron diameter | 116 in | 294.6 cm |
| Outside iron diameter | 148 in | 375.9 cm |
| Full weight | 284 t | |

---

[1] *SVN revision ID:* tdr_summary_sol.tex 13854 2014-06-12 04:42:15Z gen

## 3.2 Target

### 3.2.1 Target Summary [2]

The main parameters and properties of the target are given in Tables 3.2 and 3.3. The assembly drawing for the target is D000000300-0000.

Table 3.2: Liquid hydrogen target properties.

| Item | Value |
|---|---|
| Target, conical | Liquid Hydrogen |
| Target length | 30 cm |
| Upstream diameter | 2.42 cm |
| Downstream diameter | 1.56 cm |
| Target entrance window ⌀ (Kapton, 1.42 g/cm$^3$, 75 $\mu$m) | 1.56 cm |
| Target exit window ⌀ (Kapton, , 1.42 g/cm$^3$, 75 $\mu$m) | 1.56 cm |
| Super insulation | |
| Aluminized-Mylar+cerex (5 layers) | 2.9 mg/cm$^2$ per layer |
| Scattering chamber (Aluminum 25 $\mu$m) exit window diameter | 2.54 cm |
| Target cell, conical (not in beam path) | Aluminized Kapton, 127 $\mu$m |
| Super insulation (not in beam path) | |
| Aluminized-Mylar+cerex (5 layers) | 2.9 mg/cm$^2$ per layer |
| Scattering chamber (not in beam path) | |
| Aluminum-lined Rohacell ($\sim$ 110 mg/cm$^3$) | 9.44 cm OD, 7.49 cm ID |
| Distance from end of target to window | 4.5 cm |
| Nominal center in detector coordinates | 65 cm |
| Target pressure | 16 psia |
| Nominal operating temperature | $\sim$18°K |

Table 3.3: Additional target

| Item | Description |
|---|---|
| Cryogenic targets | $^4$He, D |
| Solid targets | various solid targets |

---

[2] *SVN revision ID:* tdr_summary_target.tex 13854 2014-06-12 04:42:15Z gen

## 3.3 Barrel Calorimeter

### 3.3.1 BCAL Summary [3]

The main parameters and properties of the BCAL are given in Tables 3.4 and 3.5, respectively. The assembly drawing for the BCAL is D000000107-1000.

Table 3.4: BCAL properties.

| Property | Value |
|---|---|
| Number of modules | 48 |
| Module length | 390 cm |
| Module inner/outer chords | 84.0 mm/118.3 mm |
| Lead-scintillator matrix thickness | 221.7 mm (14.9$X_0$) |
| Inner/outer Al plates thickness | 8 mm/31.75 mm |
| Module azimuthal bite | 7.5° |
| Total number of fibers | 683000 |
| Lead sheet thickness | 0.5 mm |
| Kuraray SCSF-78MJ multi-clad fiber | 1.0 mm |
| Pitch radial/lateral | 1.18 mm/1.35 mm |
| Volume ratios | 37:50:13 (Pb:SF:Glue) |
| Effective density | 4.86 g/cm$^3$ |
| Sampling fraction | 0.095 |
| Total weight | 28 t |
| MPPC operating bias, $V_{br} \approx 75$ V | 0.6-1.4 V above $V_{br}$ |
| Operating temperature | 5-25°C |
| Energy resolution, $\sigma_E/E$ | $5.4\%/\sqrt{E} \oplus 2.3\%$ |
| Time difference res., $\sigma_{\Delta T/2}$ | 70 ps/$\sqrt{E}$ |
| $z$-position resolution, $\sigma_z$ | 1.1 cm/$\sqrt{E}$ (weighted) |
| Polar/azimuthal angle resolution | $\sim 8/8.5$ mrad |

Table 3.5: BCAL channel counts.

| Item | Description | Quantity |
|---|---|---|
| Light guides | Trapezoidal, 10 types radially | $2 \times 4 \times 10 \times 48$ |
| Light sensor | Hamamatsu 144 mm$^2$ S12045 MPPC | $2 \times 4 \times 10 \times 48$ |
| Readout fADC | Sensors combined radially 1-2-3-4 | $2 \times 4 \times 4 \times 48$ |
| Readout TDC | Sensors combined radially 1-2-3 | $2 \times 4 \times 3 \times 48$ |
| Flash ADCs | JLab fADC250-MHz, 16 ch | 96 |
| Discriminator | JLab LE Discriminator, 16 ch | 72 |
| TDCs | JLab F1TDC V2, 32 ch | 36 |
| Monitoring | Blue LED Model SMS1105BWC, Bivar, Inc. | $2 \times 4 \times 10 \times 48$ |
| Monitoring controllers | Athens-custom. One per 4 strings of ten LEDs | 96 |
| MPPC Bias supply | ISEG EHS 201P-F-K, 16 ch, 8 mA for 10 MPPC/ch | 24 |
| LV power | MPOD MPV8008, 8 ch, 5 A/ ch | 8 |

---

[3] *SVN revision ID:* tdr_summary_bcal.tex 13854 2014-06-12 04:42:15Z gen

### 3.3.2 Introduction

The barrel electromagnetic calorimeter (BCAL) is a lead and scintillating fiber (Pb/SciFi) matrix built at the University of Regina, and is a key component of the GlueX detector. The BCAL is positioned immediately inside the solenoid, leaving a space of 2.7 cm radially between the two for supports and installation. This constrains the device's outer radius to be 90 cm, while its inner radius is fixed at 65 cm to allow adequate space for the CDC (see Section 3.6).

A principle goal of GlueX calorimetry is to detect and to measure photons from the decays of $\pi^0$'s and $\eta$'s which can come from the decays of produced mesons (normal or exotic) or possibly from excited baryons ($N^*$ or $\Delta$). The positions and energies of the photons must be determined to sufficient accuracy to allow for a complete kinematic reconstruction of the event. Adequate readout segmentation is required for an accurate determination of the azimuthal angle of tracks as well as for providing information on the energy deposition profile in depth, and for good cluster identification, while avoiding multiple occupancy. Detailed Monte Carlo studies [1,2] indicate that the BCAL is sensitive to photon energies in the range from 60 MeV to at least 2.5 GeV. Specifically, studies of the lowest energy photons in high-multiplicity reactions that are expected to yield exotic hybrids such as $\gamma p \to b_1(1235)\pi n \to 2\pi^+\pi^- 2\pi^0 n$ indicate that an energy threshold of 60 MeV suffices. The device also provides timing information for charged particles that will contribute to particle identification (PID) in the central region, in conjunction with the CDC. The BCAL will further assist in PID by providing $dE/dx$ information.

The relevant parameters that determine the $\pi^0$ and $\eta$ mass resolutions are the photon energy ($E$) along with polar and azimuthal position resolutions ($\sigma_\theta$ and $\sigma_\phi$). The energy resolution ($\sigma_E$) depends on the number of photoelectrons ($N_{pe}$) yielded by the photosensors, based on the collected light. The photoelectron statistics are strongly dependent on the stochastic fluctuations of the energy deposited by the electromagnetic shower in the scintillating fibers of the calorimeter. In addition, $N_{pe}$ depends on the fraction of photon shower energy deposited in the fibers, the efficiency with which the resulting scintillation light is captured and transmitted down the fiber to the photosensor, and the photon detection efficiency of the photosensor. The photon position is determined by the readout segmentation in the azimuthal direction, and in the beam-line direction ($z$) by the difference in arrival time ($\Delta T$) of the scintillation light between the two ends of the barrel. The time difference resolution ($\sigma_{\Delta T}$), and therefore the polar angle resolution, also depend on $N_{pe}$. These measurements assist in the reconstruction of the momentum of photons and in the PID for charged particles [3,4].

The performance metrics for these quantities were set by simulating hadronic photoproduction at GlueX energies using Pythia [5] and also by simulating several of the signature reactions expected to yield exotic mesons. These studies included a GEANT-based simulation [6] of the entire GlueX detector response, including detector material, cabling, photon reconstruction, and kinematic fitting. The Pythia simulations indicate that 70% of the produced photons with energies up to about 2 GeV will be incident on the BCAL. The photon population in the BCAL for one of the signature reactions, $\gamma p \to \eta\pi^0 p \to 4\gamma p$, where the distribution in $\eta\pi^0$ mass was generated uniform from 1.0 to 2.0 GeV/$c^2$ and uniform in decay angles, is shown in Fig. 3.1. The distribution of photons ($dN/dz$, where $N$ represents the number of photons) is plotted as a function of position from the upstream end of the BCAL, and predominantly populate the downstream end. Also graphed is the average energy as a function of $z$ with higher energy photons being more forward. The integrated thickness of the BCAL matrix, in number of radiation lengths, traversed by photons incident at various positions along the length of the BCAL is also

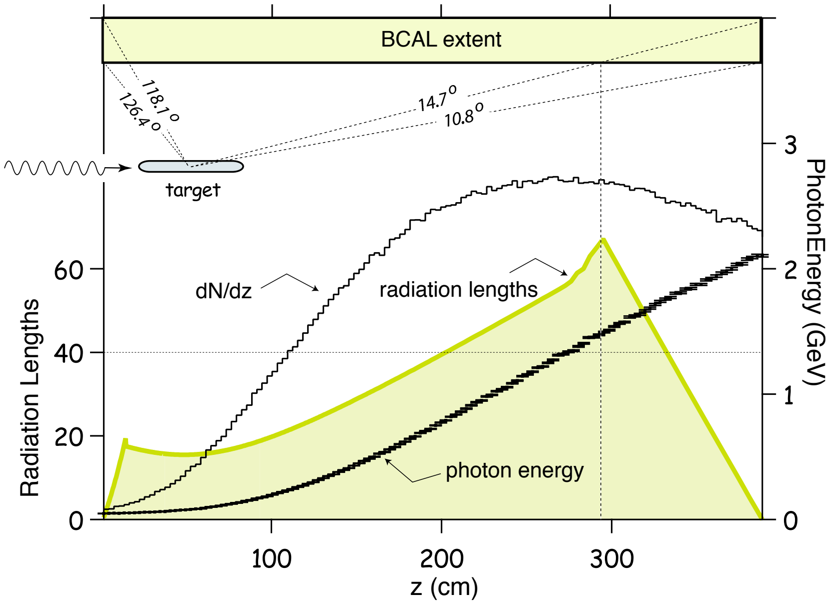

Figure 3.1: The distribution of photons (dN/dz), their energy and integrated path length through the Pb/SciFi matrix as a function of position along the length of the BCAL for one of the GlueX signature reactions, $\gamma p \to \eta\pi^0 p \to 4\gamma p$, is shown. The target position and angular range subtended by the BCAL are also presented.

displayed. The target occupies the region $z = 33 - 63$ cm relative to the upstream edge of the BCAL. Note that there is a narrow ($\sim 1°$) angular range near 11° where the photon trajectory intercepts a small number of radiation lengths of the Pb/SciFi matrix. Photons with angles less than 10°, with respect to the beam direction, will be detected in the FCAL.

### 3.3.3 Spaghetti Calorimetry

The BCAL design is based on scintillating fibers embedded in a lead matrix, which results in a relatively high–resolution sampling calorimeter. Such materials have been used in calorimeter design and operation for nearly three decades. The ratio of the active scintillator to the passive high-$Z$ material, as well as the diameter of the fibers, can be tuned to enhance resolution, to determine the radiation length, and to achieve uniformity in the ratio of electromagnetic (EM) to hadronic response (the $e/h$ ratio).

In general, the energy resolution of an electromagnetic calorimeter is expressed in the form:

$$\frac{\sigma_E}{E} = \frac{a}{\sqrt{E(\mathrm{GeV})}} \oplus b \oplus \frac{c}{E(\mathrm{GeV})}, \tag{3.1}$$

where the symbol $\oplus$ means that the quantities are added in quadrature.

The $a/\sqrt{E}$ term contains the combined effect of sampling fluctuations and photoelectron statistics, with the former dominating the resolution. This is commonly referred to as the stochastic term. The constant term, $b$ in Eq. 3.1, originates from sources that scale with energy and contribute to uncertainties in the energy reconstruction. These sources can be mechanical imperfections, material defects, segment-to-segment calibration variations, non-uniformity of response, instability with time, and shower leakage. The noise term, $c/E$, results from noise, and pileup in high-rate environments. A similar equation governs the timing resolution:

$$\sigma_t = \frac{c}{\sqrt{E(\text{GeV})}} \oplus d. \tag{3.2}$$

In general, the constant term $d$ is the result of residual calorimeter mis-calibrations. However, the measured time difference will also be smeared by the finite beam spot size in a test beam when used to determine this quantity.

### 3.3.4 BCAL Geometry and Parameters

The BCAL is modelled closely after the EmCal calorimeter built for the KLOE experiment at DAΦNE [7,8,9], which, for more than a decade, also operated in a solenoidal magnetic field. The KLOE collaboration developed tooling for the production of long-grooved lead sheets, pushed the technology for excellent fibers with long attenuation lengths (2.3 m $< \lambda <$ 3.2 m), and built a device with inner radius of 2 m and length 4.3 m [10]. This device utilized 1 mm diameter scintillating fibers, with ratios of fiber to lead to glue of 48 : 42 : 10. The energy and timing resolutions for KLOE [9] are

$$\frac{\sigma_E}{E} = \frac{5.4\%}{\sqrt{E(\text{GeV})}} \oplus 0.7\%, \quad \sigma_t = \frac{56 \text{ ps}}{\sqrt{E(\text{GeV})}} \oplus 133 \text{ ps}.$$

The latter yields a nearly constant $\sigma_t \approx 180$ ps for photon energies above 150 MeV, and a diverging timing resolution for $E_\gamma < 75$ MeV. The EmCal parameters and performance served as benchmarks for the BCAL.

A key instrumentation difference is that the EmCal employed conventional PMT readout at each end, that was possible due to the lower field and more favorable magnetic field gradient of KLOE compared to GlueX. The BCAL requires devices that are practically immune to magnetic fields; Silicon Photo–Multipliers (SiPM's) operate reliably under such conditions. Additionally, it is important to point out differences in the GlueX and KLOE applications of barrel calorimetry. KLOE is a symmetric colliding beam experiment with the intersection region at the center of its barrel calorimeter. As a result, that calorimeter is illuminated symmetrically and nearly uniformly by photons having average energies of 100-200 MeV, with very few photons greater than 400 MeV. On the other hand, GlueX is a fixed target experiment resulting in a highly asymmetric photon distribution (30% of the photons in the BCAL will have energies considerably higher than 500 MeV). Despite these differences, the KLOE experience provided valuable guidance in the design and construction of the BCAL. The KLOE resolutions are adequate for the GlueX physics requirements, as indicated by our simulation studies. The extracted resolutions are a direct result of the internal Pb/SciFi matrix geometry such that similar resolutions should be expected for the BCAL [11].

For GlueX, the tracking elements inside the magnet's bore require a radius of at least 65 cm in order to perform as desired, leaving about 25 cm of radial thickness for the BCAL. Additionally, the BCAL must reside within the 4.5 m length of the solenoid. These constraints lead to a long, narrow, tube-like design. In this geometry, the readout is logically placed at the ends where space exists, and where it can take advantage of the fact that all fibers run parallel to the symmetry axis of the solenoid. With rise times of a few ns, good timing can be expected in collecting the light from a shower. Moreover, because the EM showers spread across the azimuthal boundaries, algorithms for finer positioning of the shower are required. A typical weighted position resolution is $\delta x \approx 5$ mm $/\sqrt{E}$. For the BCAL design, this would lead to an azimuthal resolution of ∼8.5 mrad. Using the $z$ position resolution of approximately 4 cm, obtained from the time difference, leads to a polar angular resolution at 45° of ∼8 mrad. The time difference from the two ends produces the $z$ coordinate of the hit. Because we will use an array of readout devices on each end (segmented in azimuth and depth), redundant measurements are made of the $z$ coordinate. These measurements of $z$ correspond to different average radii and therefore help to establish the angle of the incoming photon. Finally, the fractional volume of scintillator in the detector makes BCAL efficient for detecting charged hadrons. The mean light collection time of the two readout ends can be used to determine the particle time-of-flight (TOF). TOF coupled with the track length and momentum then yields particle mass, thus contributing to PID information.

The BCAL design is depicted in Fig. 3.2. A zoomed-in view of the matrix is portrayed in Fig. 3.3. The main parameters of the BCAL can be found in Ref. [12] and fabrication was based on the assembly drawings in Ref. [13]. The completed lead-scintillating fiber matrix including the light collection and sensing units at each end is called a module. Fourty eight modules, plus one spare, were constructed.

The choice of readout device must bear in mind the considerable magnetic field (2 T) inside the bore, and the rapidly varying fringe field at the ends. The option chosen for the readout is based on a large-area application of SiPM's. These devices offer gain and timing resolution comparable to that of a PMT, superior energy resolution, are immune to magnetic fields, and require simple electronic amplification and summing circuits. Each channel also includes low-voltage bias and power for the preamplifiers, a flash ADC, discriminator, TDC and cabling. Forty independent light guides were fastened with epoxy to the two polished ends of the BCAL. A gain-stability monitoring system is critical and is based, in part, on small LED's glued directly to each of the light guides. The LED driver system consists of small LED boards, driven in four strings of 10 LEDs per side, using a custom-designed controller board. All these are presented in more detail below.

### 3.3.5 Module Construction

In order to build lead-SciFi modules, our collaboration studied and used the KLOE tooling techniques. Specifically, a "swager" (plastic deformation machine) was borrowed from KLOE and was used as a model to build our own. As a result, several prototypes were built, gradually increasing in dimensions and culminating in two full-sized prototypes, named Prototype 1 and 2. Each prototype had a length of 400 cm, a width of 13 cm, and height ranging from 21 to 24 cm. For the production, lead sheets were ordered from the manufacturer[4] at specified widths and Kuraray SCSF-78MJ, double-clad fibers[5] were used.

The modules were built by employing two custom-designed presses that pressed the matrix as it was being stacked with alternating layers of lead sheets and fibers, thereby expelling excess epoxy and allowing the bonded matrix to set. They consisted of a ∼4.5 m steel table, two tilting pistons that raised/lowered a group of 20 pistons to the top surface of the matrix, as well as associated electronics and pneumatics. The fibers were bonded in the lead channels

---

[4] Vulcan Lead Inc (www.vulcunlead.com)

[5] Kuraray America Inc., Houston, TX, USA (www.kuraray-am.com)

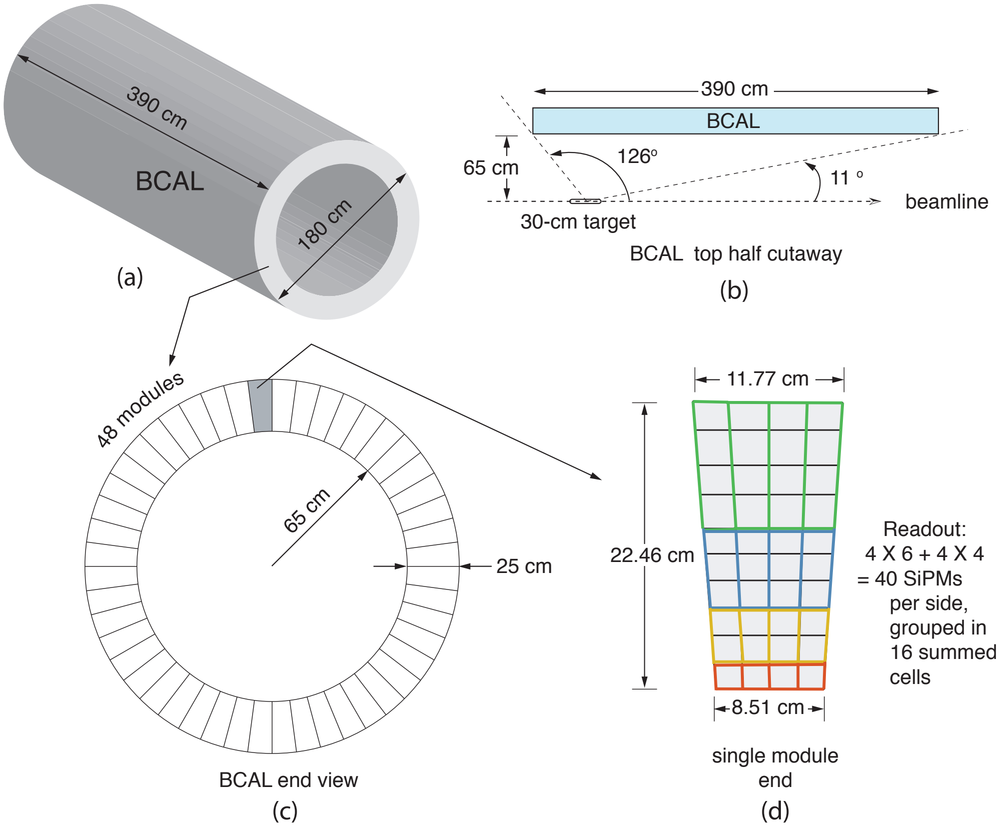

Figure 3.2: Sketch of Barrel Calorimeter readout. (a) A three-dimensional rendering of the BCAL; (b) top-half cutaway (partial side view) of a BCAL module showing polar angle coverage and location with respect to the GlueX liquid $H_2$ target; (c) end view of the BCAL depicting all 48 azimuthal modules, and (d) an end view of a single module showing the readout segmentation: four rings (inner to outer) comprised of sums of 1, 2, 3, and 4 readout rows, respectively, and four azimuthal slices (columns), resulting in a total of 16 summed readout zones. More details can be found in the text.

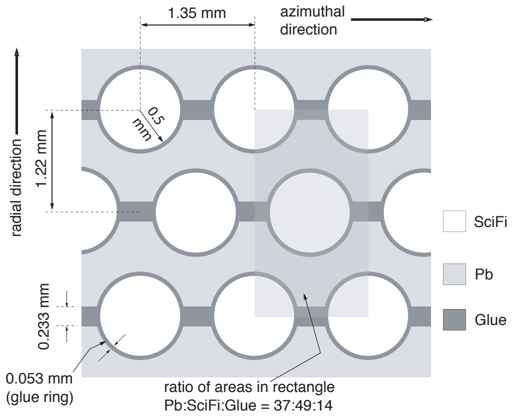

Figure 3.3: Close-up view of the BCAL matrix details.

with Bicron-600[6] optical epoxy: the internal matrix geometry is indicated in Fig. 3.3. Visual inspection revealed that only a handful of the approximately 15,350 fibers in each module were damaged during the construction.

A comprehensive report (how-to manual), training video, photos, and movies were prepare to simplify the training of personnel and to document the methods employed [14, 15, 16, 17]. The final set of construction procedures were recorded in a step-by-step "Procedures Manual" – complete with photos – which details the entire production process [18].

Built modules were shipped for machining to an industrial firm[7]. The process included shaping the modules to their final dimensions within tight tolerances, polishing the two ends, and machining features in the aluminum base and top plates.

### 3.3.6 Light guides

The BCAL light guides connect the output face of the modules to the SiPM light sensors. The geometry of the light guides is azimuthally symmetric, consisting of four identical radial columns per BCAL wedge. Each column consists of ten light guides, which cover an azimuthal angle of 1.875° degrees. Both the input and output faces of the light guides are trapezoidal in shape. The bases of the guide are glued to the face of the BCAL module and increase in width toward the outer edge of the wedge. The radial dimension of the bases is $20.57\,mm$ for the inner six guides and $24.64\,mm$ for the outer four. The base of the guide receives the light from the calorimeter and funnels it down to a smaller trapezoid covering the sensitive area of the SiPM sensors, which have an area of $1.27 \times 1.27\,cm^2$. The length of the light guides is $8\,cm$. There is a $0.5\,mm$ air gap between the output of the light guide and the $0.45\,mm$ clear epoxy protective coating over the sensitive area of the SiPM. The light guide shapes are shown in Fig. 3.4. The simulated light collection for the ten guides ranged from 48-75%. [19]

The light guides were fabricated from ultraviolet transmitting (UVT) acrylic at the Universidad Técnica Federico Santa María according to JLab drawings [20,21,22,23,24,25,26,27,28,29]. Dimensional tolerances were kept under control to avoid interferences between wedges. The light guides were glued onto the face of the modules at Jefferson Lab using Norland NOA 87 UV adhesive following the procedure documented in Procedure D000000107P003 [30]. Each light guide was covered with black Tedlar to avoid any optical cross talk between the firing cells. Measurements of different materials for the cover showed no significant differences in light collection [31], as might be expected if the collection efficiency is dominated by total internal reflection. Tested LED boards in strings of 10 LEDs were glued onto the face of the light guides during the gluing procedure while there was access. Hardware to attach the readout assembly was mounted to each module and every combination of LED string and high voltage setting was verified to output signals. An overnight run triggering on cosmic rays was taken as a reference for future calibrations. The gluing procedure and repairs were documented using the JLab Pansophy system [32] .

### 3.3.7 Silicon Photomultiplier Arrays

The BCAL resides inside a 2 T superconducting solenoid with the magnetic field – in its readout region — calculated to be 1.5-2 T upstream and ∼0.5 T downstream. We have selected the new

---

[6] Saint-Gobain Crystals & Detectors, USA (www.bicron.com)

[7] Ross Machine Shop, Ltd. 40 Kress Street, Regina, SK, Canada

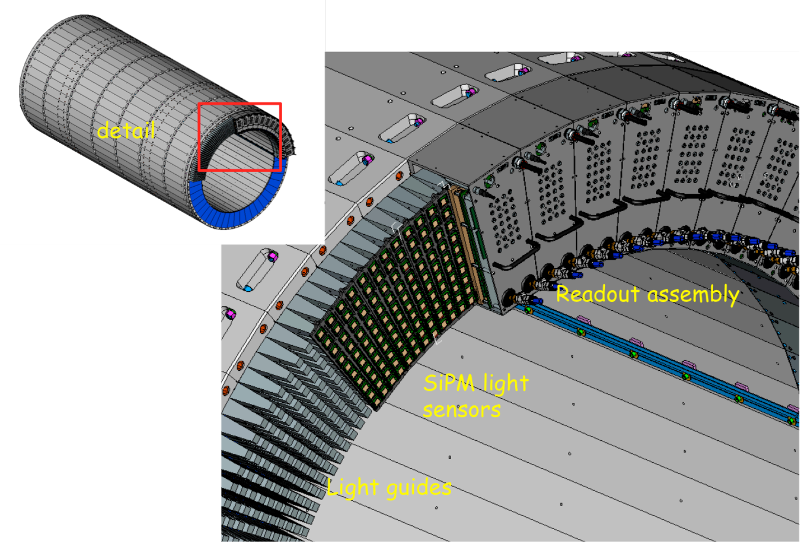

Figure 3.4: Three-dimensional rendition of the light guides mounted at the end of the BCAL, as well as the readout assemblies mounted over them. The readout assemblies contain the SiPMs and their electronics.

technology of silicon photomultiplier arrays (SiPMs), which can operate in fields well beyond that present in GlueX. The arrays were developed through an extensive R&D effort between GlueX and SensL[8], a photonics firm from Ireland. This led to the “tiling” of 16 $3 \times 3$ mm$^2$ SiPM’s into a $4 \times 4$ array of cells, having a 1.26 cm$^2$ area. Such large area units have found broad appeal, from subatomic physics to medical applications, with several manufacturers entering the field. Following a competitive bidding process, Hamamatsu[9] was selected to provide the readout devices for the BCAL.

The selected sensors are Hamamatsu S12045 Multi-Pixel Photon Counter (MPPC) arrays with a sensitive area of 1.44 cm$^2$. The basic SiPM unit is a $3 \times 3$ mm$^2$ cell with 3600 50 $\mu$m micro-pixels, which are joined together on a common substrate and under a common load. The sensor is a $4 \times 4$ array of cells with a dynamic range defined by the 57,600 micro-pixels in each array. The single micro-pixel gain is $\sim 10^6$, roughly the same order of magnitude as that of a traditional PMT. While each pixel operates digitally as a binary device, the output signal behaves as an analog detector that is proportional to the incident light intensity.

The SiPM’s operate at an operational voltage $V_{op}$ that is 0.9–1.2V above the typical breakdown voltage ($V_{br}$) of about 71 V at room temperature. The gain is proportional to this over voltage ($V_{over} = V_{op} - V_{br}$). At $V_{over}$=0.9 V and 23°C, these devices have a typical gain of

---

[8] SensL, Blackrock, Cork, Ireland (www.sensl.com)

[9] Hamamatsu Corporation, Bridgewater, NJ 08807, USA (sales.hamamatsu.com/en/home.php)

$0.75\times10^6$, and photon detection efficiency (PDE) of about 21% [33], but a relatively high single-photoelectron dark rate of 16 MHz per array. The relatively low over-voltage and the sensitivity of the breakdown voltage to temperature imposes considerable requirements on operation. The sensitivity of the breakdown voltage to temperature is nominally 56 mV/°C [34]. The gain, PDE and dark rates all depend on the breakdown voltage and therefore proper operation of the sensors requires careful temperature stabilization.

A total of 3840 SiPMs are needed to instrument the BCAL. The order for the SiPMs was placed based on Specification D000000107S004 [35] and was split between Jefferson Lab (1200 units) and the Universidad Técnica Federico Santa María (USM) (2810 units). The eighty first article samples were checked at Jefferson Lab and in all cases they either achieved or exceeded the design specifications [36, 37]. Quality control tests were carried out at Jefferson Lab and USM on each SiPM unit received. Only one unit failed specifications at JLab, and three units failed at USM. All four defective samples were replaced by Hamamatsu. Regina also conducted selected tests mimicking the experimental conditions, with an exception that the data was analyzed using energy-summing boards (photo peaks not visible) instead of individual readout boards (reading each of the 16 cells of the array individually, thus seeing the photo peaks). The average geometrical mean from the Regina measurements of $(24 \pm 2)\%$ is consistent with measurements at Jefferson Lab $(21 \pm 1)\%$ [36]) and USM $(23 \pm 2)\%$ [38]. All measurements produced PDE values $> 19\%$, which was the contract specification and were also consistent with test data provided by Hamamatsu. The characteristics of the arrays measured are shown in Fig. 3.5.

### 3.3.8 Radiation Damage

It is well known that the performance of silicon detectors degrades after exposure to radiation. Therefore, we have checked the effect of radiation to the Hamamatsu S12045 MPPC arrays. Only the dark rate seems to be significantly affected, which increases linearly with neutron dose at a rate of about 16 MHz per $10^9 n_{eq}/\text{cm}^2$ [33,39]. The dark current is essentially unaffected by electromagnetic radiation, tested with 0.67 MeV $\gamma$ rays from a $^{137}$Cs source up to an exposure of 2 krad (which is ten times the dose expected in ten years of operation in HALL D). The calculated neutron fluence at the downstream end of the BCAL during high intensity operation, assuming $10^7$ live seconds per year and a hydrogen target, is $3 \times 10^8 \text{n}_{\text{eq}}/\text{cm}^2$. The fluence at the upstream end is about four times less. Running with a helium target would increase the fluence by 50% [40]. Over the course of time, the dark rate at room temperature will exceed our design specification of 100 MHz/array. This increase will be compensated for by operating the MPPC's at lower temperature. The dark rate is three times less at 5°C than at 20°C [41]. Running at a temperature of 5°C would extend the expected useful lifetime of the MPPC's at high intensity to about 7 years. However, initially the sensors will be operated just below room temperature at about 18°C so we can use water in the cooling loops which will allow for the risk of condensation inside the readout assemblies to be avoided.

### 3.3.9 Readout Assembly and Granularity

The readout assembly holds all forty MPPC's that collect light from one end of a module, the supporting infrastructure to operate them, and the electronics that produce output signals to feed the flash ADCs and pipeline TDCs. The temperature stabilization is an integral component of the assembly and is addressed using a two-fold approach. First, we have implemented a

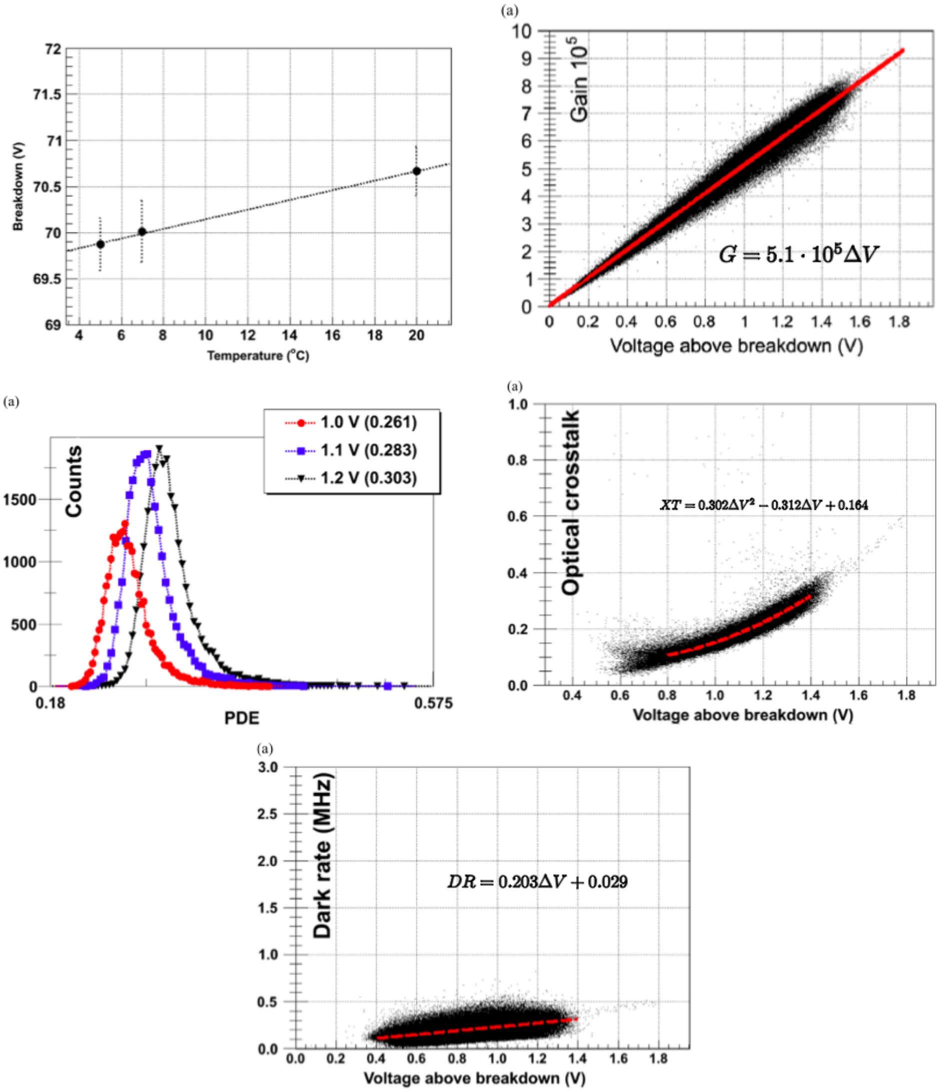

Figure 3.5: Measured characteristics of the production SiPM arrays (Hamamatsu S12045 MPPC's). *Top left panel:* Breakdown voltage versus Temperature. *Top right panel:* Gain versus voltage above breakdown. *Middle left panel:* Counts versus photon detection efficiency at three different applied voltages. *Middle right panel:* Optical cross talk versus voltage above breakdown. *Bottom panel:* Dark rate versus voltage above breakdown.

mechanical cooling system with the goal of maintaining the temperature of the sensors within ±2°C of the operating point. The cooling system is composed of a chiller; the coolant is water during initial operation, and later for operation at 5°C, the coolant is a mixture of water and 20% propylene glycol. The coolant flows through a copper pipe that is glued to a copper cooling plate, which is in thermal contact with the back of the SiPM sensors. Second, a thermistor is incorporated in the sensor bias circuit to compensate for any temperature deviations from the nominal operating point, thereby maintaining a stable output under small changes in the environment. The relatively low over voltage results in high sensitivity to the setting and

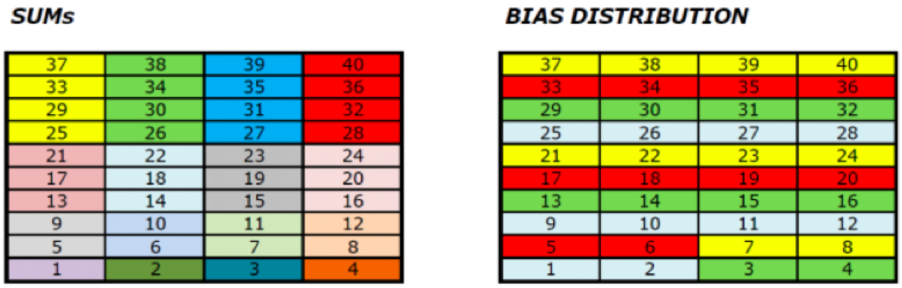

**SUMs**

| | | | |
|---|---|---|---|
| 37 | 38 | 39 | 40 |
| 33 | 34 | 35 | 36 |
| 29 | 30 | 31 | 32 |
| 25 | 26 | 27 | 28 |
| 21 | 22 | 23 | 24 |
| 17 | 18 | 19 | 20 |
| 13 | 14 | 15 | 16 |
| 9 | 10 | 11 | 12 |
| 5 | 6 | 7 | 8 |
| 1 | 2 | 3 | 4 |

**BIAS DISTRIBUTION**

| | | | |
|---|---|---|---|
| 37 | 38 | 39 | 40 |
| 33 | 34 | 35 | 36 |
| 29 | 30 | 31 | 32 |
| 25 | 26 | 27 | 28 |
| 21 | 22 | 23 | 24 |
| 17 | 18 | 19 | 20 |
| 13 | 14 | 15 | 16 |
| 9 | 10 | 11 | 12 |
| 5 | 6 | 7 | 8 |
| 1 | 2 | 3 | 4 |

Figure 3.6: *Left panel:* Schematic layout of summed (1:2:3:4) MPPC outputs for the upstream facing downstream. Each number corresponds to a single sensor and colors show the groups that are summed into the readout channels. *Right panel:* Assignment of four bias voltages to groups of ten MPPC's: light blue is bias 1, green is bias 2, red is bias 3 and yellow is bias 4. The summing is radially outward as shown in Fig. 3.2 and the bias channels are assigned along rings of constant radii. The upstream and downstream ends are mirror symmetric so that a cell number at the upstream end corresponds to the same number downstream.

stabilization of the bias voltage. The requirement is to maintain the voltage set point to within 10 mV, which corresponds to a gain variation of less than 1%. The effect of any temperature changes must also be kept to less than 1%.

The layout of the individual MPPC bias and readout is shown in Fig. 3.6. The light guides are arranged in four rows of ten identical columns on the face of the BCAL modules. Each MPPC has its own pre-amplifier but various groups of MPPC's are summed to generate the output signals. The BCAL is divided into four readout rows, within which individual MPPCs are summed column-wise in groups of 1, 2, 3 and 4, respectively. This scheme retains the complete azimuthal segmentation, but results in coarser longitudinal shower segmentation, a decision based on electronics cost considerations [42]. Thus, forty MPPC's on each end of the BCAL are summed into sixteen groups, which are digitized by 250 MHz Flash ADC's, but only the first twelve sums are discriminated and fed into pipeline TDC's to measure their times. The bias lines deliver power to groups of ten sensors, but the grouping is orthogonal to the readout sums, as shown in the figure. This allows individual MPPC's to produce the sole output of a summed channel by appropriately enabling bias voltages during calibrations.

The temperature compensation circuit for BCAL is a voltage divider with one temperature dependent resistor element (thermistor). The values of the resistances coupled with the value for the $V_{Supply}$ voltage allow the sharing of a single supply voltage among several SiPMs, while still providing a temperature compensated $V_{op}$ value that stabilizes gain. The individual resistor values to tailor the input voltage to different MPPC's were determined based on Hamamatsu datasheet values for the recommended $V_{op}$ (given for 25°C) and adjusted for a presumed operation temperature of 5°C. Operation at a specified temperature and over voltage ($V_{over}$) requires a formula that takes into account the temperature dependent nature of the voltage divider circuit, and the errors from ideal operation induced by granularity of the trim values. Details are provided in Ref. [43]. The formula has been incorporated into the EPICS control system to set the proper operating parameters for each of the four bias inputs to each side of each module. For this reason, the readout assemblies are not easily interchangeable.

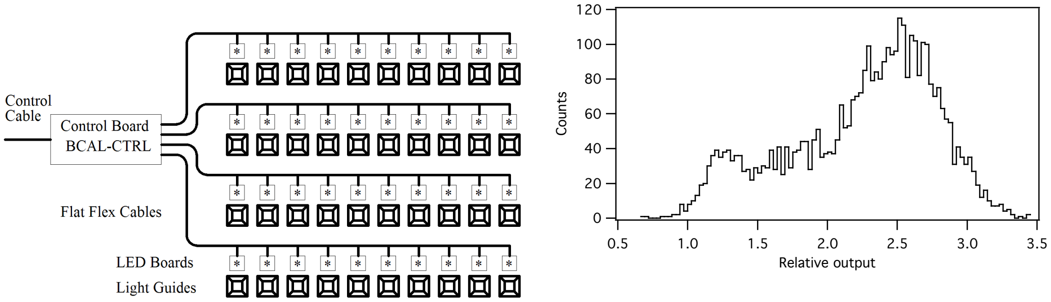

Figure 3.7: *Left panel:* Configuration of the BCAL monitoring system for one side of one module. *Right panel:* Relative output of all BCAL LEDs driven by their respective boards.

### 3.3.10 BCAL monitoring

The monitoring system is designed to track the stability of the MPPC output signals between calibrations with particles. The system is composed of light emitting diode (LED) light sources, which are distributed one per light guide. They are placed in pockets drilled on the side of the light guide, which are 4 mm in diameter and 2 mm deep and located 3.8 cm from the BCAL module. The monitoring system is presented in more detail in Ref. [44]. Here we give a brief overview.

The LEDs[10] come in a standard surface mount package emitting blue light at 471 nm, which is near the peak of the fiber emission spectrum [45]. Each LED is attached to a 12 × 13.5 mm$^2$ PCB board so that it emits light parallel to the PCB, through the near light guide and toward the opposite side of the BCAL module. Light enters the fibers and is transmitted through the module to the sensor at the far end, and is also reflected from the near end of the module back into the near sensor. With this geometry, the signal in the near sensor includes prompt light as well as a delayed reflected pulse from the opposite end of the module. The signal in the far sensor is smoother and reaches a higher peak amplitude.

As mentioned previously, the forty LEDs at each module's end are grouped into four independent groups. The system configuration is shown in the left panel of Fig. 3.7. Each group is attached to a flex ribbon cable and its 10 LEDs are pulsed simultaneously using a common trigger signal from a control board (BCAL Controller) located on the outer edge of each wedge. Each string is attached to a column of light guides, which is orthogonal to the cabling that provide the bias to the MPPCs. The possibility of noise pickup in a MPPC induced by the BCAL monitoring system was investigated but no such pickup was detected as a result of proximity operation to both LED and controller boards.

3840 production LED mini boards plus 100 spares were tested and divided into groups of similar intensity. The relative light outputs of these LEDs are shown in the right panel of Fig. 3.7. The variation between the LEDs in a single group of ten is typically less than 1%. However, this grouping will not be used in the experiment, as in order to reduce cost and complexity only eight bias lines will power all LEDs, based on which of the BCAL upstream or downstream quadrant they belong, as explained in the paragraph below. At least two LED bias settings will be used for the gain monitoring, one nominal and one at a higher bias for those LEDs that have weak signals at the nominal bias.

---

[10] Model SMS1105BWC, Bivar, Inc., CA 92618, USA (www.bivar.com)

The overall pulsing system is segmented into four quadrants for both the upstream and downstream LEDs. In each quadrant, four independent TTL signals feed the BCAL Controllers of the twelve modules, which can fire the LEDs in a single column simultaneously. The bias and low voltage to the LEDs can also be adjusted for each quadrant independently. EPICS GUIs have been developed that allow pulsing the system at pre-described rates for the purpose of firing the LEDs and triggering the DAQ system. Whenever an LED trigger is enabled, the system also generates a NIM signal, which is used to enable triggers by the DAQ system.

### 3.3.11 Characteristics of the components

#### Production Fibers

Due to the length of the BCAL, superior quality fibers were required and ordered according to Specification D000000107S001 [46]. Over three quarters of a million, 4-m-long Kuraray double-clad SCSF-78MJ (blue-green) scintillating fibers have been used in the construction of the BCAL. The response and quality of a random sample (∼0.5-1%) of fibers was tested from each shipment, and the quality assurance results confirmed that the fibers were of high quality and complied with GlueX specifications. The key parameters measured were:

1. dimensional uniformity: outer radius conforming to 1 mm diameter.
2. spectral response: wavelength of maximum emission of the scintillator was specified to be between 450 and 500 nm.
3. bulk (effective) attenuation length: specified to be greater than 300 cm with an $RMS \leq 10\%$ over the 100-280 cm source distance range, when measured with a bi-alkali photomultiplier tube.
4. light output: specified in terms of the number of photoelectrons ($N_{pe}$) collected at the fiber's end, which had to be greater than 4.5 using a bialkali PMT at 200 cm from the source with $RMS \leq 15\%$.

The measurements and conclusions from this extensive Quality Assurance (QA) excercise are summarized herein; detailed interim [47,48,49] and final reports were produced [50] and detailed summary published in Refs. [51] and [52].

In order to assure a uniform matrix during the building, the fibers had to be uniform in diameter and free of defects (such as protrusions). To this end, fibers were visually inspected and the fiber diameter was measured at three locations along the length of each sampled fiber (50 cm, 200 cm and 350 cm from one end) using a micrometer caliper, for 883 fibers from Shipments 1-29. The error on each measurement was 0.005 mm. A Gaussian fit to all the data yielded $(0.997 \pm 0.006)$ mm. All measurements fell within the specifications: diameter of 1 mm with a $RMS \leq 2\%$.

#### Spectral Response

Details on the test setup can be found in Refs. [53, 50, 51], and, therefore, are recounted only briefly herein. A USB4000 spectrophotometer[11] and the tested SciFi were coupled together in

---

[11] Ocean Optics Inc., Dunedin, FL, USA (www.oceanoptics.com)

a robust manner. An RLS-UV380 ultra violet LED[12] – having a peak emission wavelength of 373 nm – stimulated the fiber. The LED translated across the length of the fiber and measurements were carried out in near darkness. As an additional precaution against UV damage, UV-absorbing film (TA-81-XSR[13]) was used to cover all overhead fluorescent lights and desk lamps.

Measured wavelength spectra were fitted using double Moyal functions plus a flat background, with the LED positioned at 10 cm, 30 cm, 100 cm and 300 cm. The Moyal function is of the form:

$$f(x, a, \mu, \sigma) = a \cdot \exp\left(-\frac{1}{2}\left(\frac{(x-\mu)}{\sigma} + e^{-(x-\mu)/\sigma}\right)\right) \tag{3.3}$$

These spectra are overlayed in Figure 3.8 together with the corresponding spectra from Kuraray of a fiber from Lot JS072 [54]. The peak intensity and the integrated spectral strength scale as a function of distance from the light source in a similar manner for both sets of measurements. Minor differences in the spectral shapes between our measurements and those from Kuraray are perhaps due to the measurement apparatus and/or specific choice of fibers tested.

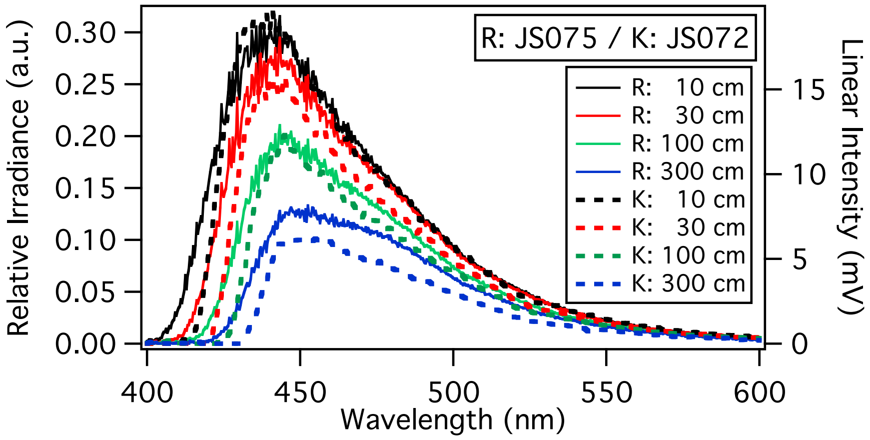

Figure 3.8: Wavelength spectra, measured at Regina ('R' label) at source distances of 10 cm, 30 cm, 100 cm and 300 cm for a JS075-lot fiber are shown as solid lines, with the corresponding Kuraray spectra [54] ('K' label) for a JS072-lot fiber displayed as dotted curves. The former are relative irradiance measurements and the latter are in units of linear intensity.

### Attenuation length

Considering the large number of fibers to be tested, an expedient method was developed in order to extract the attenuation length based on a Hamamatsu calibrated S2281 photodiode [50, 51]. It should be mentioned that the spectral sensitivity of this device is relatively flat in the range of the fiber emission spectrum, and as such, the extracted attenuation length reflects the fiber

---

[12] Roithner Lasertechnik, Vienna, Austria (www.roithner-laser.com)

[13] Window Film Systems, London, ON, Canada (www.windowfilmsystems.com)

performance exclusively. Each tested fiber was positioned horizontally in a 420-cm-long, 1-mm-deep channel machined in a black polyethylene board that had an attached length scale. The near end of the fiber was polished using a Fibre Fin 4 diamond polisher[14] before being connected to the photodiode using Dow Corning[15] optical grease, and the device was read out using a Keithley 6485 picoammeter[16]. The far fiber end was initially blackened using black mat enamel paint (used for scale model painting), and later left as un-blackened factory rough-cut. An RLS-UV380 UV LED stimulated the fiber. The LED could be positioned on the lab bench guided by a holder on the polyethylene board and translated across the length of the fiber.

The data from each fiber were fit using a single exponential fit of the form $I = I_0 e^{-x/\lambda}$ in the 100-280 cm source distance range. The results conform to contract specifications, with $\lambda$ greater than 300 cm in all cases. The average of all measurements was $\lambda = (387 \pm 26)\ cm$. The agreement is quite good in the comparison between Regina and Kuraray measurements, and similar features are present in both data sets. Since the measuring setups are different, the features are clearly a result of the fiber properties, which depend primarily on the secondary dye content. Finally, both Kuraray's and Regina cumulative results had a standard deviation less than 10%, and therefore met the contractual specifications.

A single exponential fit to the fiber data is possible only over a limited range of source distance, as was carried out above. When the entire range is examined, and in particular source distances below 100 cm, a double exponential fit is required owing to the capture of short-wavelength light (blue region) which otherwise becomes absorbed leaving only the longer wavelengths. The following function was used:

$$I = I_0 \left( e^{-x/\lambda_L} + \alpha \cdot e^{-x/\lambda_S} \right) \tag{3.4}$$

where $\lambda_L$ and $\lambda_S$ are the long and short attenuation lengths, respectively, $I_0$ is the readout current in units of $\mu$A and $\alpha$ represents the relative strength between the two components. Most events were clustered in a peak centered around $\alpha = 0.3$, and average values of $\lambda_L = (482 \pm 5)$ cm and $\lambda_S = (74 \pm 1)$ cm were extracted.

The shipment results are shown in Figure 3.9. The error bars reflect the standard deviation of the distribution from individual fiber measurements. Linear fits show the extracted averages. It is noted that a correction to the attenuation length due to the different treatment of fibers for Shipments 1-3 was not applied (a 3% increase), but this does not change any of the conclusions that all measured parameters were found to be comfortably within contract specifications, and overall this product was of high quality.

### Number of photoelectrons

Details on the $N_{pe}$ measurements can be found elsewhere [50, 52], and are only summarized herein. Both ends of the fiber were polished and one was blackened. The fiber was then inserted in a dedicated measuring station contained in a 4.5-m-long dark box. A Hamamatsu R329-02 calibrated photomultiplier with a standard progressive voltage divider was used to measure the light from the fiber. A small dab of optical grease[17] was applied to the non-blackened polished end of the fiber before coupling it to the PMT using a piece of machined acrylic as a fiber guide.

---

[14] FibreFin Inc., 201 Beaver Street, Yorkville, IL, USA (www.fiberfin.com)

[15] Dow Corning Corporation, Midland, 48686 MI, USA (www.dowcorning.com)

[16] Keithley Instruments, Inc., Cleveland, 44139 OH, USA (www.keitlhey.com)

[17] EJ-550 Silicone Optical Grease, ELJEN Technology, (`www.eljentechnology.com/`)

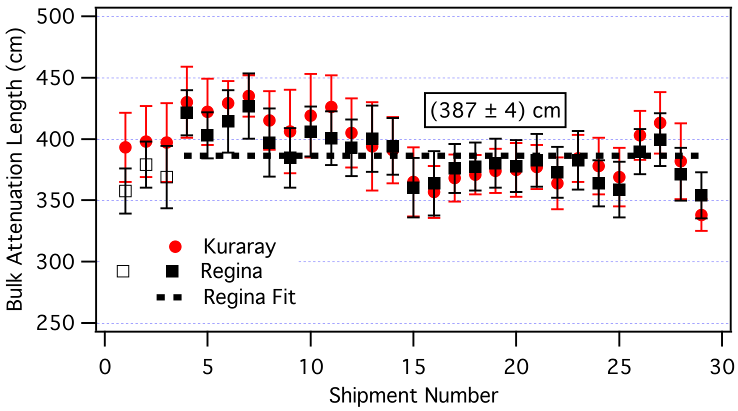

Figure 3.9: The bulk attenuation length, from a single exponential fit between 100-280 cm is shown as a function of shipment number for Regina and Kuraray measurements.

The fiber was stimulated using a $^{90}$Sr radioactive source, which was placed within a custom-designed lead collimator, the latter positioned over the center point of the fiber at approximately 200 cm from the PMT's end. The collimator consisted of a $4 \times 4$ cm$^2$ Pb block, having an 8 mm diameter partial bore to house the source. Located below the source was a slit having dimensions $13\,(h) \times 0.5\,(w) \times 8\,(l)$ mm$^3$ with a $1 \times 1$ mm$^2$ groove, parallel to the 8-mm-slit side, along the bottom of the collimator for accurate placement and illumination of the tested fiber. The collimator included a lid, since it was determined that a small amount of "backsplash" activity resulted from source electrons striking the lid of the dark box. A scintillator counter of length $\sim$9 cm was coupled to a Burle 8575 PMT (at 1700 V) and was placed directly below the fiber, thus sandwiching the fiber between it and the source/collimator above.

The results of the fit extractions for the $N_{pe}$ — averaged for each lot and plotted against the lot number with the error bar being the RMS of those distributions — are shown in Figure 3.10. Only fibers from Lots 96–707 (Shipments 4–29) were analyzed; Lots 1–95 (Shipments 1–3) were excluded from this comparison due to different handling of the fiber ends. Clearly, there is lot-to-lot variation apparent in the number of photoelectrons, as was also manifest in the attenuation length measurements [51]. Kuraray observed a similar behaviour in measurements of their own, with the most likely candidate for the difference being small impurities in the secondary dye in the fiber's chemistry, which cannot be controlled in the manufacturing process[18].

Kuraray used different dye batches for the fiber production, supplied by one of their vendors. Two correlated groupings (clusters) are discernible in the two-dimensional representation of attenuation length versus $N_{pe}$, one belonging to dye batch 'B' (open circles) and the combined dye batches 'C' to 'F' (open squares) in Figure 3.11. The latter are grouped rather tightly and as such are presented as a single group rather than plotted separately. Note that dye batch 'A' corresponds to the fibers that had one end polished (shipments 1-3 or lots 1-95) and were not included in the analysis as explained above.

---

[18] Kuraray, private communication (2011)

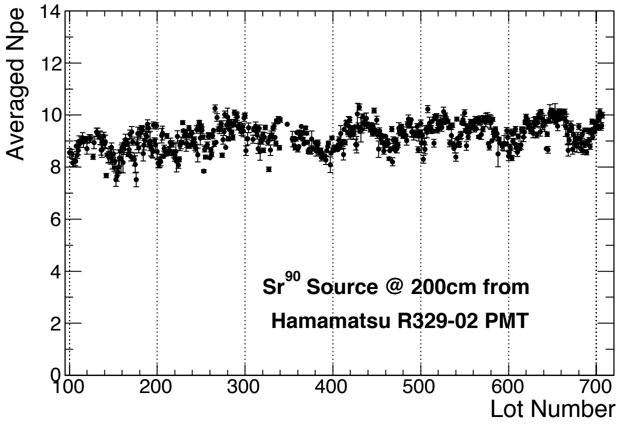

Figure 3.10: The $N_{pe}$ results are averaged by lot number, and their average is graphed against the lot number. The results conform to contract specifications by being greater than 4.5 using a bialkali PMT at 200 cm from the source with $RMS \leq 15\%$.

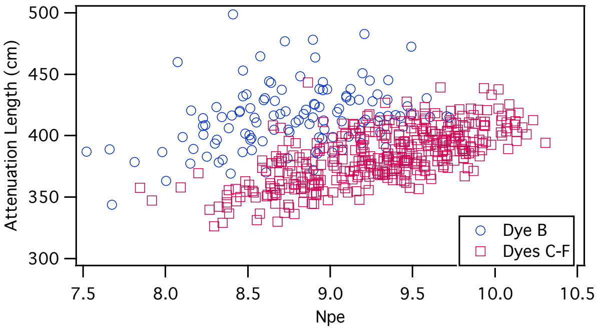

Figure 3.11: The attenuation length to $N_{pe}$ correlation is shown for dye batch 'B' (open circles) and for the combined dye batches 'C' to 'F' (open squares). Details are in the text.

### 3.3.12 Photon Beam Test: Energy and Timing Resolution and $N_{pe}$

A photon beam test of Prototype-1 module was carried out in Hall B of Jefferson Lab in 2006 with the objective of measuring the energy and timing resolutions of the module, as well as the generated number of photoelectrons [55, 56]. This prototype served to establish of baseline for the performance of the final BCAL, but not all its components nor shape were retained for production. The prototype had a rectangular cross section instead of the trapezoidal shape of the final detector modules. It was constructed using Pol.Hi.Tech.0044 fibers[19], while the fibers selected for production were higher-quality Kuraray SCSF-78MJ fibers. The prototype was divided into 18 segments, each with dimensions $3.81 \times 3.81$ cm$^2$ and readout by PMTs, while the production readout has 16 segments consisting of MPPC sums. Low current (1 nA) data were collected over the tagged photon energy range of 150 to 650 MeV at multiple positions

---

[19] Pol.Hi.Tech. S.R.L., Carsoli, Italy.

and angles along the module. The photon beam was collimated with a 2.6 mm collimator, resulting in a beam spot of virtually uniform density with a diameter of 1.9 cm on the BCAL module. The extracted energy resolution at normal incidence and at the center of the module was $\sigma_E/E = 5.4\%/\sqrt{E(\mathrm{GeV})} \oplus 2.3\%$, i.e. the fits were consistent with $c = 0$ of Eq. 3.1. Small variations in the fits produced relatively large variations in the floor term $(2.3 \pm 1\%)$ but little variation in the stochastic term $(5.4 \pm 0.1\%)$. The energy resolution plotted versus the mean tagger energy for the respective bin is shown in Figure 3.12 and demonstrate the design meets our requirements.

We also studied how the resolution changed for showers produced by photons incident at forward angles. The extracted energy resolution shows the degradation as the incident photon angle decreases. Specifically, the stochastic term $a$ in Eq. 3.1 increases from 5.4% at 90° ($z = 0$ cm[20], center of module) to over 7% at 15° ($z = 100$ cm). The change in the parameter $a$, shown in Figure 3.12, is expected since fluctuations from intrinsic properties of the interaction mechanisms increase with the number of particles created as the shower develops. As the angle decreases, the particles transverse more of the radiator mass resulting in more interactions and increased fluctuations [11]. This expectation has been corroborated with Monte Carlo simulations [57].

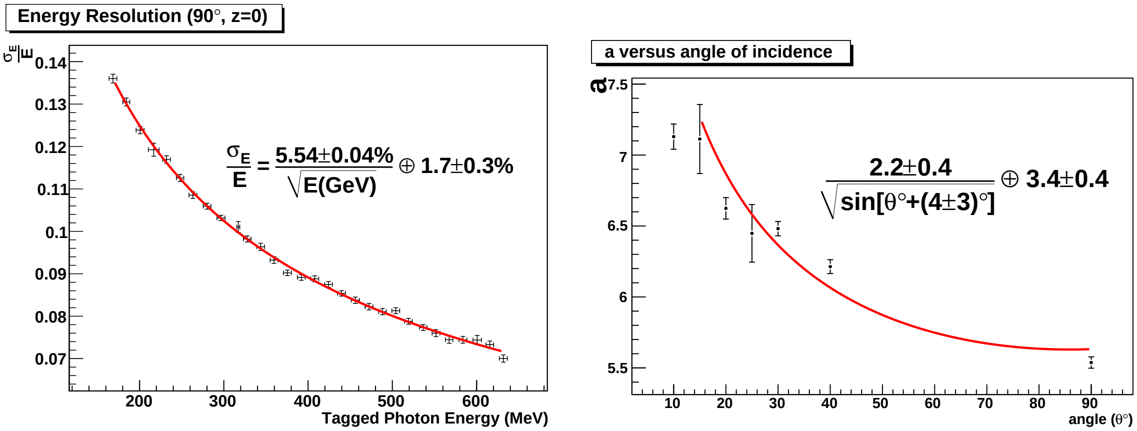

Figure 3.12: Results of the photon beam test. Left: Energy resolution at normal incidence ($\theta$=90°) as a function of tagged photon energy. Right: Resolution parameter $a$ (Eq. 3.1) versus angle of incidence. As the angle decreases the energy term degrades, which is expected because the energy leakage from the sides and from backsplash out of the front face of the module, increases.

The time difference between opposite ends of the BCAL will provide position information for neutral particles, which is needed to reconstruct their four-momentum. The position resolution is related to the time difference resolution by the effective speed of light within the calorimeter. Thus, by using measurements of the effective speed of light in the calorimeter ($v_{\mathrm{eff}} = 17 \pm 0.4$ cm/ns from a previous beam test at TRIUMF [58]), the position resolution of the calorimeter can be easily extracted. The double-ended readout of the BCAL allowed for time difference measurements to be made. The timing for an event was found by summing the TDC values of all the segments in an event cluster, weighted by their energy. The floor term from the fits

---

[20] The coordinate system for the beam test, in contrast to the GlueX global coordinate system, has the coordinate $z$ along the length of the module with the origin at the center of the module.

was equal to the finite width of the beam, as expected. This implies that the intrinsic time resolution of the BCAL is consistent with zero for the constant term, and this why we quote the timing without a floor term. The time difference resolution, after subtracting the beam width from the constant term, was found to be

$$\sigma_{\Delta T/2} = \frac{70\text{ ps}}{\sqrt{E(\text{GeV})}}. \tag{3.5}$$

The position resolution can be computed as $\sigma_z = \sigma_{\Delta T/2} \cdot v_{\text{eff}}$, which gives $\sigma_z = 1.1$ cm for a 1 GeV photon.

The number of photoelectrons per end of the prototype BCAL module, $N_{pe}$, was estimated at $z = 0$ cm and $\theta = 90°$. The distribution in the ratio, $R$, of the North to the South readout sums, for each of ten bins in beam energy, $E_j$, from 150 MeV to 650 MeV, was expressed as

$$R(E_j) = \frac{\sum_{i=1}^{18} E_{\text{N},i;j}}{\sum_{i=1}^{18} E_{\text{S},i;j}}. \tag{3.6}$$

Using this ratio results in the suppression of shower fluctuations that dominate the statistical variance of the individual sums for each readout end. Under the assumption that each of the amplitude spectra has a Poisson-type shape, the ratio spectra were fitted to the function:

$$f(r) \sim \int P(x, N_{pe} \cdot \sqrt{R}) \cdot \frac{1}{r} P\left(\frac{x}{r}, \frac{N_{pe}}{\sqrt{R}}\right) \left[\frac{x}{r} dx\right], \tag{3.7}$$

where $r$ is the event-by-event North/South amplitude ratio, $R$ is an average North/South amplitude ratio, $N_{pe}$ is the average number of photoelectrons, and $P$ is a Poisson probability. The resulting photoelectron yield per end was plotted as a function of beam energy and fit to a linear function, holding the y-intercept fixed at zero. This resulted in $N_{pe} = 662 \pm 1$ photoelectrons per end at 1 GeV. In comparison, KLOE reported $N_{pe} \sim 700$ per end at 1 GeV.

### 3.3.13 Simulation

#### Shower Profile and Energy Resolution

Details of the full BCAL detector response to photons has been simulated using a stand-alone Monte Carlo program that incorporated fine details of the geometry that are not included in the standard Hall D Monte Carlo HDGeant [59]. This allows the description of the shower development in fine steps as well as computation of the sampling fraction, which are not treated accurately in HDGeant. We conducted a series of simulations using GEANT3 [57], without the inclusion of the BCAL magnetic field. However, a description of the geometry of the fibers inside the matrix was included as it is important to determine the correct sampling fraction. Individual fiber and epoxy volumes were programmed into the Monte Carlo with the appropriate Pb:SciFi:Glue ratios and material properties resulting in the geometry shown in Fig. 3.3. The micro geometry of the fiber matrix was encoded in two different ways. In the first, the glue boxes were approximated by trapezoids between the fibers and in the second, strips of glue were placed “inside” the lead with the fiber volumes on “top”. The first is termed *traps* and the second *strips*. These yielded consistent results and only the latter were considered further.

We first fit the shower development to the standard parameterization [60]. If the depth of the shower in the material, expressed in radiation length units, is $t = x/X_0$ and the energy of the incident particle is $E_0$ then

$$\frac{dE}{dt} = E_0\, b\, \frac{(bt)^{a-1}\, e^{-bt}}{\Gamma(a)} \tag{3.8}$$

describes the evolution of the electromagnetic cascade in the material and, therefore, the shape of the longitudinal shower profile in the lead-fiber-glue matrix. The parameters $a$ and $b$ depend on the nature of the incident particle and the type of the absorbing material. The depth in the material, where the shower maximum occurs, depends on the incident particle's energy $E_0$ and the critical energy $E_c$. This parametrized longitudinal development of the electromagnetic shower describes the shower reasonably well when the incident photon energy is larger than 1 GeV [61].

Simulations were run from normal incidence down to the minimum acceptance angle of the BCAL. The longitudinal shower profile is shown in the left panel of Figure 3.13 for three different angles of the incident photon with respect to the beam direction. Note that the abrupt termination of a curve corresponds to the end of the matrix due to the exhausted number of radiation lengths. The discrete simulations have been fitted with Equation 3.8. The simulated profiles exhibit the characteristic shower profile shape and expected evolution with increasing energy. At 14° the low energy particles deposit almost all of their energy in the first segment of the module. This explains why the fitted function does not describe the shower development as well as it does for 45° or 90°.

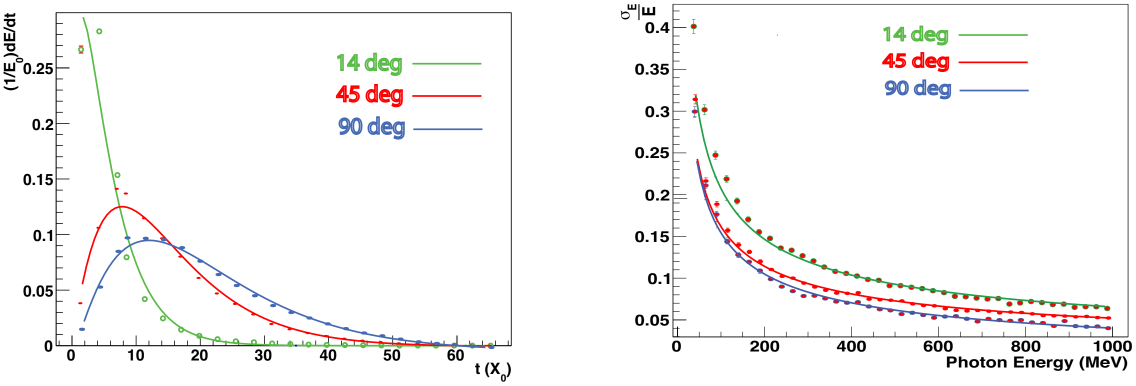

Figure 3.13: *Left panel:* Longitudinal shower profile for 200 $MeV$ simulated photons impinging at 14°, 45° and 90°. The data points correspond to the Monte Carlo results and are fitted with Equation 3.8 represented by the lines. *Right panel:* Energy resolution as a function of incident photon energy for photons impinging at 14°, 45° and 90°. The points are simulated data whereas the lines represent fits to Equation 3.1. The extracted fit coefficients for the energy and floor term ($a$, $b$) were ($6.56 \pm 0.02$, $0 \pm 0.2$)%, ($4.98 \pm 0.02$, $0 \pm 0.2$)%, and ($5.01 \pm 0.03$, $0.5 \pm 0.6$)%, for the three angles respectively.

The simulated energy resolution is graphed in the right panel of Figure 3.13 and is in agreement with past simulations [62]. The energy resolution reaches its best value at angles 45° and larger as a result of the improved ability of the module to contain the electromagnetic shower at those angles. At 14° the situation is quite different. The resolution is worse, which is a manifestation of the increased shower leakage from the front of the module (albedo). The shower path at 14° is long enough to eliminate leakage from the back of the module.

### Sampling Fraction and Leakage

The sampling fraction – the fraction of energy deposited in a SciFi – can be expressed as a ratio with respect to either the total energy deposited in the BCAL module ($f$) or the incident photon energy ($f_\gamma$), with $f_\gamma < f$ since $E_{mod} < E_\gamma$ owing to energy leakage outside the calorimeter volume. These quantities are difficult to measure in an experiment but fairly simple to simulate. Simulations indicate that $f_\gamma$ decreases as a function of photon energy due to leakage, with the loss being approximately constant above 200 MeV. Clearly, $f$ depends only on the energy deposited in the matrix itself and is independent of the incident photon energy or overall geometry of the module. Our most recent sampling fraction simulations are in general agreement with earlier ones, although the magnitude is less: 9.5% [57] instead of 11.5% in [63, 61]. This is expected due to the refining the SciFi volume to include the insensitive[21] two layers of cladding. The sampling fluctuations, $\sigma_f/f$, are the dominant contributor to the energy resolution, and are about $4.5\%/\sqrt{E(\mathrm{GeV})}$. Subtracting the simulated sampling fluctuation contributions from the measured energy resolution yields photoelectron statistics contribution to the energy resolution of about $3.1\%/\sqrt{E(\mathrm{GeV})}$ [63]. This is similar to the estimated value of $\sim 2.7\%/\sqrt{E(\mathrm{GeV})}$ from a KLOE beam test [64].

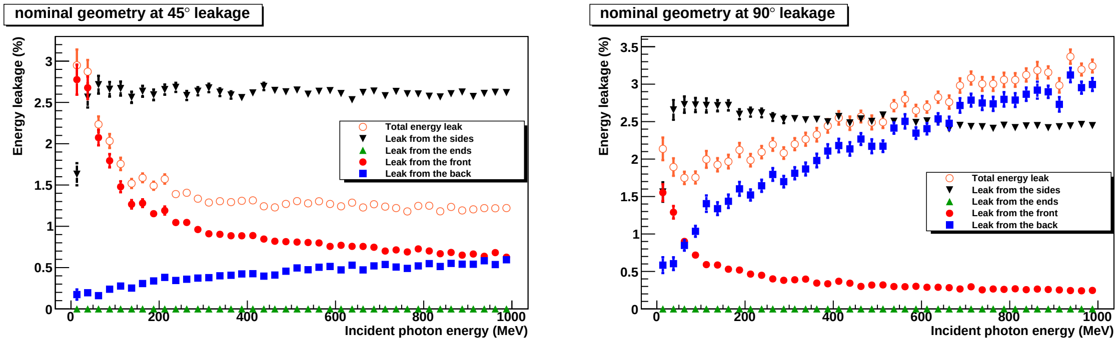

Figure 3.14: Simulated energy leakage (in percent) versus incident photon energy. Energy leakage from the sides (black filled triangles) is plotted but not added to the total energy leakage (red open circles). The leakage out the ends (green filled triangles) is consistent with zero in all cases except at 12°.

The percent energy leakage out the calorimeter volume is shown in Figure 3.14. The different symbols correspond to energy leaking out from different faces of the module. Front and back refers to the inner and outer faces of the module, with respect to the radial direction. Leakage from the ends refers to the energy leaking out from the faces of the module along the direction of the beam, where photo sensors will be placed. Leakage from the sides refers to the faces of the module that will be in contact with it's nearest neighbor modules. As the latter will be recovered in adjacent modules during the experiment, it was not included in the leakage sum. Indeed, total energy leakage refers to the sum of all energy leaking out the module from front, back and ends. For incident photon angles of 90°, irrecoverable energy

---

[21] Insensitive in this context has the meaning of not contributing to the energy deposited in the fibers.

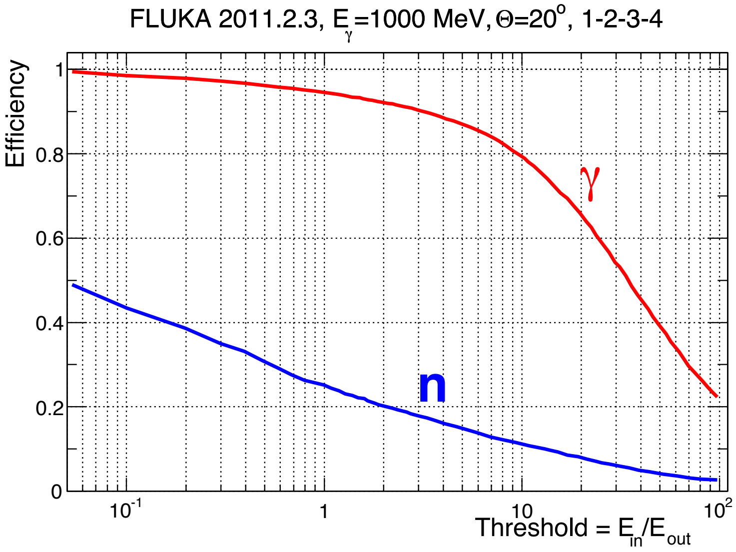

Figure 3.15: The efficiency of photon and neutron detection is plotted versus threshold.

leakage occurs mostly from the back of the module and it increases monotonically, following the evolution of $t_{max}$. There is little energy leaking out the front face of the module (albedo) at 90°, but it increases with decreasing angle and dominates the leakage at small angles (12°-14°). The fraction also tends to be larger at lower energies. Low energy particles have increased probability of interaction with only a few layers of lead before the secondary particles drop below the energy threshold for generation of secondaries. Furthermore, there is increased probability of low energy particles to back scatter and end up leaving the module out the front.

### Photon-Neutron Separation

Dedicated simulations were carried out contrasting the energy deposition and patterns of photons to neutrons [65]. The aim was to separate photon-caused and neutron-caused showers of the same energy deposited in BCAL fibers. The kinetic energy of selected neutrons (of about 1200 MeV) was significantly larger than the energy of correspondent photons [66]. A suppression of neutrons by a factor of about 2.5 is achievable without reducing the photon efficiency. The difference in the patterns between the two species is evident in Fig. 3.15. Finally, for each photon- or neutron-induced shower event, the probability was formed that this event came from the photon. The efficiencies in these probabilities for photon- and neutron-induced showers were simulated as a function of threshold on the photon probabilities and gave good photon ID with suppression of neutrons up to a factor of 4. It should be noted that the higher the neutron energy (viz., the more difficult the use of TOF), the better the proposed method works. It is envisioned that a Boosted Decision Tree method for the BCAL reconstruction will incorporate variables that will result in classifiers sensitive to neutron-photon separation [67].

## 3.4 Forward Calorimeter

### 3.4.1 FCAL Summary [22]

The main parameters and properties of the FCAL are given in Tables 3.6 and 3.7. The assembly drawing for the FCAL module is D000000106-1000.

Table 3.6: FCAL properties.

| Property | Value |
|---|---|
| Lead Glass F8-00 block dimensions | $4 \times 4 \times 45$ cm$^3$ |
| Lead Glass density | 3.61 g/cm$^3$ |
| Lead Glass radiation length | 3.1 cm |
| Lead Glass index of refraction | 1.62 |
| Radius of the array (59 blocks/2) | $\sim$ 118 cm |
| Beam hole 3×3 blocks | $12 \times 12$ cm$^2$ square |
| Photomultiplier tube operating voltage | 1300-1900 V |
| Magnetic shielding | 1026 steel, 3 mm thickness ave. over square |
| Magnetic shielding | 0.36 mm AD-MU-80 $\mu$-metal |
| Dark room enclosure | 5 (deep) × 9 (wide) × 11 (high) ft$^3$ |
| Energy resolution $\sigma_E/E$ | $5.6\%/\sqrt{E} \oplus 3.5\%$ |
| Time resolution $\sigma_t$ | $\sim$0.4 ns for 100 mV |
| Position resolution | 6.4 mm $/\sqrt{E}$ |

Table 3.7: FCAL channel counts.

| Description | Type | Quantity |
|---|---|---|
| Lead glass blocks | Lead glass F8-00 | 2800 |
| Photomultiplier tubes | 12-stage FEU 84-3 | 2800 |
| Voltage dividers | Custom IU Cockcroft-Walton (C-W) bases | 2800 |
| Flash ADCs | JLab fADC250-MHz, 16 ch | 176 |
| Monitoring Plexiglas pane | UVT PMMA, $\approx 1.5 \times 1.5$ m$^2$, 1.3 cm thick | 4 |
| Monitoring violet LED | Satistronics SS-1206-UV, 10 per quadrant | $4 \times 10$ |
| Monitoring blue LED | Kingbright KPTD-3216QBC-D, 10 per quadrant | $4 \times 10$ |
| Monitoring green LED | Kingbright KPTD-3216MGC , 20 per quadrant | $8 \times 10$ |
| Monitoring controllers | Custom. One per quadrant, serves 40 LEDs | 4 |
| CAN-bus for C-W controls | ribbon cables (100 C-W bases per cable) | 28 |
| | bridge modules (4 ribbon cables per module) | 7 |

---

[22] *SVN revision ID:* tdr_summary_fcal.tex 13854 2014-06-12 04:42:15Z gen

## 3.5 Straw-tube Central Drift Chamber

### 3.5.1 CDC Summary [23]

The main parameters and properties of the CDC are given in Tables 3.8 and 3.9. The assembly drawing for the CDC is D000000102-1000.

Table 3.8: CDC properties.

| | |
|---|---|
| Straw Length | 150 cm |
| Straw ID | 15.55 mm |
| Wall thickness | 109 $\mu$m |
| Aluminum layer | 100 nm |
| Thickness (28 layers) | |
| Mylar | 2.22% Rad.Length |
| Gas | 0.34% Rad.Length |
| Thickness (End Plate) | 2.14% Rad.Length |
| Gas | 50% Ar / 50% $CO_2$ |
| Gas Flow | $\sim 3\ \ell$/min |
| Preamps (GASS-2) | 149 cards |
| fADC125-MHz, 72 ch | 50 modules |
| HV CAEN A1550P | +2110V |
| LV, MPOD MPV8008 | < 8V, 0.47A/card |
| Drift position $\sigma$ | $\sim 150\ \mu$m |

Table 3.9: CDC channel counts.

| Layer | Type | Straws |
|---|---|---|
| 1 (inner) | Axial | 42 |
| 2 | Axial Close Packed | 42 |
| 3 | Axial | 54 |
| 4 | Axial Close Packed | 54 |
| 5 | Stereo +6° | 66 |
| 6 | Stereo Close Packed | 66 |
| 7 | Stereo +6° | 80 |
| 8 | Stereo Close Packed | 80 |
| 9 | Stereo -6° | 93 |
| 10 | Stereo Close Packed | 93 |
| 11 | Stereo -6° | 106 |
| 12 | Stereo Close Packed | 106 |
| 13 | Axial | 123 |
| 14 | Axial Close Packed | 123 |
| 15 | Axial | 135 |
| 16 | Axial Close Packed | 135 |
| 17 | Stereo -6° | 146 |
| 18 | Stereo Close Packed | 146 |
| 19 | Stereo -6° | 158 |
| 20 | Stereo Close Packed | 158 |
| 21 | Stereo +6° | 170 |
| 22 | Stereo Close Packed | 170 |
| 23 | Stereo +6° | 182 |
| 24 | Stereo Close Packed | 182 |
| 25 | Axial | 197 |
| 26 | Axial Close Packed | 197 |
| 27 | Axial | 209 |
| 28 (outer) | Axial Close Packed | 209 |
| Total | | 3522 |

---

[23] *SVN revision ID:* tdr_summary_cdc.tex 14127 2014-07-15 18:59:42Z dugger

### 3.5.2 Overview

The Central Drift Chamber (CDC) is used to track charged particles, providing timing and energy loss measurements. The CDC is a cylindrical straw-tube drift chamber situated within the upstream end of the GlueX solenoid. It surrounds the target and start counter, as shown schematically in Figure 3.16, with dimensions given in Table 3.10. Its active volume is traversed by particles coming from the target with polar angles between 6° and 168°, with optimum coverage for polar angles between 29° and 132°.

Prior to construction of the CDC, the materials were evaluated and used to build two smaller prototype chambers. These prototypes were then used to study chamber characteristics and performance, including choice of gas mix and dE/dx simulations, reported elsewhere [68].

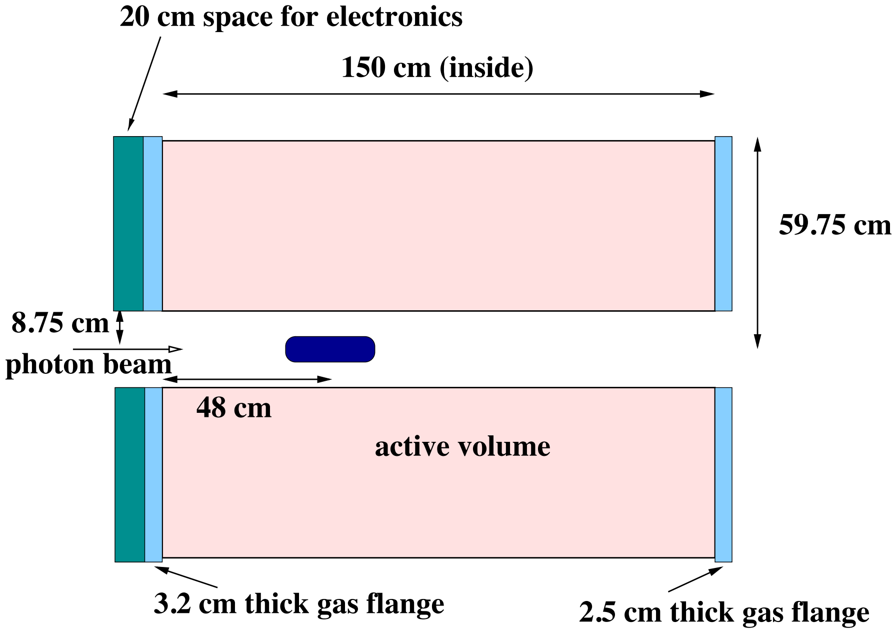

Figure 3.16: A side view of the CDC.

| | |
|---|---|
| Active volume inner radius: | 9.92 cm |
| Active volume outer radius: | 55.54 cm |
| Active length: | 150.0 cm |
| Chamber assembly inner radius: | 8.75 cm |
| Chamber assembly outer radius: | 59.74 cm |
| Upstream gas plenum length : | 3.18 cm |
| Downstream gas plenum length : | 2.54 cm |

Table 3.10: Geometry of the CDC's active volume and gas plenums

The CDC contains 3522 straw tubes of diameter 1.6 cm in 28 layers, located in a cylindrical volume with an inner radius of 10 cm and outer radius 56 cm, as measured from the beamline. Each straw tube contains an anode wire of 20 $\mu$m diameter gold-plated tungsten. The inner wall of the tube forms the cathode, ensuring uniformity of electric field around the wire. The straws contribute structural rigidity to the assembly, supporting the tension on the wires, and also prevent the wires from making contact with their neighbors, which would cause electrical problems in the event that one should break. The number of straws within each layer is given in Table 3.11.

| Layer | Straws | Radius (cm) | Layer | Straws | Radius (cm) |
|---|---|---|---|---|---|
| 1 | 42 | 10.7219 | 15 | 135 | 34.4343 |
| 2 | 42 | 12.0797 | 16 | 135 | 35.8128 |
| 3 | 54 | 13.7802 | 17 | 146 | 37.4446 |
| 4 | 54 | 15.1447 | 18 | 146 | 38.8314 |
| 5 | 66 | 16.9321 | 19 | 158 | 40.5369 |
| 6 | 66 | 18.3084 | 20 | 158 | 41.9248 |
| 7 | 80 | 20.5213 | 21 | 170 | 43.6152 |
| 8 | 80 | 21.9009 | 22 | 170 | 45.0038 |
| 9 | 93 | 23.8544 | 23 | 182 | 46.6849 |
| 10 | 93 | 25.2362 | 24 | 182 | 48.0737 |
| 11 | 106 | 27.1877 | 25 | 197 | 50.3747 |
| 12 | 106 | 28.5712 | 26 | 197 | 51.7597 |
| 13 | 123 | 31.3799 | 27 | 209 | 53.3631 |
| 14 | 123 | 32.7577 | 28 | 209 | 54.7464 |

Table 3.11: The number of straws in each layer of the CDC, and the central radius of each layer, as measured from the beamline at a point halfway between the endplates.

The tracking volume is enclosed by an inner wall (‘shell’) of G-10, an outer wall (‘shell’) of aluminum, a downstream carbon fiber endplate, and an upstream aluminum endplate. The endplates are linked by 12 aluminum support rods which were bolted into place to maintain the relative location and orientation of the endplates after alignment. Fig. 3.17 shows the endplates, inner shell, and support rods before the straws were installed. The holes in the endplates were milled precisely to position the ends of the straws correctly.

There is a cylindrical gas plenum next to each endplate - the upstream plenum has polycarbonate walls and a polycarbonate endplate, while the downstream plenum has Rohacell sidewalls and a ring-shaped end-wall of mylar film, aluminized on both sides. The inner and outer shells are sealed along their seams and where they meet the endplates, forming an outer plenum around the straws. The materials used for construction were chosen to minimize the amount of material in the tracking volume, especially at the downstream end. They are listed in Table 3.12.

A length of 20 cm is reserved for the electronics, which are mounted on standoffs on the polycarbonate endplate. Threaded holes in the polycarbonate endplate allow signal wires to pass through the gas plenum. These are sealed with an O-ring and a threaded bushing which is torqued into place.

Figure 3.17: CDC frame prior to the installation of the straw tubes.

### 3.5.3 CDC construction

**Straws**

The straw tubes were manufactured by Lamina Dielectrics[24] from four layers of mylar tape wound into a tube. The innermost layer of tape has 100 nm of aluminum vapor-deposited onto the side that faces inwards. The total wall thickness of the tube is 109 $\mu$m and the inner diameter is 15.55 mm. The electrical resistance of each straw, from one end to the other, is between 75 $\Omega$ and 100 $\Omega$. The straws are arranged in 28 radial layers surrounding the inner shell, as shown in Fig. 3.18. 12 of the layers are axial (parallel to the beam axis) and the remaining 16 are placed at stereo angles of $\pm 6^\circ$. These are ordered such that the innermost 4 layers are axial, followed by (at increasing radius) 4 layers at $+6^\circ$, 4 layers at $-6^\circ$, 4 axial layers, 4 layers at $-6^\circ$, 4 layers at $+6^\circ$ and 4 axial layers. The layers are paired and located so that the first layer of each pair contains the largest number of straws possible for its radius, and the straws in the second layer are close-packed against those in the first. This is illustrated in Fig. 3.19.

A non-conductive epoxy is used to glue each straw tube to its neighbors within the same layer at three points evenly distributed along its length. In the first layer of each pair, every sixth straw is also glued to the straw behind it. In the second layer of each pair, every straw is glued to the straw behind it. Fig. 3.20 shows straws in opposing stereo layers 8 and 9 and Fig. 3.21 shows the outermost row of straws, with the outer shell partly installed. The number of straws in each layer is listed in Table 3.13, together with the radial distance of each wire, relative to the beamline at the center of the chamber, and at the inside face of the two endplates.

---

[24] www.lamina.uk.com

| | |
|---|---|
| Upstream endplate: | 0.9525 cm Al (3/8” plate) |
| Downstream endplate: | 0.6 cm Carbon Fiber |
| Support rods (12): | Al |
| Upstream inner hub | Al |
| Downstream inner hub | G-10 |
| Thickness of inner shell (mm): | 0.5 mm G-10 |
| Upstream outer hub | G-10 |
| Downstream outer hub | G-10 |
| Thickness of outer shell (mm): | 1.6 mm Aluminum 6061 |
| Outer shell joints: | Scotch 27 glass cloth electrical tape<br>5.04 cm wide strip of military duct tape<br>2.54 cm wide 1.27 mm thick Cu tape |
| Outer shell connections to endplate (21) : | approx. 3 cm x 2.54 cm x 0.05 mm Al tabs |
| Outer shell connections to endplate (2) : | approx. 3 cm x 2.54 cm x 0.05 mm Cu tabs |
| Straw tube (inner diameter): | 1.555 cm |
| Straw tube (material): | Aluminized Mylar |
| Straw tube (thickness): | 119(0.1) $\mu$m Mylar(Al) |
| Upstream donuts and feedthroughs (3522): | Al |
| Downstream donuts and feedthroughs (3522): | Noryl plastic |
| Pinholders (7044): | Noryl plastic |
| Crimp pins (7044): | Au plated Cu |
| Anode wires (3522): | 20 $\mu$m gold-plated W |
| Upstream plenum sidewall: | 3 mm Polycarbonate and 1.27 mm Cu tape |
| Upstream plenum endwall: | 15.8 mm Polycarbonate |
| Downstream plenum sidewall: | 2.54 cm Rohacell |
| Downstream plenum endwall: | 50 $\mu$ m Aluminized Mylar |
| Gas pipes (6): | Al, inner diameter 6.35 mm |
| Gas line widgets (6): | plastic |
| Gas line widgets (6): | Al |
| Hose barbs (6): | stainless steel |
| Thermocouples (10) | Constantan Cu-Ni, Kapton coating |
| Conductive epoxy: | 920-H |
| Non-conductive epoxy: | DP-190 (straw assembly) |
| Non-conductive epoxy: | DP-460NS (outer shell and hubs) |

Table 3.12: Construction materials

| Layer | Straws | Radius (cm) (center) | Radius (cm) (end plate) | Stereo (radians) |
|---|---|---|---|---|
| 1 | 42 | 10.7219 | 10.7219 | 0.00000 |
| 2 | 42 | 12.0797 | 12.0797 | 0.00000 |
| 3 | 54 | 13.7802 | 13.7802 | 0.00000 |
| 4 | 54 | 15.1447 | 15.1447 | 0.00000 |
| 5 | 66 | 16.9321 | 18.6765 | 0.10470 |
| 6 | 66 | 18.3084 | 20.1945 | 0.11314 |
| 7 | 80 | 20.5213 | 21.9827 | 0.10470 |
| 8 | 80 | 21.9009 | 23.4606 | 0.11168 |
| 9 | 93 | 23.8544 | 25.1226 | −0.10470 |
| 10 | 93 | 25.2362 | 26.5780 | −0.11072 |
| 11 | 106 | 27.1877 | 28.3070 | −0.10470 |
| 12 | 106 | 28.5712 | 29.7475 | −0.10999 |
| 13 | 123 | 31.3799 | 31.3799 | 0.00000 |
| 14 | 123 | 32.7577 | 32.7577 | 0.00000 |
| 15 | 135 | 34.4343 | 34.4343 | 0.00000 |
| 16 | 135 | 35.8128 | 35.8128 | 0.00000 |
| 17 | 146 | 37.4446 | 38.2650 | −0.10470 |
| 18 | 146 | 38.8314 | 39.6822 | −0.10855 |
| 19 | 158 | 40.5369 | 41.2959 | −0.10470 |
| 20 | 158 | 41.9248 | 42.7099 | −0.10826 |
| 21 | 170 | 43.6152 | 44.3216 | 0.10470 |
| 22 | 170 | 45.0038 | 45.7326 | 0.10801 |
| 23 | 182 | 46.6849 | 47.3455 | 0.10470 |
| 24 | 182 | 48.0737 | 48.7539 | 0.10779 |
| 25 | 197 | 50.3747 | 50.3747 | 0.00000 |
| 26 | 197 | 51.7597 | 51.7597 | 0.00000 |
| 27 | 209 | 53.3631 | 53.3631 | 0.00000 |
| 28 | 209 | 54.7464 | 54.7464 | 0.00000 |

Table 3.13: The number of straws in each layer of the CDC. The radius at the center is the wire location half-way between the two endplates. The radius at the endplates is where the wire passes through the end plate. For axial layers, both radii are the same. For the stereo layers, the radius at the endplate is larger than it is at the center.

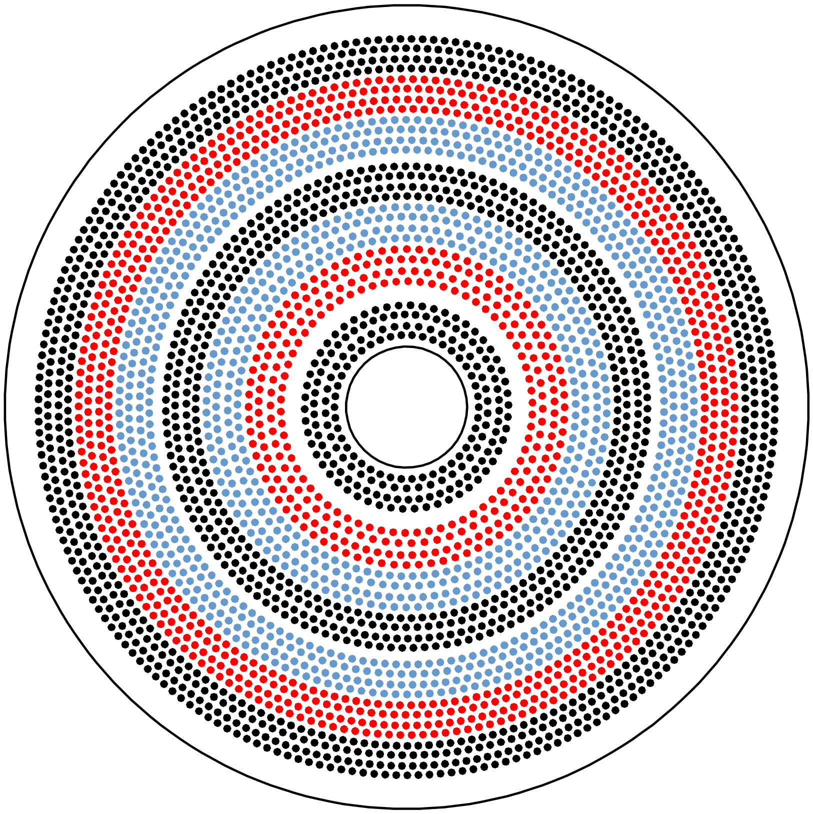

Figure 3.18: Diagram showing the position of the straws at the upstream endplate. The axial straws are shown in black, the +6° stereo layers are shown in red and the −6° stereo layers are shown in blue.

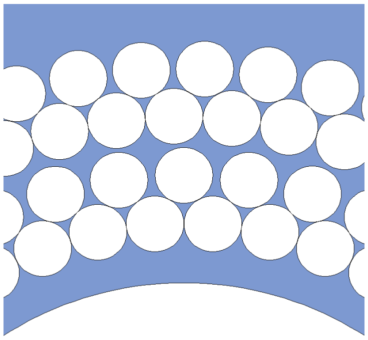

Figure 3.19: Diagram showing close-packing of the straws in a small section of rows 1 to 4.

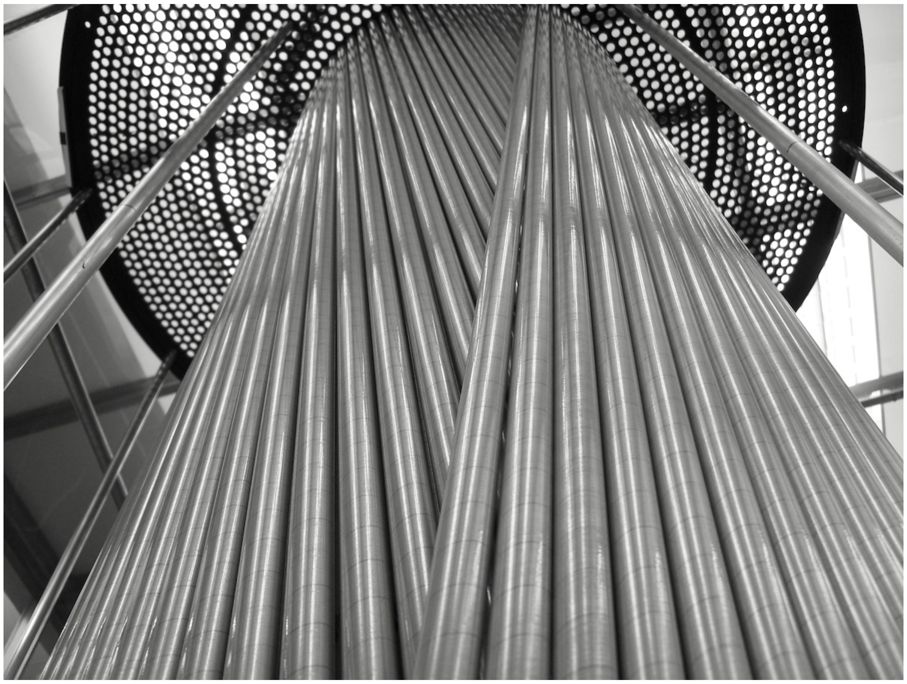

Figure 3.20: Straw tubes in stereo layers 8 and 9.

Figure 3.21: Straw tubes in layer 28, with one half of the outer shell in place.

### Straw and wire assembly

The straw assembly components are shown in Fig. 3.22. A 'donut' ring is glued inside each end of the straw, and a 'feedthrough' tube is glued through the endplate into the donut, and holds the straw in position. Depending on the endplate, there are two types of donuts, feedthroughs, and epoxy used: Noryl plastic donuts and feedthroughs are glued into the carbon fiber endplate with non-conductive epoxy, and aluminum donuts and feedthroughs are glued into the aluminum endplate with silver conductive epoxy. The conductive epoxy ensures that the electrical grounding of the aluminum endplate is shared with the aluminum feedthroughs, donuts, and the aluminum layer on the inside of the straw. Sufficient epoxy is used to make each joint gas-tight.

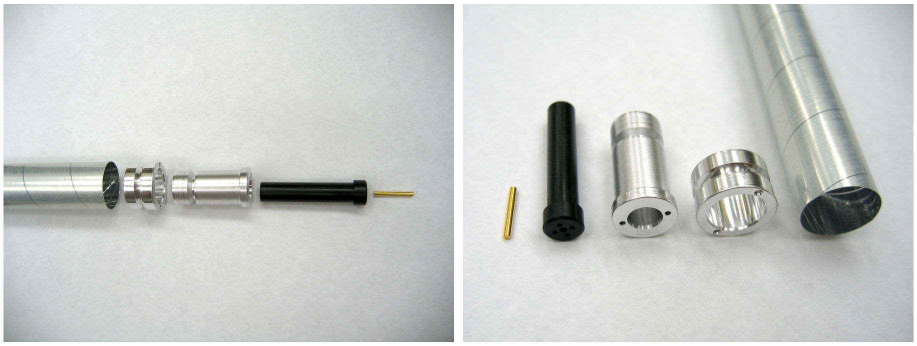

Figure 3.22: Straw, donut, feedthrough, pinholder and crimp pin.

The donuts and feedthroughs were manufactured to a CMU design which features a recess ('glue trough') partway down the outside of each component, accessed by 2 small holes ('glue-ports') bored lengthwise into the component wall. This permitted epoxy to be injected through one glue-port into the glue trough, allowing for air to exit through the partner glue-port, thus enabling a strong joint to form as the epoxy makes good contact with both surfaces. The dimensions of these components are given in Table 3.14.

| Component | Inner diameter | Outer diameter | Length |
|---|---:|---:|---:|
| Straw (straight) | 1.552 cm | 1.575 cm | 149.809 cm |
| Straw (stereo) | 1.552 cm | 1.575 cm | 150.571 cm |
| Donut (top) | 1.111 cm | 1.575 cm | 0.063 cm |
| Donut (rest) | 1.111 cm | 1.552 cm | 0.889 cm |
| Al feedthrough (top) | 0.635 cm | 1.270 cm | 0.254 cm |
| Al feedthrough (rest) | 0.635 cm | 1.111 cm | 2.159 cm |
| Noryl feedthrough (top) | 0.635 cm | 1.270 cm | 0.254 cm |
| Noryl feedthrough (rest) | 0.635 cm | 1.111 cm | 1.803 cm |
| Pinholder (top) | 0.147 cm | 0.787 cm | 0.396 cm |
| Pinholder (rest) | 0.508 cm | 0.635 cm | 2.906 cm |
| Crimp pin | 0.0203 cm | 0.147 cm | 1.206 cm |

Table 3.14: The dimensions of the straw assembly components

The anode wires are held in place by gold-plated copper crimp pins inside Noryl plastic tubes 'pinholders', which were inserted into the feedthroughs. The inner diameter of the pinholder top is at first 1.47 mm, a very close fit with the crimp pin, then after 6 mm of length the diameter is reduced to 1.27 mm for a further length of 1.63 mm to hold the crimp pin in place, before opening out to a diameter of 5.08 mm for the rest of the length.

The pins were crimped when the wire was under tension, applied by suspending a 30 g weight from the wire, with the chamber orientated so that the wire was hanging vertically. The anode wire is 20 $\mu$m diameter tungsten with a flash coating of gold, supplied by Luma-Metall[25]. Each pinholder has 4 additional holes surrounding the crimp pin which permit gas to flow in and out of the straw.

### Wire tension measurements

The tension on each wire was measured a few weeks after stringing, and again some time later, using two Helmholz coils and a control device which alternated between applying a sinusoidal voltage along to the wire and measuring the induced current on the wire. The wire tension was calculated from the frequency of the applied voltage when the system reached resonance. This technique is described elsewhere [69]. The tension measurements were interleaved with the stringing work and a few wires with very low tension were found and replaced during this time. When stringing was complete the tension on each wire was between 0.265 N and 0.294 N. The chamber is shown with the Helmholz coils in place in Fig. 3.23.

---

[25] www.luma-metall.se

Figure 3.23: Wire tension measurement

#### Gas flow

Six aluminum tubes of inner diameter 6.35 mm run the length of the CDC, close to the inside wall of the outer cylindrical shell, taking the gas supply from outside the upstream end through the polycarbonate plate and both endplates into the downstream plenum, where the gas enters the straw tubes through the holes in the pinholders. The gas passes through the straw tubes into the upstream plenum and then through ten holes in the lower half of the aluminum endplate into the void between the straws and the outer shell of the CDC. Six holes near the top of the aluminum endplate permit the gas to leave the void through exhaust tubes. Five thermocouples within each plenum enable the temperature of the gas to be monitored. The gas used is a mixture of 50 % $CO_2$ and 50 % Ar at atmospheric pressure.

#### Electrical shielding

Electrical shielding is required to minimize the amount of electromagnetic noise picked up by the signal wires. The aluminum endplate is the common ground for the straw tubes and also the outer shell, which provides electrical shielding around the tubes. Each half of the outer shell is glued to the aluminum endplate and G-10 outer hub with non-conductive epoxy. In order to ensure a good electrical connection, tabs of aluminum are glued over the join between the outer shell and the endplate with conductive epoxy at twenty points around the outer radius.

The long straight edges of the two halves of the outer shell were covered with non-conductive glass-cloth electrical tape and then joined together with a layer of 2 inch wide military duct tape. A strip of 1 inch wide copper tape with a non-conductive backing was applied along the center of the duct tape. The copper tape is grounded to the endplate by a tab of copper attached with conductive epoxy and then covered over with two more layers of the military duct tape. This arrangement ensures that the sidewalls of the cylindrical outer shell have a good connection to the grounded aluminum endplate, while the discontinuity between the two halves of the shell prevents eddy currents from spiraling around the CDC in the event of a magnet quench.

The upstream outer gas plenum sidewall is covered with 0.005 inch thick copper tape. A copper braid is soldered to the tape at intervals and glued to the aluminum endplate with conductive epoxy. The downstream plenum endwall material is mylar, aluminized on both sides. Rectangular tabs extend outwards from the endwall around its radius. These are glued to the sidewall and outer shell with conductive epoxy.

Grounded shielded extension cables are used for the downstream thermocouples along the length of the CDC, and for all the thermocouples from the upstream end to the electronics racks, in order to minimize any electrical pickup.

### 3.5.4 Electronics

The hookup wires, which pass through the polycarbonate endplate and onto the crimp pins inside the upstream gas plenum, were made from RG-316 wire as follows: at one end of the wire, the inner conductor was exposed for approximately 5 mm and the teflon dielectric was exposed for a further 5 mm. The end of the shielding braid was sealed with epoxy to prevent gas from migrating along the cable inside the braid. A silver bead was soldered onto the end of the center conductor and then covered with a narrow tube of conductive rubber, approximately 15 mm long, which fits tightly over the bead. Heat-shrink was then used to seal over the region from the end of the outer covering and braid to the end of the conductive rubber tube. An O-ring and threaded bushing were fed onto the hookup wire before its other end was finished by stripping back the braid 10 mm and then soldering a ferrule to the braid, then stripping the dielectric 5 mm from the end of the wire. Two hookup wires, one complete and one partly assembled, are shown in Fig. 3.24. The length of wire used for each connection was between 9.3 cm and 12.5 cm; this was chosen to be as short as possible, without causing excessive strain on the solder joints.

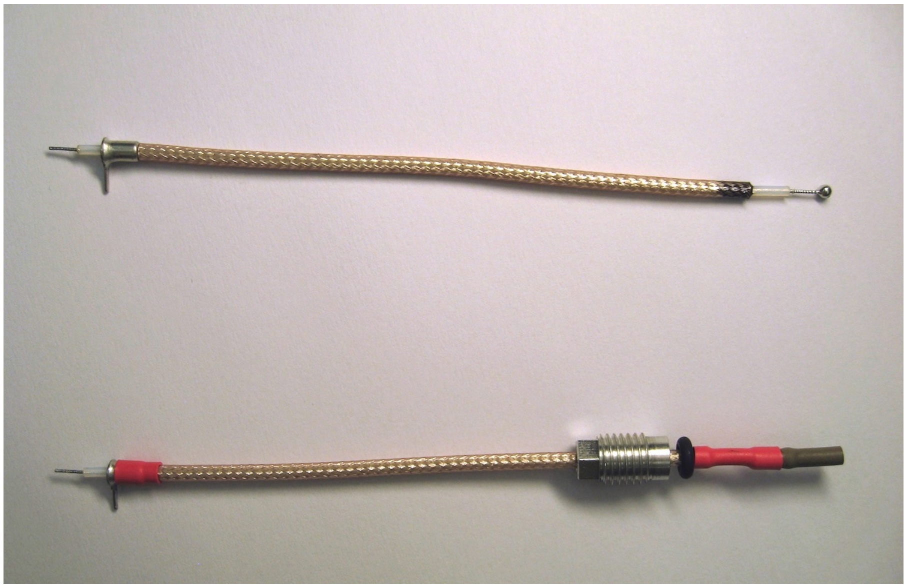

Figure 3.24: Two hookup wires, the upper wire is part-assembled and the silver bead is visible.

The polycarbonate endplate was polished to transparency so that the crimp pins would be clearly visible through it. Each hookup wire was installed by inserting it through a threaded hole in the polycarbonate endplate and sliding the conductive rubber over the corresponding crimp pin until it made a snug fit as the silver bead made contact with the end of the pin. The O-ring and threaded bushing were then fitted into the hole in the endplate, and the ferrule and center conductor at the other end of the hookup wire were soldered onto pads of a transition board. The transition boards are mounted onto standoffs located on the polycarbonate endplate - one standoff mounts directly to the polycarbonate endplate while the other (grounding) standoff threads onto another standoff which is mounted onto the Al endplate and protrudes through a hole in the polycarbonate endplate, sealed with an O-ring.

There are 149 transition boards with each board having between 20 to 24 hookup wires soldered to it. The hookup wires that are attached to any given transition board come from 3 to 4 neighboring rows of straws. Some of the transition boards and standoffs are shown in Fig. 3.25. Each transition board houses a 30-pin connector for installation of a high voltage board (HVB) that provides approximately 2 kV for up to 24 wires, 2 connections of approximately 2 kV for the shielding braids, 2 ground connections to the grounding standoffs and 2 unused connections which are located between the HV and ground connections. In addition to providing voltages, the HVBs also house the preamplifier cards.

The preamplifiers have 24 channels per board, are charge-sensitive, and capacitatively coupled to the CDC. The preamplifiers are connected to 125 MHz 12-bit flash ADCs, with

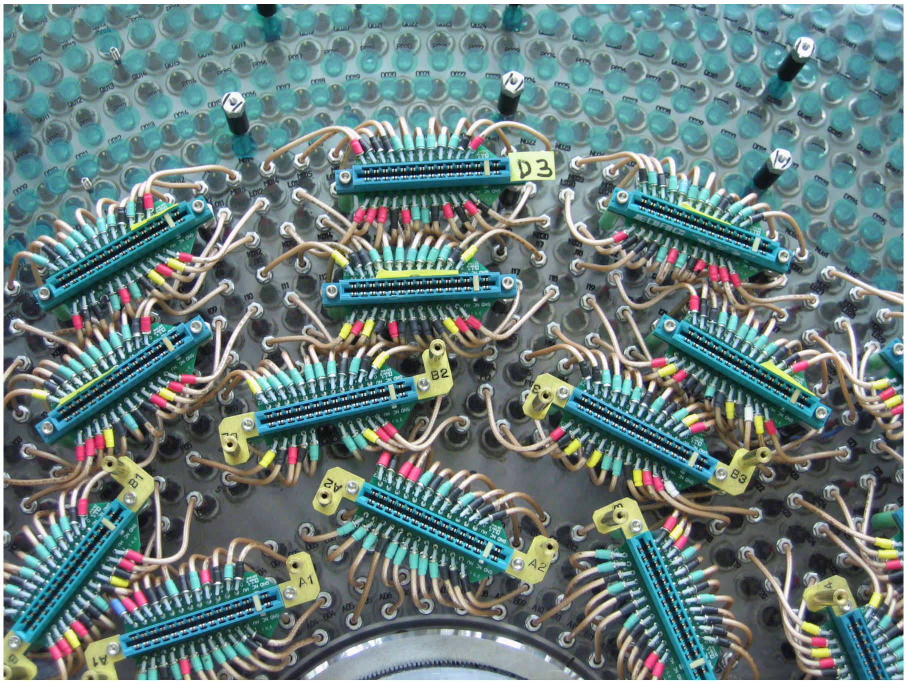

Figure 3.25: Hookup wires and transition boards.

three preamps to each fADC. The preamplifiers and fADCs are described in detail in the section on electronics.

### 3.5.5 Chamber operating parameters

The background noise present on the wires is important in determining the operating parameters for the CDC, and thus the range of dE/dx measurements possible. During calibration, measurements are made of the mean and standard deviation ($\sigma$) of the pedestal height (the ADC value in the absence of an event). The pedestal height is adjusted by downloading a data file into the fADC, it is set at approximately $3\sigma$ to $4\sigma$ in order to maximize use of the fADC range.

The choice of the gas mixture is described elsewhere [68]. The anode voltage is chosen such that the minimum ionizing peak in the amplitude histogram, from tracks at 90° to the straws, lies above the background noise. This is done by setting the anode voltage to match the hit threshold, typically $5\sigma$, to a low percentile (1% to 5%) of the distribution within the 4095 channel range of the fADC. Table 3.15 shows estimates of the dynamic range for conditions typical of the small prototype chamber operating at voltages close to $2\,kV$ with a gas mixture of $50\,\%$ $CO_2$ and $50\,\%$ Ar at atmospheric pressure giving a gas gain of approximately $3 \times 10^5$, and the $5\sigma$ hit threshold matched to the $1^{st}$ percentile. For $\sigma$ of 15 channels this gives a dynamic range of approximately 20 times minimum ionizing at 90°. Table 3.16 shows similar estimates for the hit threshold matched to the $5^{th}$ percentile, which gives greater dynamic range at the expense of detection efficiency for the minimum ionizing particles.

| Pedestal $\sigma$ | Minimum ionizing peak | Dynamic range |
|---|---|---|
| 10 | 140 (170 to 120) | 30 (24 to 34) |
| 15 | 210 (250 to 180) | 20 (16 to 22) |
| 20 | 280 (340 to 240) | 15 (12 to 17) |
| 25 | 350 (420 to 300) | 12 (10 to 13) |
| 30 | 420 (500 to 360) | 10 (8 to 11) |

Table 3.15: Table of estimates of the dynamic range of the CDC. There is some variation due to the shape of the Landau distribution, the data are given for ratios of the Landau parameters 4MPV/FWHM of 3.3 (3.0 to 3.6) and the $5\sigma$ hit threshold is matched to the $1^{\mathrm{st}}$ percentile of the distribution within the range of the fADC, where MPV is the most probable value

| Pedestal $\sigma$ | Minimum ionizing peak | Dynamic range |
|---|---|---|
| 10 | 90 (100 to 90) | 44 (41 to 47) |
| 15 | 140 (150 to 130) | 29 (27 to 32) |
| 20 | 180 (200 to 170) | 22 (20 to 24) |
| 25 | 230 (350 to 210) | 18 (16 to 19) |
| 30 | 280 (300 to 260) | 15 (13 to 16) |

Table 3.16: Table of estimates of the dynamic range of the CDC. There is some variation due to the shape of the Landau distribution, the data are given for ratios of the Landau parameters 4MPV/FWHM of 3.3 (3.0 to 3.6) and the $5\sigma$ hit threshold is matched to the lower $5^{\mathrm{th}}$ percentile of the distribution within the range of the fADC, where MPV is the most probable value

### 3.5.6 Timing method and position resolution

The fADCs are programmed to output data in two alternative modes - a ‘raw’ mode, intended for development and diagnostics, where a full sample window of 512 samples is read out for each channel, and a ‘run’ mode, where the output consists of only a few quantities, representing drift time, pedestal height and integrated charge, for only those channels where a hit occurs. The algorithms used to determine the drift time and energy loss were developed using the small 24-channel prototype chamber and are included in the fADC firmware. The drift time is converted into a drift distance in offline software.

The timing algorithm is activated by the trigger signal and performs a search through the raw sample data buffered in the fADC to identify a hit signal, if there is one, and return the time corresponding to its leading edge. It uses several thresholds which can be related to the pedestal standard deviation, $\sigma$. These are determined during calibration and uploaded into the fADC firmware as constants. Values optimized using the small prototype are available as a starting point: hit identification threshold $T_{hit} \sim 5\sigma$, high timing threshold $T_h \sim 4\sigma$, low timing threshold $T_l \sim \sigma$ and pedestal lead time $N_p \sim 4$ for $\sigma$ of 15. The hit search window, $W_s$ to $W_e$, specifies the range of samples to be searched for a hit, following the trigger.

1. The event pedestal, $P_{evt}$, is found, as the mean of 4 samples ending at the start of the hit search window, sample $W_s$.

2. The samples within the hit search window are searched for a hit, which is found if the data exceed a high threshold $P_{evt} + T_{hit}$ at point $x$. If no hit is found, no further action is taken.

3. The local pedestal, $P_{loc}$, is obtained as the ADC value at $N_p$ samples before $x$.

4. The algorithm searches through the samples from $x - N_p$ toward $W_e$ to find sample $x_h$, where the ADC value first exceeds or equals the high timing threshold, $P_{loc} + T_h$. If this is not found, the algorithm returns an error code and the value of $10(x_h - T_{const})$. The value of $T_{const}$ is set in configuration parameters.

5. It then searches the samples from $x_h$ back toward $x - N_p$ to find sample $x_l$, where the ADC value is less than or equal to the low timing threshold, $P_{loc} + T_l$.

6. The ADC data are upsampled by a factor of 5 to calculate values at $1.6\,ns$ intervals, from $x_l - 0.2$ to $x_l + 1.2$.

7. The upsampled values are searched from $x_l + 1.2$ down to $x_l - 0.2$ to find the point where the values fall equal to or below $P_{loc} + T_l$, and then interpolated to find the threshold crossing to the nearest tenth of a sample. This quantity is returned by the algorithm as an integer.

The time quantity returned by the algorithm is converted to a time in offline software by multiplying by 0.8 ns, which is one tenth of the sample period. It includes a constant offset, corresponding to the earliest possible drift time (when a track passes through a wire). This offset is determined during offline analysis and subtracted from the drift time returned by the algorithm to give the net drift time, which is then converted to a drift distance using look-up tables calculated beforehand using a GARFIELD [70] model.

The CDC was designed to achieve a position resolution of 150 $\mu$m. Data obtained with the small prototype and cosmic rays and analyzed with a simple straight-line track-fitting code give a position resolution which averages around 110 $\mu$m; the resolution improves with track distance from the wire, and also signal amplitude, as shown in Fig. 3.26.

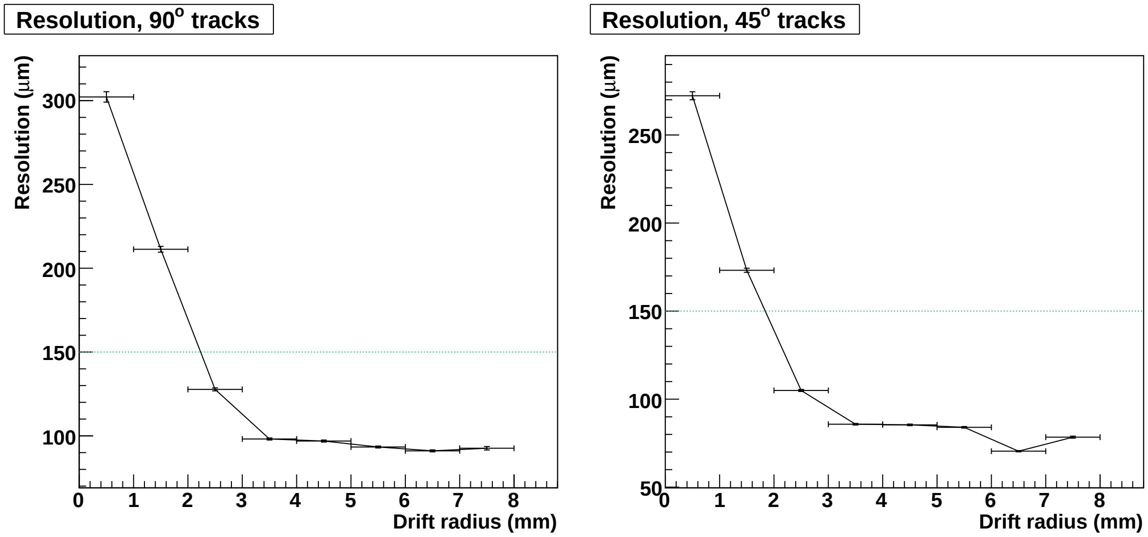

Figure 3.26: Position resolution for cosmic rays with 50/50 mix of Ar and $CO_2$ at 2090V, with tracks at $90^o$ (left) and $45^o$ (right) to the wires.

## 3.6 Forward Drift Chambers

### 3.6.1 FDC Summary [26]

The main parameters and properties of the FDC are given in Tables 3.17 and 3.18. The assembly drawing for the FDC package is D000000103-1030.

Table 3.17: FDC properties.

| Item | Value |
|---|---|
| Gas | 40% Ar /60% $CO_2$ |
| Gas flow | $\sim 4\times$ 0.23 $\ell$/min |
| Sense voltage range | +2100 to +2200 V |
| Field voltage range | 0 to -500 V |
| Sense wire pitch | 10 mm |
| Distance between sense and field wires | 5 mm |
| Cathode strip width | 4 mm and 1 mm gap |
| Cathode thickness | 2 $\mu$m Cu on 25 $\mu$m Kapton |
| Distance between wire and cathode planes | 5 mm |
| Cathode central area with no copper, diameter | 2.6 cm |
| Insensitive area (thick signal wires) packages 1-2, diameter | 6.0 cm |
| Insensitive area (thick signal wires) packages 3-4, diameter | 7.8 cm |
| Material in the active area (normal) | 4× 0.43 (% r.l.) |
| Material in the 2.6 cm diameter central area | 4× 0.26 (% r.l.) |
| Preamps cooling: liquid (Fluorinert) 24°C | 0.5 $\ell$/s |
| Wire position resolution | 200 $\mu$m |
| Cathode position resolution | 280 $\mu$m |
| Resolution along wire | 200 $\mu$m |

Table 3.18: FDC channel counts.

| Item | Description | Quantity |
|---|---|---|
| Package | 6 Cathode-Wire-Cathode assemblies at 0,60,120,180,240,300° | 4 |
| Sense wires | 20 $\mu$m gold-plated W | 96×6×4 |
| Sense wire HV | CAEN A1550P, 24 ch | 4 |
| Field wires | 80 $\mu$m gold-plated Cu-Be | 97×6×4 |
| Field wire HV | CAEN A1550N, 24 ch | 4 |
| U Cathodes | 75° to wires, central 24 strips are split in the middle | 216×6×4 |
| V Cathodes | -75° to wires, central 24 strips are split in the middle | 216×6×4 |
| Preamp Cards | Card (24 ch) with 3 ASIC (GASS-2) @8 ch/chip | 528 |
| TDCs (Wires) | JLab F1TDC V3, 48 ch, 97 ps | 48 |
| Flash ADCs (Cath.) | JLab fADC125-MHz, 72 ch | 144 |
| LV Power | MPOD MPV8008, 8 ch, 5A/ch | 9 |
| FDC Vth | MPOD MPV8030, 8 ch, 2.5A/ch | 1 |

---

[26] *SVN revision ID:* tdr_summary_fdc.tex 13854 2014-06-12 04:42:15Z gen

### Overview

The Forward Drift Chamber system (FDC) is used to track charged particles coming from the target with polar angles up to 20°. Tracks at angles greater than 10° also pass through the CDC detector and its associated downstream end-plate. Due to the spiraling trajectories of the charged particles and the high multiplicity of charged tracks passing through the FDC, this system must be able to provide a sufficient number of measurements with appropriate redundancy to enable the linking of hits from the different tracks with high accuracy, while providing good spatial resolution with reasonable direction information. The chosen technology is a Cathode Strip Chamber in which the two cathode planes facing each wire plane are divided into strips at an angle with respect to the wires. In addition to the charge induced on the strips, the timing information from the wires is read out, enabling reconstruction of both a coordinate along the wire, as well as a coordinate transverse to the wire (using the drift time). This allows the reconstruction of “space points” and facilitates the association of adjacent hits with each other, thereby enhancing pattern recognition.

The most critical requirement in the FDC design is to minimize the amount of the material in the active area of the chamber and at the periphery: frames, supporting systems, and cables. At low momenta, the thickness of the detector in the active area limits the momentum resolution. Photons from meson decays may convert in the detector frames or other materials and may not be properly reconstructed by the BCAL due to the strong magnetic field. Therefore the amount of material at the periphery affects directly the efficiency of photon reconstruction. At the same time the mechanical structure must be robust enough to minimize the frame deformations and to allow for a good gas containment.

The central region of each chamber is close to the beam line and require a special configuration to handle the otherwise unmanageable rates on the strips in this region.

The chambers are positioned inside the bore of the solenoid where the strength of the magnetic field is largest. The direction of the magnetic field is roughly perpendicular to the wires. Not only does this affect the drift time of the electrons toward the wires but the Lorentz force causes a deflection of the avalanche position along the wire relative to the case where there is no magnetic field. The latter effect can be minimized with an appropriate choice of gas mixture. Further details are provided in Section 3.6.1.

The FDC detector includes four separate but identical [27] disk-shaped packages as shown in Fig. 3.27. Each package includes six independent planar drift chambers, or cells, with separate gas volumes. Each cell consists (Fig. 3.28) of a wire frame with alternating anode and field-shaping wires sandwiched between two cathode strip planes. Aluminized Mylar planes (ground planes) in between the cells shield the strips electrically and also separate the gas volumes of the different cells. Additional layers of thicker Mylar are added at the two ends of the package (end windows) to close and provide mechanical protection.

### Wire planes

The basic chamber element is a circular frame on which alternating sense and field wires are strung as cords across the chamber in one plane. Each plane contains 96 sense and 97 field wires, with the two side wires being field ones. The length of the sense wires varies from 20 cm to 97 cm. The sense wires are 20 $\mu$m diameter gold-plated tungsten, while the field wires are

---

[27] Except for the size of the deadened area on the wires discussed later

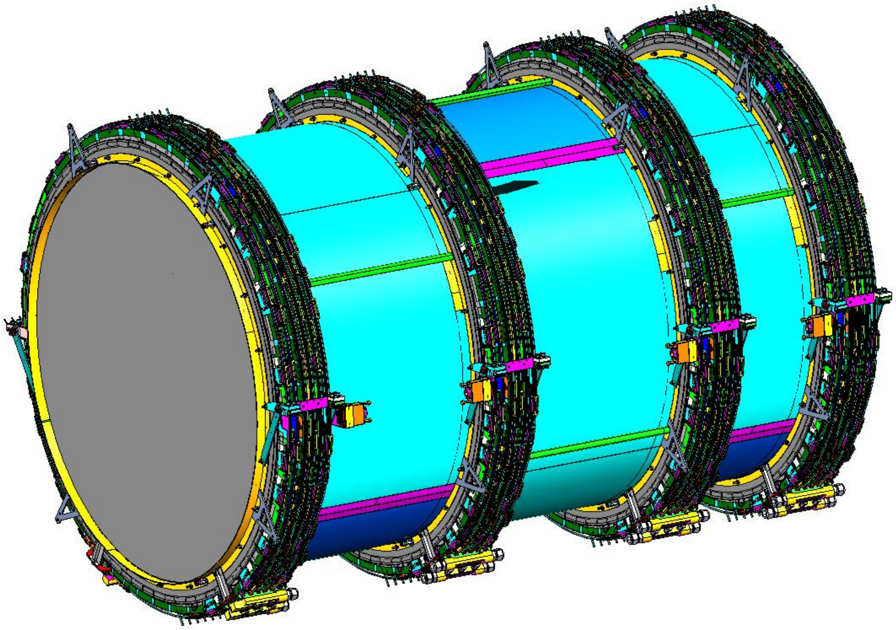

Figure 3.27: FDC detector: four tracking packages, each having six separate drift chambers (cells). The active area diameter is 97 cm with a total detector diameter of 120 cm, and total length of 174 cm.The positions of the second, third and fourth packages with respect to the first one are at: 58.43, 168.86, and 155.30 cm.

80 $\mu$m gold-plated copper-beryllium. The field-to-sense wire spacing is 5 mm and the distance to both cathodes is also 5 mm, resulting in a 10x10 mm$^2$ electric-field cell formed around the sense wires in a plane perpendicular to the wires. Positive HV is applied on the sense wires to achieve a gas gain of $\sim$5 $10^4$. Negative HV is applied on the field wires to improve the circular symmetry of the electric field in the cell (Fig. 3.29 right panel).

The frame containing the the sense and field wires is a 5 mm thick lamination (Fig. 3.30) consisting of three rings: a fiberglass (G10) ring, a Rohacell ring, and a printed circuit board (PCB) ring, with all three elements glued together [28]. The inner diameter of the frame is 100 cm with an outer diameter of 120 cm. To reduce the amount of the frame material, 80% of the fiberglass G10 ring thickness was milled from 4.14 mm down to 0.8 mm. The milled region was filled with sectors made out of Rohacell glued together [29] as a ring. The remaining 20% form a solid G10 ring that covers the holes for the mounting rods and mechanically supports the package assembly.

The PCB ring is formed by gluing [30] together six separate circuit boards. Two of the boards (4-layer PCB) are at the signal side of the wires, another two boards (2-layer PCB) are at the high voltage side of the wires, and the last two boards form the sides of the ring. As a first step, the G10 and Rohacell rings are glued together, after which the PCB ring is laminated to them.

The sense and field wires are strung between the high voltage and signal PCBs. First, the

---

[28] Using Hysol epoxy RE2039 resin and HD3561 hardener

[29] Using Scotchweld 1838 epoxy

[30] Scotchweld 1838 epoxy

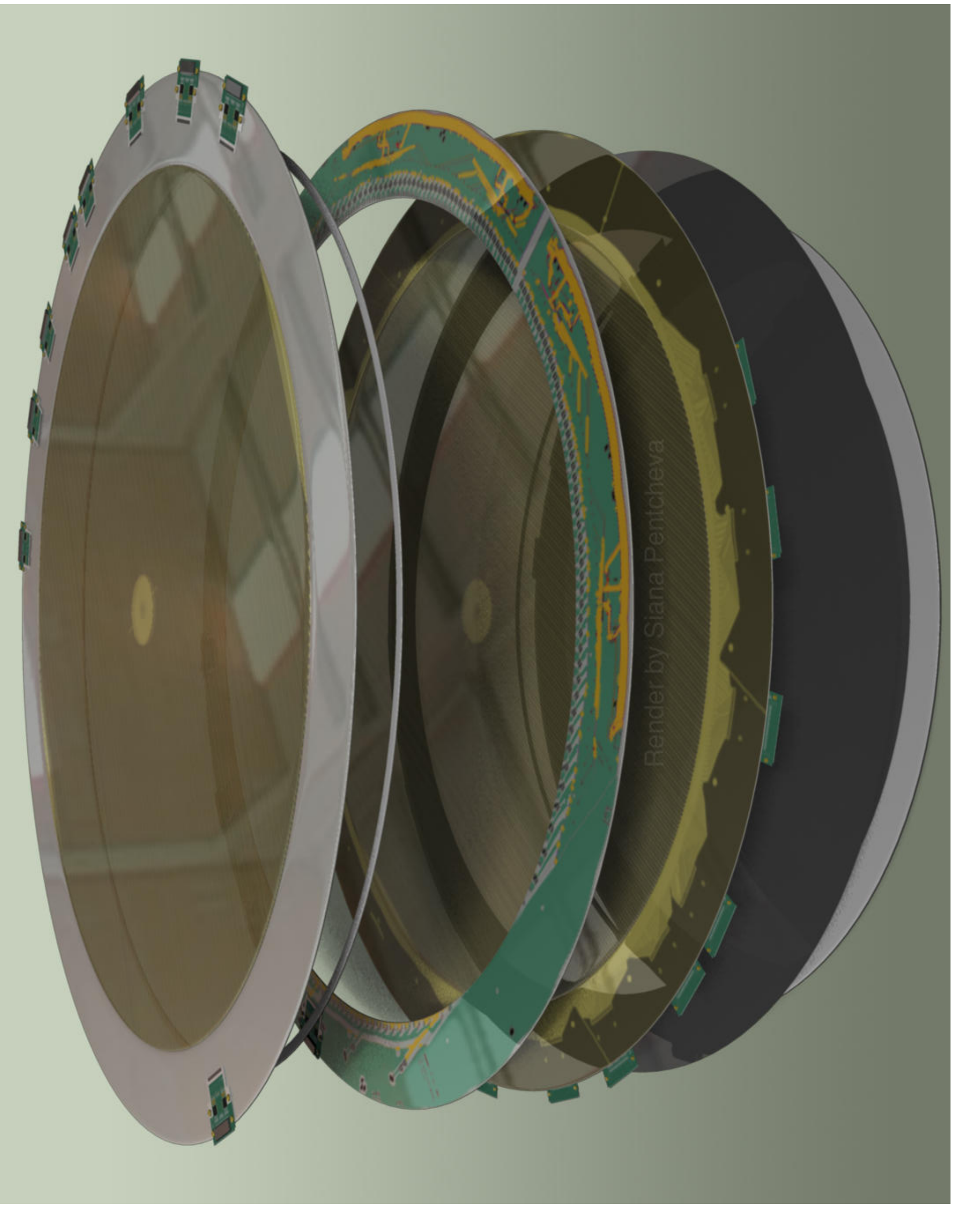

Figure 3.28: One detector cell (artistic view) from left to right: upstream cathode, spacer ring, wire plane, downstream cathode, ground plane (black disk) glued to the back of the downstream cathode, end window (gray) only at the end of the package.

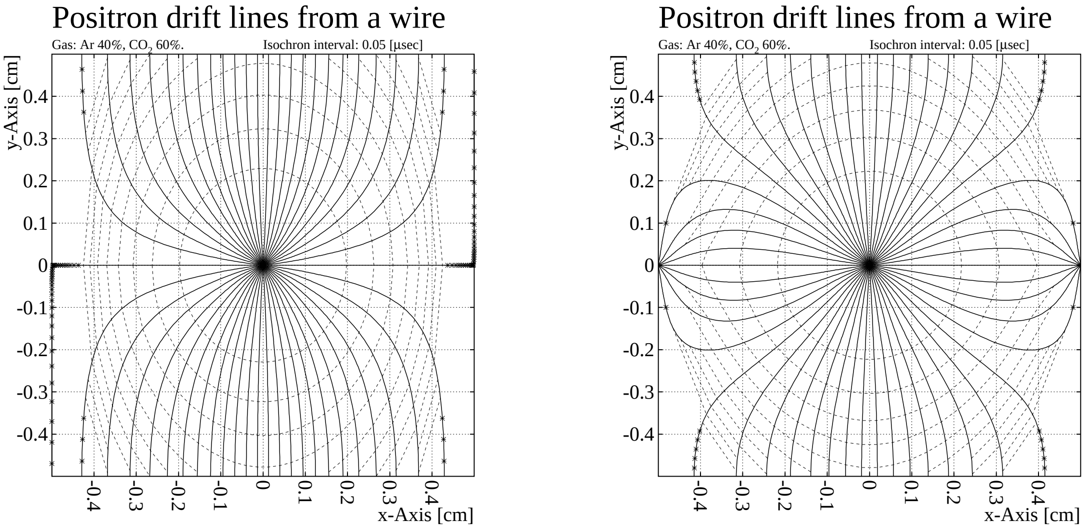

Figure 3.29: GARFIELD calculations of electric field lines (for a $B = -2.3$ T field configuration) within a square drift cell for a 40% argon - 60% $CO_2$ gas mixture for electrode configurations without (left) and with (right) field-shaping wires. The x-axis is perpendicular to the wires in the wire-plane, y-axis is along the beam line, with the sense wire at zero, and field wires at ± 5 mm.

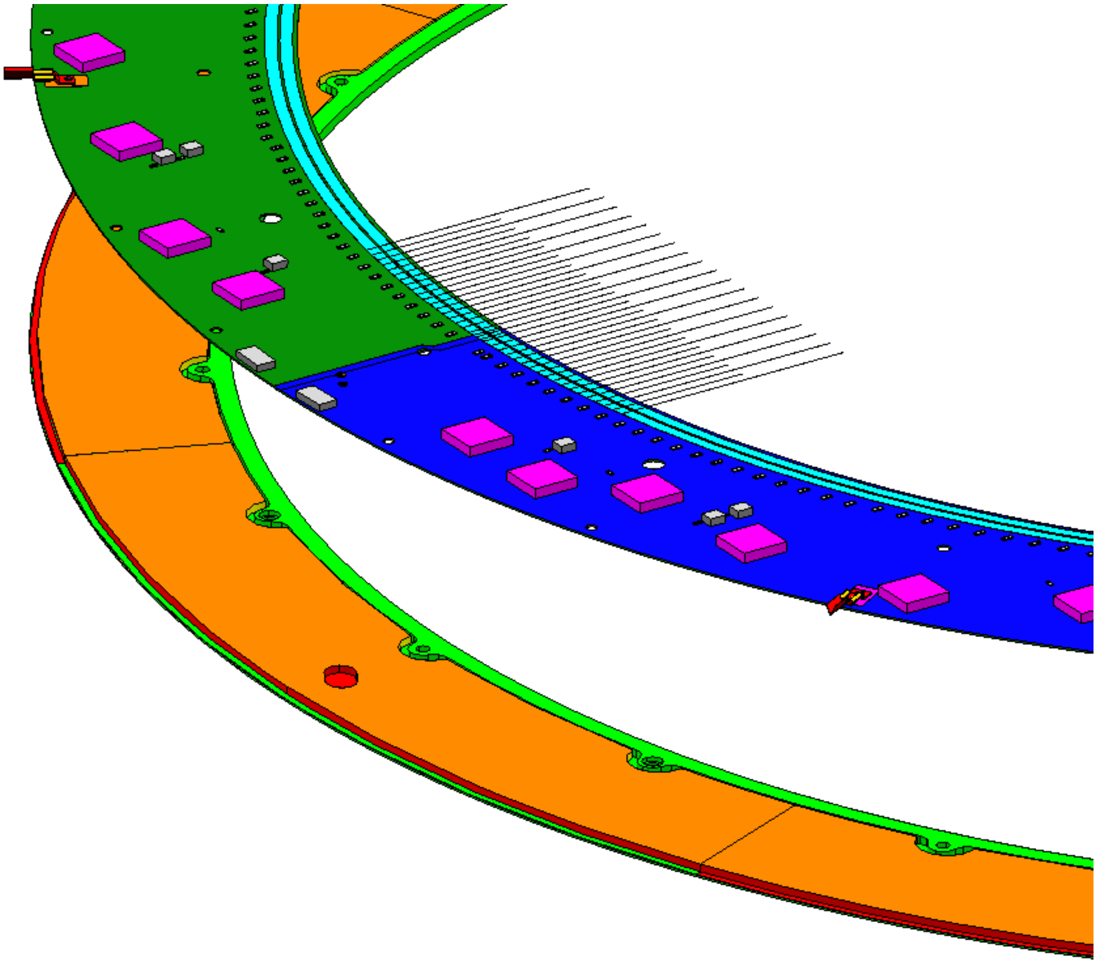

Figure 3.30: Wire frame lamination: PCB ring (top green and blue) with sense and field wires soldered on it (not all wires shown), Rohacell sectors (bottom orange with red sides), G10 frame (bottom green)

wire frame is mounted on a strong-back placed on a granite stringing table. Then the wires are strung above the frame between high precision pins attached with rails to the ends of the table. Next, the position of the strong-back (and the wire frame) is adjusted with respect the wires, and the frame is raised so that the wires are just touching the wire pads on the boards. At this position the wires are fixed to the boards by applying small adhesive Kapton dots. Then the wires are glued [31] and soldered [32] to the boards.

The wire positions are measured (and corrected if needed) using a stepper motor [33] attached to a worm gear with a sensor running across the wires. The positions are kept within 50 $\mu$m from the nominal value with a R.M.S. less than 25 $\mu$m. Tensions of 20 and 130 g (force) are applied on the sense and field wires respectively. They are checked using a permanent magnet placed close to the wire and applying variable current from a function generator, thus finding the main resonance frequency that is related to the tension. The measured tensions did not vary by more than 2 g for the sense and by 10 g for the field wires.

Each high voltage PCB is divided into two independent sectors supplying positive HV for 20 (inner) and 28 (outer) sense wires. Similarly, the negative HV supply is split in two on each board. In total, for each wire plane, there are 4 positive and 4 negative independent HV sectors connected to different channels on the HV supply.

The signal PCBs have HV capacitors separating the sense wires from the signal part of the board. The capacitors are positioned at the inner side of the PCBs, which is inside the gas volume. Due to improper soldering by the manufacturer that resulted in enhanced leakage currents, all the HV capacitors were replaced [34]. Each signal PCB has two connectors for the pre-amplifiers, each serving 24 sense wires; in total there are four connectors or 96 channels per wire plane. Protective resistors of 1 M$\Omega$ are installed on both HV and signal PCBs. These resistors limit the current on each sense and field wire to inhibit sparks.

### Cathode strip planes

The cathode planes are copper coated Kapton foils stretched on G10 frames. The cathode G10 frame is similar in shape to the wire G10 frame. It has a thick ring covering the mounting holes and thin periphery on which the Kapton foil is glued [35]. Unlike the wire frames, there is no Rohacell material in the cathode frames. The Kapton foil thickness is 25 $\mu$m while the copper layer is only 2 $\mu$m to minimize the amount of the material in the active region.

Due to the large size of the cathode, one cathode foil is made out of three separate foils. The three pieces are first cut, aligned together, and then attached by gluing [36] thin (25 $\mu$) Kapton tape over the non-copper side of the foils. Thus, the cathode foil is made as a circle with the copper layer forming the strips, grounds, traces and connectors. The foils, and therefore strips, are aligned with a precision better than 100 $\mu$m. The cathode foil is first glued to a transfer ring so that the surface tension can be set to 500 N/m, and then glued [37] to the cathode frame.

The optimum cathode readout pitch is determined by the width of the induced charge

---

[31] Epon Resin 828 and Versamid 140 hardener

[32] Almit Solder PN-KR19SHRMA Sn60-P2-0.3mm

[33] Parker S/SX 83-93 with ACR 9000 controller

[34] Using 220 nF AVX 1825JC102 rated for 4 kV except a few of the boards where AVX 1825HC102 rated for 3kV were used

[35] Using Hysol epoxy RE2039 resin and HD3561 hardener

[36] Using Hysol epoxy RE2039 resin and HD3561 hardener

[37] Using Hysol epoxy RE2039 resin and HD3561 hardener

distribution. It has been shown by several groups that minimal differential non-linearity is achieved when the cathode pitch is equal to the wire-cathode distance of 5 mm (e.g. [71]). This value is employed in the FDC design. Due to the higher rates, the central 24 strips are split in two halves. Thus, on one cathode there are 216 strips with lengths varying from 29 to 100 cm.

The strips have traces on one side leading to 24-channel connectors with the pads imprinted on the cathode. The strips are connected to the pre-amp cards with rigid-flex assemblies, each consisting of a flexible PCB (flex) and a daughter board on which the pre-amp is plugged. The flex part is needed to accommodate connection to the opposite side of the cathode frame (through an opening there) where there is space for the daughter boards to be installed. The soldering of the flex to the cathode is a delicate operation with some possibility of destroying the thin (2 $\mu$m) copper pads and thus the whole cathode. Therefore, the flexible sections are glued to the cathode pads using anisotropic conductive tape [38] that conducts only in the direction perpendicular to the surface. The tape is a head-bondable film with small ( 50 $\mu$m) silver-covered glass balls distributed randomly. After the tape is placed between the two contact areas, a specially designed tool is used, along with pressure and heat to make the bond between the contacts.

To investigate this new technology, samples were made and tested at significant temperature changes and irradiated up to 1 kRad (expected dose to be accumulated at this place of the detector in the hall for 10 years). During the cathode production it turned out that some of the channels may have a resistance on the contacts that varies from few Ohms to several tens of Ohms, depending on the pressure applied and deformation at the contact area. The tests show that this is not aging but a mechanical problem related to frame deformations when handling of the cathodes. To mitigate the problem, special tools were designed to keep the cathodes flat in all the operations after the cards are glued.

In addition to the type-1 cathode described above, there are two other types of cathodes that are described in the next subsection.

### Package design

The chamber elements described above are installed in the package forming six separate cells. In addition at the two sides of the package there are end windows: 2 mil aluminized Mylar stretched on G10 frames similar to those for the cathodes. The ground planes (0.5 mil aluminized Mylar) that separate the cells are part of the type-2 cathodes, a modification of the described above type-1 cathode, on the back side of which, 5 mm apart from the cathode foil, a 0.5 mil aluminzied Mylar foil is stretched and glued to the frame. All the cells have the same structure except the outer cathodes of the two outer cells. These are type-3 cathodes, a modification of the type-2 cathode with holes punched through the ground plane. In this way, the end windows accommodate the pressure difference between chamber and atmosphere.

Thus, starting from the upstream side, the package consists of:

- Upstream end window,
- cell #1 with type-3 cathode, spacer ring, wire frame, type-2 cathode
- cell #2 with type-1 cathode, spacer ring, wire frame, type-2 cathode
- ... same for cells #3, #4, and #5

---

[38] 3M Anisotropic Conductive Film Adhesive 7303 (5 mm width)

- cell #6 with type-1 cathode, spacer ring, wire frame, type-3 cathode
- Downstream end window

In each cell, the strips of the top and bottom cathode are oriented with respect to the wires at 75° and 105° respectively. Neighboring cells are rotated by 60° with respect to each other in order to improve track reconstruction on the corresponding anode wire left/right ambiguities, hence improving the overall resolution.

Each cell forms a gas volume (Fig. 3.31) separated from the neighboring cells by the ground planes. There are gas holes at the periphery of all cathode planes to equalize the pressure on both sides and keep the cathode foil flat. The gas containment of the package is achieved by Viton O-rings [39] installed in between all the chamber elements. There are O-ring grooves on one side of the the wire frames, type-1 cathodes and end-windows, and on both sides of the spacer rings. While testing the first production package it was found that there is significant oxygen contamination, up to few percent, inside the gas volume. It turned out that the oxygen penetrates between the O-rings and grooves especially on the G10 frames due to the fiber structure of the machined grooves. Therefore, the wire and cathode grooves are coated with epoxy [40]. In addition, vacuum grease [41] is applied on all the O-rings. Thanks to this, the oxygen contamination in a package is reduced down to a negligible level of less than 100 ppm.

At the same time, it was found that the combination of Viton O-ring and vacuum grease prevents the appearance of corrosion on the copper layer of the cathodes that faces the O-rings. Significant damage of the thin copper layer, especially at the traces leading to the connectors, was found on the first packages where EPDM O-rings were used, which required their refurbishment.

Two aluminum gusset rings (L-shape profile) at both sides of the package connected with 24 aluminum threaded rods through holes in all the package planes are used to compress the O-rings and hold the package elements together. Cuts are made in the gusset rings and then connected with carbon fibers to avoid closed loops inside the magnet.

The total thickness in the active area of each package in terms of radiation length is estimated to be ∼0.43 $\%X_0$ (Table 3.19), where $X_0$ is one radiation length. Most of it comes from the cathode materials, dominated by the $2\mu$m copper layer and then from the Kapton itself.

### Central chamber region

The region of the chamber close to the beam line requires special treatment. First, the material along the beam should be minimized to reduce the additional background production. There is no copper on the cathodes in the area around the beam line within 2.4 cm diameter. This reduces the material along the beam line to 0.26 $\%X_0$ per package (from Table 3.19), or 1.04 $\%X_0$ in total, to be compared to 3.5 $\%X_0$ thickness of the LH target.

Second, the detector itself should be insensitive near the beam line so that the rates on the electronic channels are reduced to a manageable level. The rates on the FDC have been studied by Monte Carlo simulations of the electromagnetic background [?]. A safe limit of ∼130 kHz was assumed for all the electronics channels. This requires insensitive areas with diameters 5.8

---

[39] Viton 55 durometer

[40] Hysol epoxy RE2039 resin and HD3561 hardener

[41] Apiezon-L

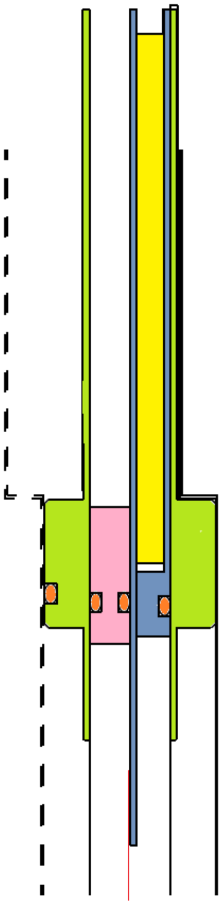

Figure 3.31: Cross-section showing separation of the different frames within one chamber cell. Top corresponds to the outer side of the detector, the gas volume is at the bottom side. From right to left: cathode type-2 (green frame) with ground and cathode foils on it (black lines), wire plane (blue frame with yellow Rohacell) with wires (red line), spacer ring (pink), cathode type-1 with cathode foil (black line), cathode type-2 from the next cell which ground foil and frame are shown with dashed line. The orange regions indicate the O-rings.

| Material (description) | Thickness $\mu$m | Quantity | Total cm | $X_0$ cm | Fraction of $X_0$ % |
|---|---|---|---|---|---|
| Kapton (on all cathodes) | 25 | 12 | 0.030 | 28.60 | 0.105 |
| Copper (on Kapton) | 2 | 12 | 0.0024 | 1.43 | 0.168 |
| Mylar (on type-2,3 cathodes) | 13 | 7 | 0.009 | 28.7 | 0.031 |
| Aluminum (on type-2,3 cathodes) | $< 0.1$ | 7 | $< 0.00007$ | 8.9 | $< 0.0008$ |
| Mylar (on end-windows) | 50 | 2 | 0.010 | 28.7 | 0.035 |
| Aluminum (on end-windows) | $< 0.1$ | 2 | $< 0.00002$ | 8.9 | $< 0.0002$ |
| Argon (gas mixture) | 13cm × 40% | 1 | 5.2 | 10944 | 0.047 |
| $CO_2$ (gas mixture) | 13cm × 60% | 1 | 7.8 | 18310 | 0.043 |
| Total | | | | | 0.430 |

Table 3.19: FDC material in the active area for one package

cm, 6 cm, 6.1 cm, and 7.8 cm respectively for the first, second, third, and fourth packages. To have two pairs of interchangeable packages it was decided the insensitive region of the first two packages to be 6 cm and for the last two packages 7.8 cm in diameter about the beam line.

An electroplating technique with copper sulfate solution was used to thicken the sense wires (Fig. 3.32) from 20 $\mu$m to ~80 $\mu$m, making the chamber insensitive in that region near the beam line. The procedure consists of several plating cycles intervened with polishing cycles in which the polarity is reversed. The current on the electrodes and the timing of the cycles

Figure 3.32: Wire deadening: a container filled with $CuSO_4$ is raised against the wires; voltage is applied between the sense wires and a copper electrode inside the container.

were optimized to obtain a smooth surface. A micro-controller system was developed [**?**] to control the electroplating procedure. After the procedure, the wires were cleaned with water and alcohol.

### Package subsystems

- Gas system.

  The six cells of the package are supplied with gas in parallel with manifolds at the supply and exhaust side. The gas enters the cell volume through nine 1 mm holes in the spacer ring of the cell (supply side) and exits the volume in the same way at the opposite side of the ring (exhaust side). In addition there is a hole in the spacer ring connected to an individual gas line that is used to monitor the internal pressure of each cell separately. We assume a nominal gas flow through one package of 250 sccpm (standard cubic centimeters per minute) and a pressure in each cell of $\sim 100$ Pa above atmospheric pressure..

- Grounding.

  To minimize the noise, the grounds of the wire and cathode planes are connected at many places at the periphery of the package. There are 16 connections per cell that bridge the grounds of the downstream cathode, wire frame, upstream cathode, and the downstream cathode of the next cell. The connections are done with 4 mil copper strips 1 cm wide pressed against the ground areas with clips. There are 16 additional connections per cell that bridge the elements of one cell on both sides (where possible) of the cathode readout cards. This is needed to ground the cards as close as possible to them. At the same time this provides mechanical strength of the cathode frame at the places where the cards are installed, thus avoiding deformation of the conductive tape contacts. In total there are about 200 such ground connections per package.

- Cooling system.

  The power dissipated by the pre-amplifier cards of one package is expected to be $\sim$200 W and therefore cooling is needed. Fluorinert [42] is used as coolant which compared to water, will avoid fatal damages of the detector and the electronics in case of leakage. Six copper tubes (one per cell) of 4 mm outer diameter and 0.6 mm wall thickness, are shaped as circles and installed around the package using brackets attached to the pre-amplifier cards. There are two plastic manifolds at the input (each serving three cells) and two at the output of the tubes connected to the Fluorinert supply. Care has been taken to avoid closed conductive loops. A nominal gauge pressure of 37 psi at the input and 4 psi at the output will allow temperature variations over the cooling loops to be less than $3^0$ C.

- HV connections.

  All the positive high voltage (HV) sectors of one package are connected to a Radial 52-pin connector mounted at one of the package holding brackets with wires running to the upstream side of the package. Each individual channel has connectors at the upstream side of the package which simplifies the package assembly and allows for additional testing of each HV sector. The wiring of the negative HV sectors is analogous. The wires are running to the downstream side and a 52-pin connector is attached to the other holding

---

[42] FC-770 by 3M

bracket. Two HV cables coming from CAEN A1550P/N HV units are connected to one package serving the 24 positive/negative HV channels of the package.

- LV connections.

  The low voltage (LV) of 3 V needed for the pre-amplifier cards (each drawing ∼0.5A) is distributed with 18 m long cables, each supplying four cards in parallel. In addition, the same cables are used to distribute the threshold voltage to the wire discriminator cards. Due to the space limitation for the LV connectors the thickness of the wires is limited such that a voltage drop along the cables is about ∼3 V. This increases the power dissipated inside the magnet by about 20%. Three types of cables are used that differ by the number of connectors (2 for the wire planes and 4 for the cathodes), and the distances between the connectors.

- Signal cabling.

  132 signal cables are connected to the pre-amps of one package. To reduce the stress on the connectors, the cables are tightened to the gusset rings and the package spacers. The cables are shielded with copper braid and thin aluminum tape, but the braid is removed for the part of the cables that are inside the magnet. The cables are subdivided into four quadrants and bundled together outside of the magnet.

- Fiducialization.

  Four prism reflectors are attached to the gusset rings of each package. Even when the detector is cabled and installed in the bore of the magnet, they can be surveyed from the downstream side in direction parallel to beam line with a precision of 0.1 mm.. Additional spherical targets have been attached to the gusset rings of each package during the initil detetctor survey.

### Readout Electronics

Two types of pre-amplifier cards are mounted on the chambers. One is for the strip readout which is a charge-sensitive preamplifier with pulse-shaping. It has a gain of 2.6 mV/fC, 130 fC dynamic range and 14 ns peaking time. The other type, used to read the sense wires, has a 0.77 mV/fC pre-amplifier with 260 fC dynamic range and in addition - a built-in discriminator that outputs LVDS signals. Both cards use GAS-II ASIC and have resistors that define the different settings.

The FDC readout will employ 100 *ps* F1 TDCs for the anode wire drift time readout and 125 MHz FADCs for the cathode readout. This enables commonality with the readout electronics of the other GlueX detector subsystems. Note that with a clock rate of 125 MHz on the FADCs, time fitting algorithms matched to the chamber pulse shape can be employed to provide a time resolution of ∼2 ns This timing information from the cathode signals would aid in pattern recognition of multiple tracks passing through the chamber volume.

### Gas Considerations

There are several basic requirements that need to be met by the chamber gas that will be used for the FDC system. These include a high drift velocity (50-60 $\mu$m/ns), low Lorentz angle ($< 10^\circ$), and for safety, a non-flammable mixture. It is important to understand that the performance

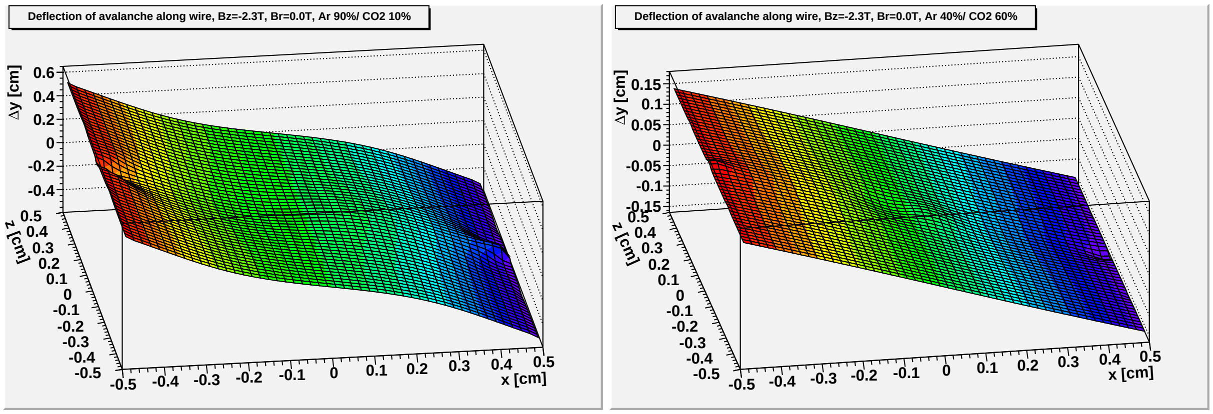

Figure 3.33: Results of GARFIELD calculations for the deflection of the avalanche position (relative to the B=0 case) as a function of the position of the ionization within the cell for two different gas mixtures: 90% Ar / 10% $CO_2$ (left) and 40%Ar / 60% $CO_2$ (right). The high voltage settings were S=+1550 V, F=-200 V, and S=+2200 V, F=-500 V, respectively.

of a cathode chamber in terms of cathode position resolution is reasonably insensitive to the exact values of the gas parameters. Here variations of the drift velocity or non-uniform drift velocities as a function of $E/p$ (i.e. electric field/pressure) are relatively unimportant. For the same reason, the cathode readout operation is immune to modest variations of temperature and pressure. Variations in gas gain on the order of 20% do not strongly affect the cathode resolution since a relative charge measurement in adjacent strips is involved.

However, the gas mixture and its control are essential for the operation of the MWDC. In order to enable accurate calibrations of the drift times, it is essential that the gas mixture is stable, which amounts to constructing a gas handling system that carefully controls the gas mixture, as well as hall-controls to fix the temperature and relative humidity as much as possible.

For the electric field configurations under consideration, increasing the percentage of argon, within a mixture of argon/$CO_2$, results in greater deflection of the avalanche position along the wire. Figure 3.33 compares the deflection along the wire as a function of the position of the ionization within a drift cell for a 90%/10% Ar/$CO_2$ mixture, and a 40%/60% mixture. We have opted for the 40% Ar/ 60% $C0_2$ mixture. At the highest magnetic field we expect to see in the chambers, the 40% Ar/ 60% $C0_2$ mixture has a maximum deflection of about one quarter of that for a 90%/10% Ar/$CO_2$ mixture. Figure 3.29 shows the field lines for two possible wire configurations (with and without field-shaping wires). The drift-to-time relationship for the 40%/60% mixture is shown in Figure 3.34. The presence of a non-zero magnetic field lengthens the minimum drift time for ionizations occurring near the field wires by a small amount relative to the B=0 case.

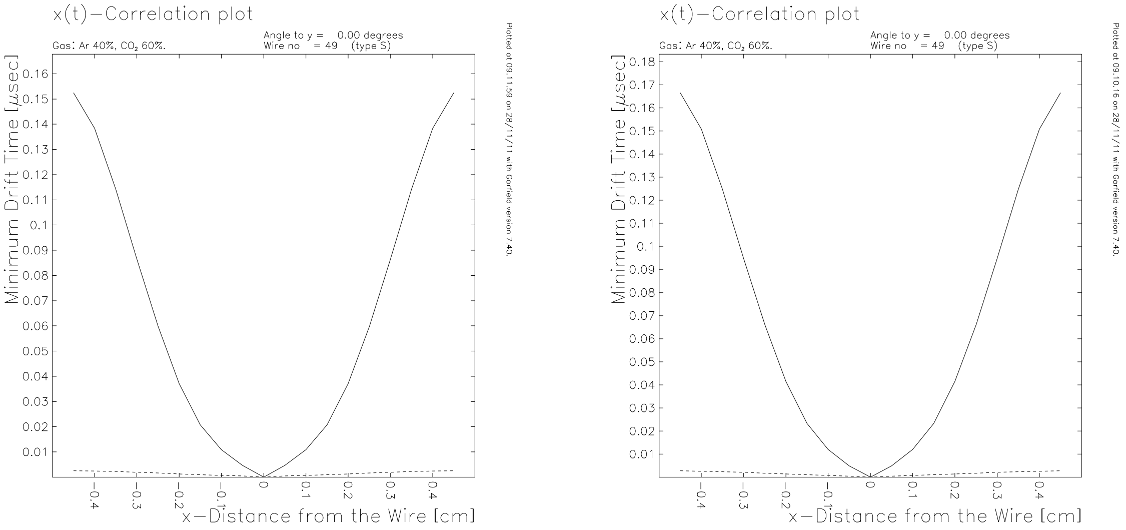

Figure 3.34: Relationship between drift time and distance for B=0 (left) and B=-2.3 T (right) from a GARFIELD calculation for an FDC cell.

## 3.7 Time of Flight

### 3.7.1 TOF Summary [43]

The main parameters and properties of the TOF are given in Tables 3.20 and 3.21. The assembly drawing for the TOF is D000000105-0000.

Table 3.20: TOF properties.

| Item | Value |
|---|---|
| Scintillator Type | Eljen EJ-200 |
| Scintillator Dimensions ($cm^3$) | |
| standard | $2.54 \times 6.0 \times 252$ |
| half-width | $2.54 \times 3.0 \times 252$ |
| half-length | $2.54 \times 6.0 \times 120$ |
| Read-Out Channels per Module | |
| standard | 2 |
| half-width | 2 |
| half-length | 1 |
| Light Guide Material | UVT PMMA |
| Light Guide Length (standard module) | approx. 30 cm |
| Wrapping Material Thickness (mils) | |
| inside: 3M ESR Daylighting Film | 2 |
| outside: Tedlar | 1 |
| Module count | |
| standard | 2×38 |
| half-width | 2×4 |
| half-length | 2×4 |
| **total** | 92 |
| Layers | 2 |
| Mean-Time Resolution (one standard module, rms) | 90-95 ps |
| PMT operating voltage | approx. 1750 V |

Table 3.21: TOF instrumentation.

| Device | Description | Quantity |
|---|---|---|
| Photomultiplier Tube | Hamamatsu H10534MOD | 176 |
| Splitter | JLab 50/50 splitter, 48 ch | 4 |
| Flash ADCs | JLab fADC250-MHz, 16 ch | 11 |
| Discriminator | JLab LE Discriminator, 16 ch | 11 |
| TDCs | CAEN 1290A TDC, 32 ch | 6 |
| HV for PMTs | CAEN A1535SN, 24 ch | 8 |

---

[43] *SVN revision ID:* tdr_summary_tof.tex 13854 2014-06-12 04:42:15Z gen

## 3.8 Start Counter

### 3.8.1 Start Counter Summary [44]

The main parameters and properties of the ST are given in Tables 3.22 and 3.23. The drawings for the ST can be found at D000000101-0001.

Table 3.22: ST properties.

| Item | Value |
|---|---|
| number of counters | 30 |
| scintillator material | Eljen EJ-200 |
| scintillator thickness | 3 mm |
| length of barrel straight section | 39.5 cm |
| length of nose straight section | 16.2 cm |
| radius of curvature of bend section | 12.0 cm |
| total angle of bend | 18.5 degrees |
| inner width of the counter | 16.29 mm |
| aluminum wrapping | 16.5 $\mu$m |
| distance from Z-axis to the counter | 77.5 mm |
| inner Rohacell shell ID/OD | 133.3 mm / 152.1 mm |
| Time resolution, $\sigma$ | 0.35 ns |
| Thickness including structure (rad.len.) | 1.2% |

Table 3.23: ST read-out instrumentation

| Item | Description | Quantity |
|---|---|---|
| photodetector | Hamamatsu MPPC, S10931-50P | 4×30 |
| discriminator | JLab LE discriminator, 16 ch | 2 |
| TDC | JLab F1TDC V2 60 ps, 32 ch | 1 |
| Flash ADC | JLab fADC250-MHz, 16 ch | 2 |
| MPPC Bias supply | ISEG EHS 201P-F-K, 16 ch, 10mA for 4 MPPC/ch | 2 |
| LV power | MPOD MPV8008, 8 ch, 5 A/ ch | 1 |

---

[44] *SVN revision ID:* tdr_summary_st.tex 13854 2014-06-12 04:42:15Z gen

### 3.8.2 Start Counter Overview

The primary purpose of the GlueX Start Counter is to provide timing information sufficient to resolve which beam pulse a physics event is associated with. The start counter is designed to operate at tagged photon intensities of up to $10^8\,\gamma/s$ and provides a fast signal to the level–1 trigger of the experiment. Furthermore, the Start Counter detector provides excellent solid angle coverage of $\sim 90\%$ of $4\pi$ hermicity, with a high degree of segmentation for background rejection. We employ Eljen Technology EJ-200 scintillator material in the construction of the start counter. The EJ-200 has a decay time on the order of 2 ns with long attenuation length, which allows the proper identification of the 2 ns "beam buckets". The detector consists of a cylindrical array of 30 scintillators with *pointed* ends that bend towards the beamline in the downstream direction. The support structure material is kept to an absolute minimum in the active region of the detector and is made up of Rohacell and carbon fiber. Silicon PhotoMultiplier (SiPM) detectors have been selected for the readout system since such detectors are not affected by the high magnetic field produced by the GlueX superconducting solenoid magnet. Moreover, the SiPMs are placed as close as reasonably possible ($< 1$ mm) to the upstream end of each scintillator element, thereby minimizing the loss of scintillation light.

### 3.8.3 Paddle Geometry

Each individual paddle of the Start Counter is machined from a long, thin, plastic (polyvinyl toluene) EJ-200 scintillator bar that was initially manufactured by Eljen Technology to be 600 mm in length, 3 mm thick, and $20 \pm 2$ mm wide. Eljen Technology bends each scintillator around a higly polished aluminum drum by applying localized infrared heating to the bend region. The bent scintillator bars were then sent to McNeal Enterprises, a plastic fabrication company, where they were machined to the desired geometry (see figure 3.35). The paddles are designed to consist of three sections. The three sections are described here starting from the upstream end towards the downstream end. First is the straight section, which is 394.65 mm in length and runs parallel to the target chamber. Second is the bend region which consists of a $18.5^\circ$ arc of radius 120 cm downstream of the straight section. Third is the tapered region, which is downstream of the target chamber, bends towards the beamline and ends at a radial distance of 20 mm from the beamline. After the straight bar is bent to the desired geometry, the taper of the third region is created by cutting the left and right side of the downstream end at a $6^\circ$ angle. During this process the width of the top and bottom surfaces are machined to be 16.92 mm and 16.29 mm respectively. Each of the 30 paddles may be rotated $12^\circ$ with respect to the paddle that preceded it so that they form a cylindrical shape with a conical end (See figure 2). The geometry of the Start Counter increases solid angle coverage while minimizing multiple scattering. The complete assembly is designed to have a diameter of $\sim 155$ mm at the upstream end and a diameter of 40 mm at the downstream end (see figure 3.36).

### 3.8.4 Support Structure

The 30 scintillator paddles are placed atop a rigid, low-density ($\rho = 0.075\,\mathrm{g/cm^3}$) Rohacell foam support structure which envelopes the vacuum chamber. The 11 mm thick Rohacell is rigidly attached to the chassis and extends down towards the end of the paddles (see figure 3.37). In order to provide additional support during the assembly process, 3 layers of carbon fiber ($\rho = 1.523\,\mathrm{g/cm^3}$) are glued to the inner diameter of the Rohacell support structure, with each

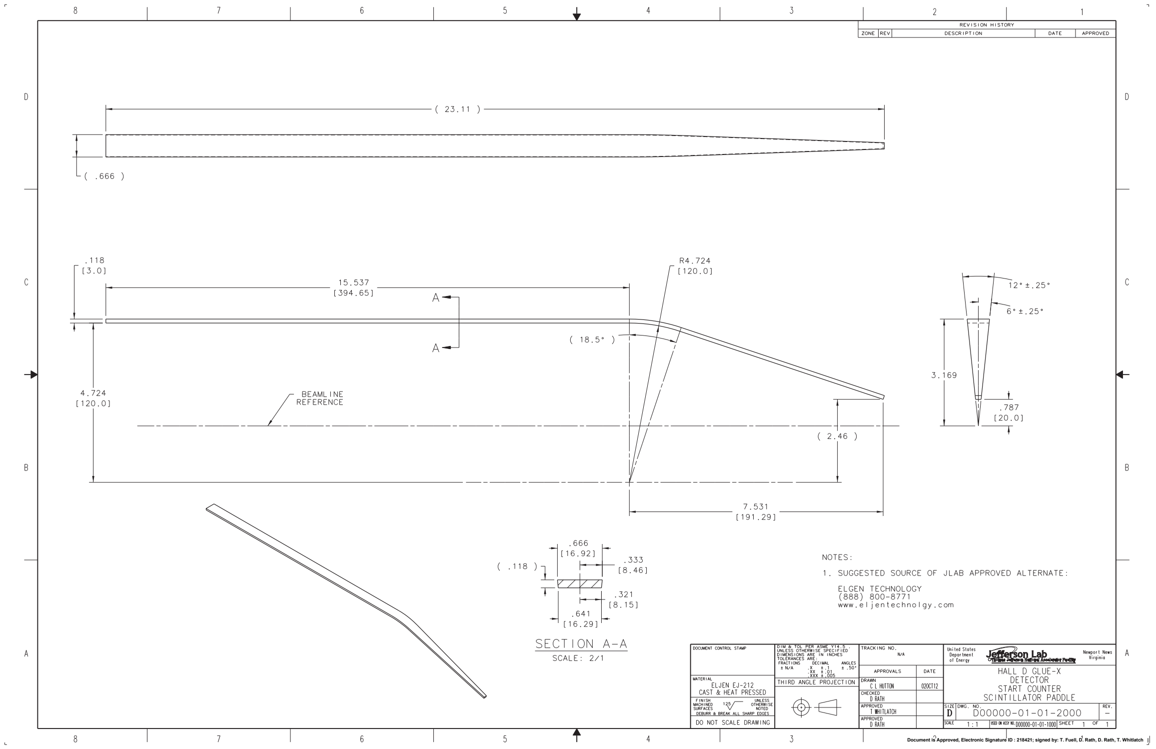

Figure 3.35: The geometry of a single Start Counter paddle.

layer having a thickness of 650 $\mu$m (see figure 3.38). The SiPM detectors are held in a fixed position while being attached to the lip of the chassis *via* two bolts. The scintillators are placed as close as possible to the SiPMs, without directly touching the active region of the SiPMs.

### SiPM Detectors & Electronics

The Start Counter (ST) has its scintillators coupled, *via* an air gap ($<1$ mm), to groups of four SiPMs set in a circular arrangement. The individual SiPMs are single-cell SiPMs (Hamamatsu MPPC, S10931-50P) with a $3 \times 3\,\mathrm{mm}^2$ active area. Four individual SiPMs, grouped together in a linear array (see figure 3.39), are arranged such that they are parallel to the end of the upstream end of the scintillator. Four SiPMs, reading out one individual paddle, are current summed prior to pre-amplification. The output of each preamp is then split, buffered for the Analog to Digital Converter (ADC) output, and amplified for the Time to Digital Converter (TDC) output. The ADC outputs are readout by way of two 16 channel flash ADCs (JLab 250 MHz Flash, fADC250), while the TDC outputs are formed through two 16 channel leading edge discriminators (JLab LE discriminators) followed by a 32 channel flash TDC (TDC JLab F1-TDC). Furthermore, each group of four SiPMs utilize a thermocouple for temperature monitoring. There are 120 SiPMs, for a total of 30 pre-amplifier channels (see figure 3.40). After many tests, it was found that there was no substantial difference between the time resolution achieved with the SiPM design and a traditional PMT. Because of studies that indicated light loss through the use of light guides coupled to PMTs, and the advantage of the mag-

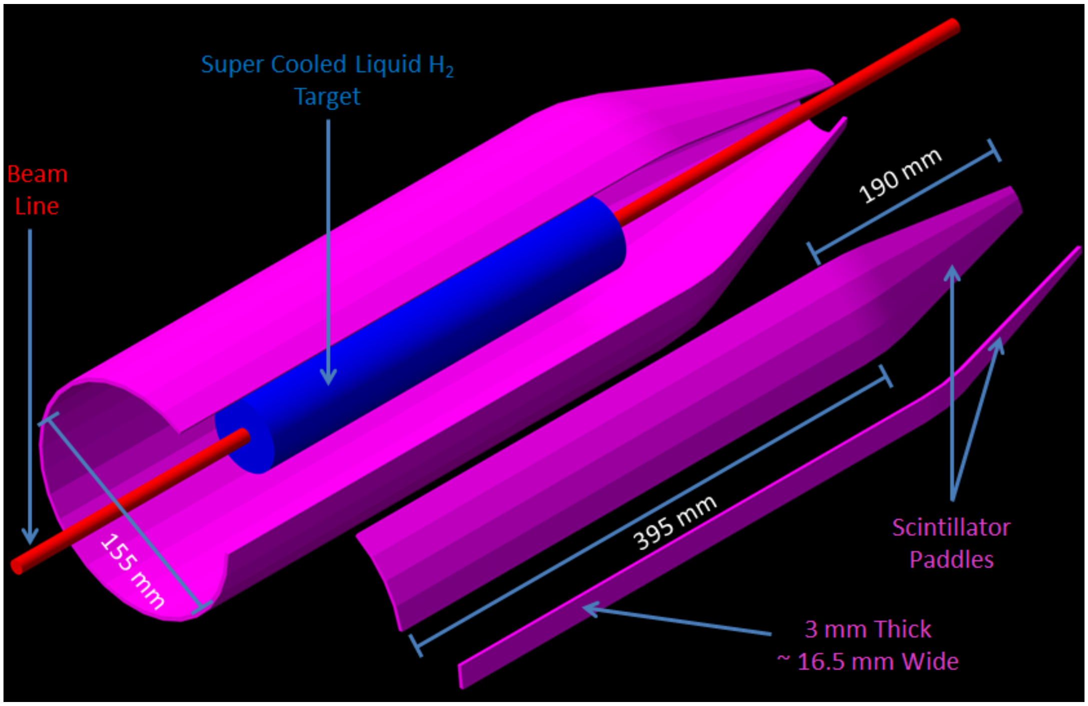

Figure 3.36: Start Counter with pieces removed revealing the target and beam line.

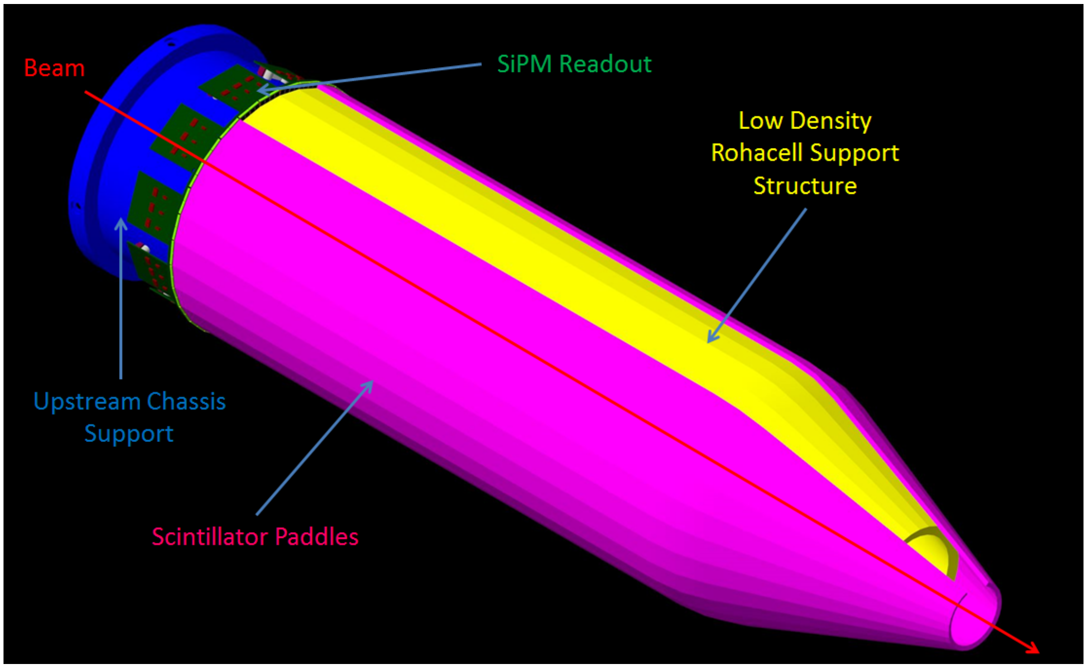

Figure 3.37: Partially assembled Start Counter.

netic field-insensitivity properties of SiPMs, it was decided that the SiPM design would be the most suitable readout system for the GlueX Start Counter. There are three components that

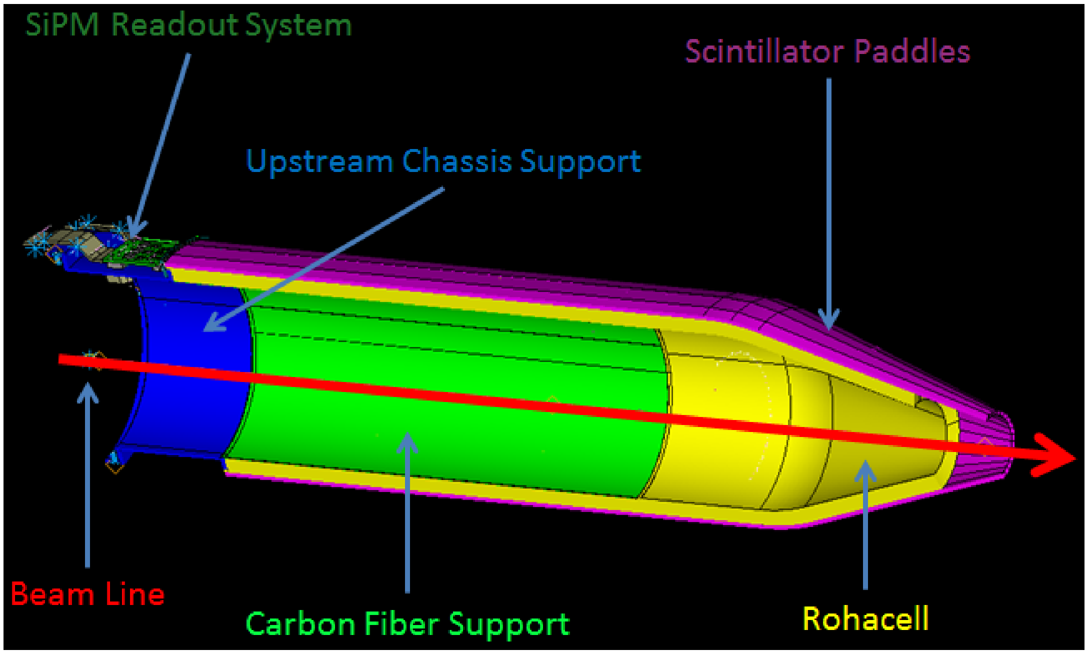

Figure 3.38: Cross sectional view of the fully constructed Start Counter.

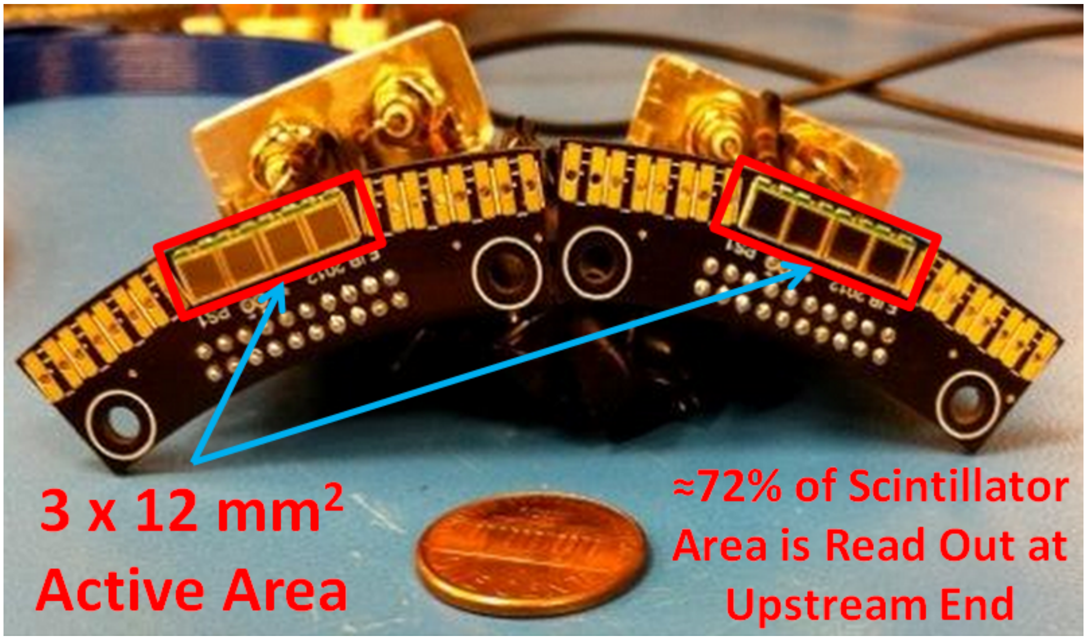

Figure 3.39: Two ST1s of the SiPM readout system placed side by side. The two holes at the bottom of ST1s PCB is the point of attachment for the SiPMs to the upstream chassis support. The SiPMs will be connected to the chassis using two pairs of nuts and bolts.

comprise the SiPM detector and readout system. The first component is the ST1 which holds 3 groups of 4 SiPMs ($3 \times 12\,\mathrm{mm}^2$ active area). The SiPMs are housed in a ceramic case and

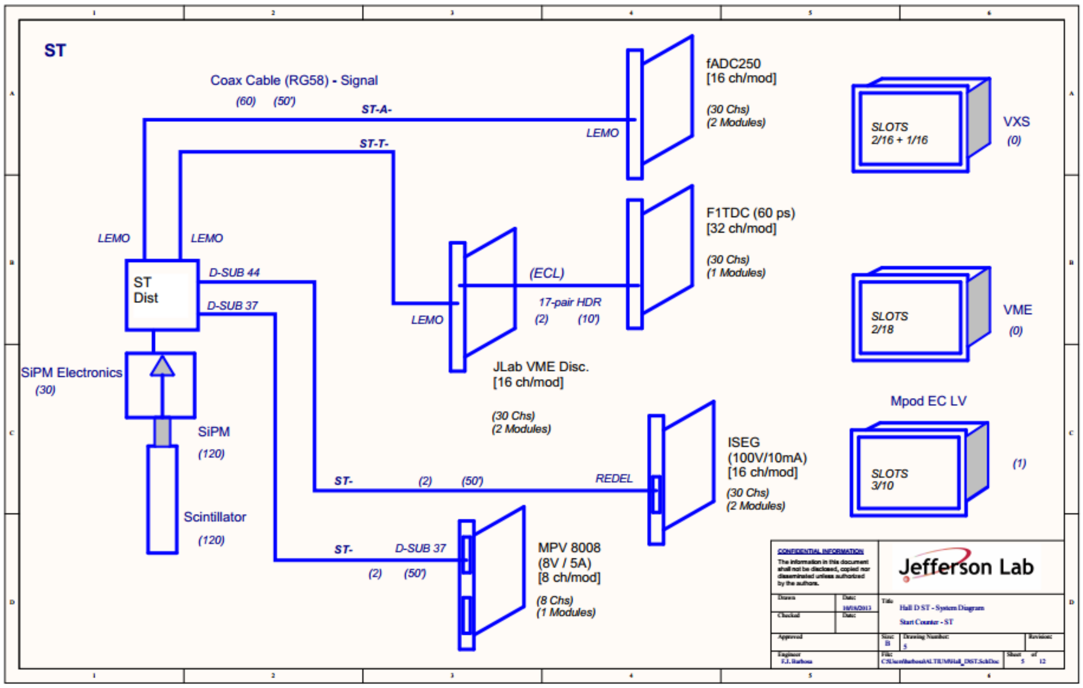

Figure 3.40: Start Counter electronics diagram.

rigidly attached to the ST1. In order to mimic the geometry of the 30 paddle design, one group (of four SiPM's) is offset by 12° relative to the central group, while another group is offset by $-12°$. Each ST1 unit collects light from three paddles individually. The ST1 implements the current sum and bias distribution per group of 4 SiPMs and has a thermocouple for temperature monitoring. The second component is the ST2, which is a Printed Circuit Board (PCB) that houses the electronics of the readout system. ST2 has 3 channels of pre-amplifiers, 3 buffers (for the ADC channels), and 3 factor-five amplifiers (for the TDC channels). Furthermore, ST2 has 3 bias distribution channels with individual temperature compensation thermistors. The ST2 is attached to the ST1 through a 90° hermaphroditic connector. The third component, the ST3, provides an interface to the power and bias supplies. It also routes the 3 ADC, and 3 TDC outputs, as well as the thermocouple output. The ST3 connects to the ST2 through a signal cable assembly (see figure 3.41). The ST3 is installed in the upstream chassis, which is upstream of the Start Counter and next to the beam pipe.

### 3.8.5 Measurements

Many data have been collected regarding long thin scintillator bars of different dimensions and materials. We have also studied the responses of various PMTs and SiPMs when coupled to scintillator bars. These data consist of measurements for both straight bars as received from Eljen Technology, and bars that have been machined to the dimmensions of the GlueX Start Counter paddles. The data showed that the optimal dimensions of the pre-machined paddles were $600 \times 3 \times (20 \pm 2)\,\mathrm{mm}^3$. Moreover, it was determined that the aforementioned SiPM and readout system would be suitable for our needs. In addition, studies determined that McNeal Enterprises provided better quality machined scintillators than other competing

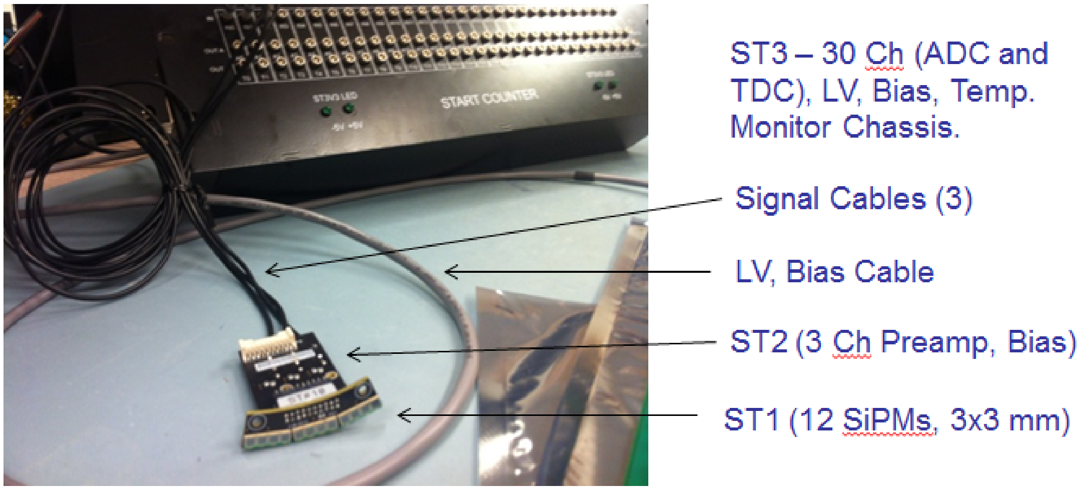

Figure 3.41: Complete Start Counter readout system.

plastics companies, *e.g.* Plastic Craft. While many tests of machined scintillators utilized the EJ-212 scintillator material, manufacturing requirements from Eljen Technology stipulated a change to the EJ-200 scintillator material. Further tests showed that there was no substantial difference between the two types of material.

### Experimental Set-up for Testing Scintillators

In order to test individual paddles, a radioactive Strontium-90 ($^{90}$Sr) source was placed at fixed distances along the path of the scintillator. $^{90}$Sr undergoes $\beta^-$ decay to $^{90}$Y (yttrium). In turn, $^{90}$Y undergoes $\beta^-$ decay to $^{90}$Zr (zirconium). The resulting decay of $^{90}$Sr provides a continuum of electron energies from $\sim 0.5$ MeV to 2.2 MeV which closely mimics the energy of minimum ionizing particles. The scintillation light is produced in the scintillator by the electrons traversing through the scintillator material. The subsequent photons were then detected using a SiPM that is coupled to the upstream end of the scintillator. A trigger PMT coupled to a scintillator was employed to provide timing information. The signals from the two detectors were then processed through various Nuclear Instrumentation Modules (NIMs) and Computer Aided Measurement And Control (CAMAC) modules. These signals were processed through a Data AcQuisition (DAQ) system. The resulting spectra were fit with Gaussian distributions with the fit parameters stored in data files. These data were then analyzed to illustrate the scintillator properties, *e.g.* $L_{attn}$, and $\sigma_{tr}$

### Results

Five scintillator bar prototypes machined to the finalized geometry were tested extensively upon arrival (06/2013) at Florida International University (FIU). The aforementioned testing procedure was implemented in an identical manner for all five of the scintillators. Figure 3.42 shows the typical behavior that is observed when measuring the various time resolutions as a function of source distance for scintillator paddles which were machined to the Start Counter geometry. The red vertical line indicates where the straight section ends and the bend/nose region begins. It is clear that the time resolution increases linearly in the straight section (0 -

39.5 cm), as one expects, and that the resolution is worst, *i.e.* least amount of light, in the bend region (39.5 - 43.3 cm), as can be seen in figures 3.42 and 3.43. An interesting phenomenon occurs in the nose region (43.3 - 59.5 cm) downstream of the bend. The time resolution begins to decrease, *i.e.* improve, as the source moves downstream of the SiPM. This effect was studied extensively *via* GEANT4 simulations, and the same result was observed. Thus, it is clear that this effect is purely a consequence of the unique geometry of the nose section. Upon comparing figures 3.42 and 3.43 it is clear that time resolution is dominated by light output. This effect is advantageous for our purposes as the majority of the charged particles produced in GlueX will have small polar angles. Based on the data and simulations, the Start Counter is able to successfully identify the electron beam buckets to within 99 % accuracy.

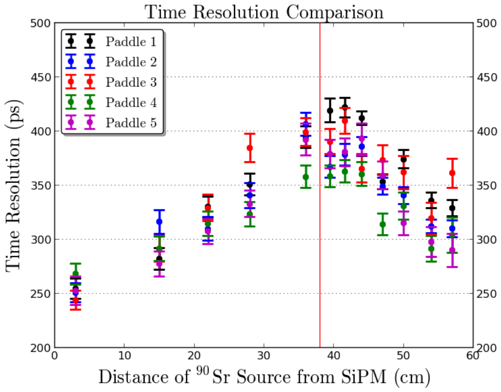

Figure 3.42: Time resolution.

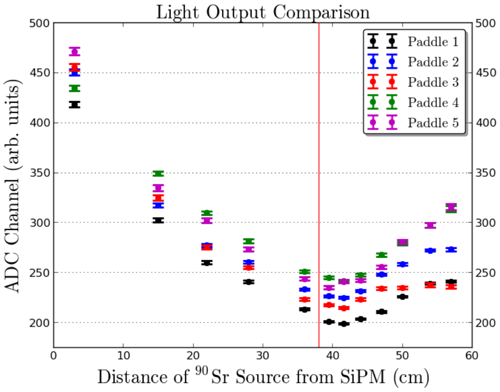

Figure 3.43: Light output.

### Wrapping of Scintillators

In order to increase the amount of light collected at the scintillator-detector interface, it is common practice to wrap plastic scintillators with reflective materials. Both 2 $\mu$m thick aluminized Mylar and 16.5 $\mu$m thick food-grade aluminum foil were extensively investigated as potential wrapping materials for individual scintillator paddles (see figure 3.44). It should be noted that the bar that was tested in this study is a prototype manufactured prior to the batch of five paddles that was discussed previously. The time resolution achieved with this bar (labelled Bar 3) was worse than what was achieved with the batch of five prototypes. To ensure light tightness in the event of microscopic holes in the reflective wrapping material, it is advantageous to wrap the scintillator and reflective material with black Tedlar film. Figure 3.45 illustrates the effect of the additional wrapping of black Tedlar Film. As can be seen in figures 3.44 and 3.45, the data indicates that wrapping the scintillators with both reflective material and black Tedlar film has no appreciable effect on the quality of the time resolution and light output when compared to wrapping only with the reflective material. While the time resolution only improved by about 10% when comparing wrapped and unwrapped scintillator paddle, the reflective materials did improve the amount of light that was collected by the SiPM. These measurements prove the advantage of utilizing reflective materials in order to increase light output. Cross talk measurements were also conducted in order to determine the effect of the reflective materials ability to reducing the amount of cross talk between two adjacent scintillator paddles. These measurements verified the advantage of wrapping scintillators in reflective material, in that the

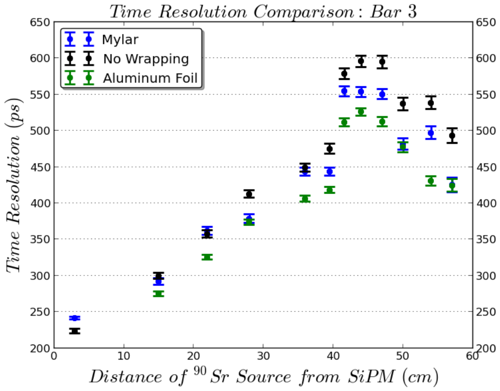

Figure 3.44: Reflective material.

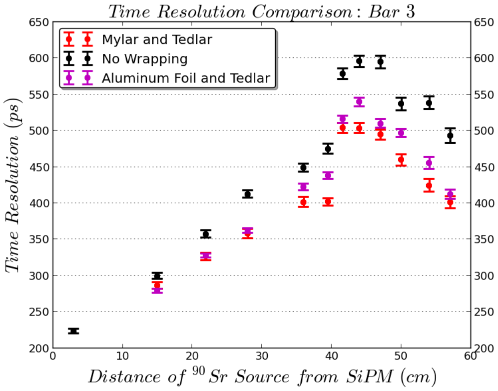

Figure 3.45: Reflective material and Tedlar.

cross talk was reduced by a factor five when compared to scintillators that were tested with no reflective material between them. However, no difference was noticed between wrapping the scintillators with Mylar and food grade aluminum foil. Coupled with previous wrapping tests, indicating no substantial difference in time resolution between the Mylar and aluminum foil, it was decided that the individual scintillator paddles would be wrapped in aluminum foil, since it is much easier to handle when wrapping scintillators.

### Deterioration

A common occurrence in scintillators is a phenomenon known as crazing. Crazing can occur in scintillators for a multitude of reasons. Some of the most common causes of crazing is that the scintillator comes into contact with chemicals other than isopropyl alcohol. Even the acids and oils from skin can diffuse into the medium of the scintillator and cause them to craze. Furthermore, machining of scintillators increases the possibility of crazing to occur. Due to the stresses and strains undergone during the machining process, it is possible for the scintillators to develop crazing over time, which may have not been visible during the initial visual inspection. After inspecting many prototypes of Start Counter paddles, it was found that some scintillators deteriorated in quality over time (see figure 3.46) and began to show visible signs of both surface and internal crazing. Numerous prototypes were made, and many of them deteriorated over time and were rendered useless. After extensive discussions with both Eljen Technology and McNeal Enterprises, the minimization of these deteriorating effects was accomplished. The most recent batch of five prototypes were monitored closely for a period of three and a half months in order to monitor for deterioration, which was proven to be a problem with previous prototypes. After close monitoring it was discovered that the scintillators were not deteriorating (see figures 3.47 and 3.48) over time. The quality of the five scintillators received in the most recent batch of prototypes from McNeal Enterprises have proven to be of the necessary quality to fulfil the needs of the GlueX Start Counter.

### Test Stand

A test stand was designed and built in order to improve the reproducibility of the measurements conducted on machined scintillator paddles (see figure 3.49). The scintillator was held in place

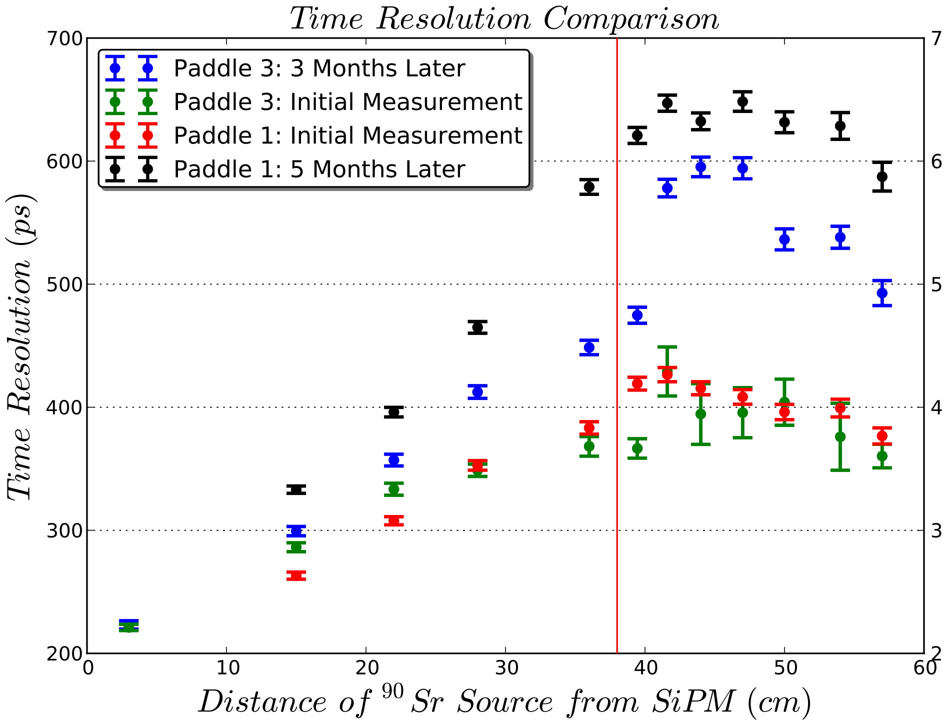

Figure 3.46: Deterioration Measurements. These data are an example of a batch of prototypes that deteriorated over time. It was discovered that after five months time, a ($\sim$ 175 ps), or 36% increase in time resolution had ensued resulting in an unacceptable quality of scintillator material.

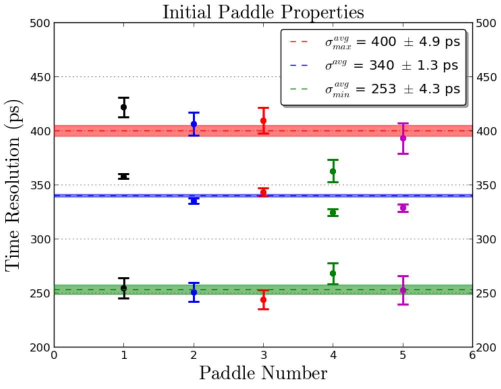

Figure 3.47: Initial Measurements.

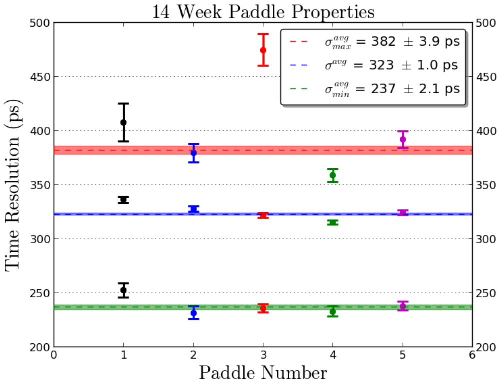

Figure 3.48: 14 Week Measurements.

by two scintillator support pieces that are rigidly attached to the frame of the test stand at fixed locations. The scintillator was held in place by spring loaded locking plungers that came into contact with a piece of protective foam which sat atop the surface of the scintillator. The frame has twelve grooves, machined at precise locations, cut out of the frame so that the trigger PMT

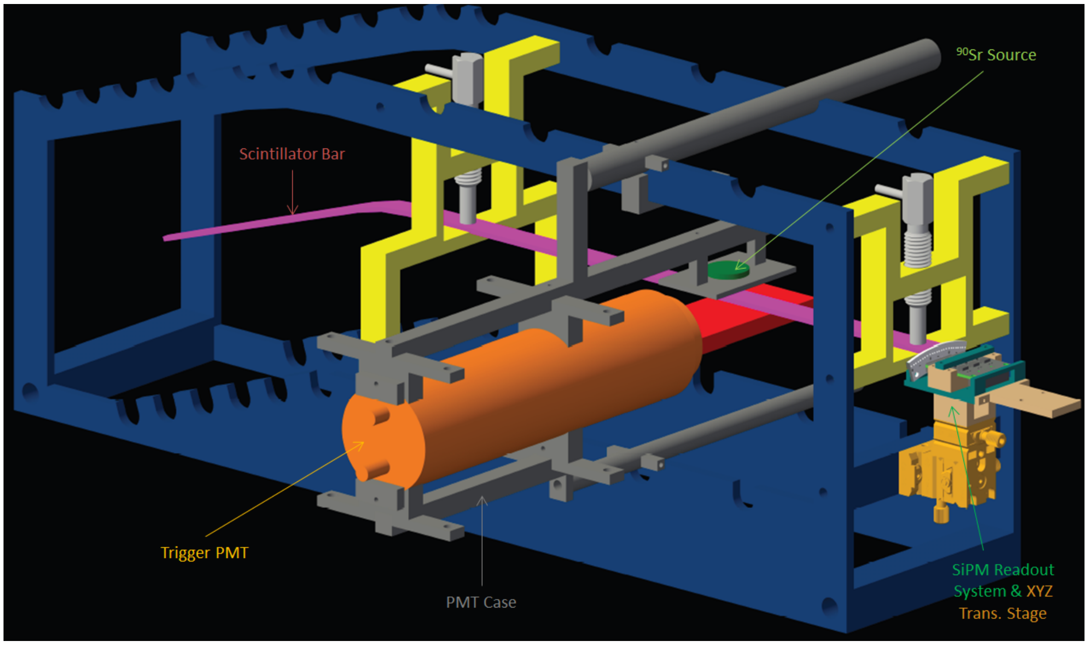

Figure 3.49: Start Counter test stand.

may be held fixed at well defined locations along the path of the scintillators. The trigger PMT was held in place by a custom case designed to mount the $^{90}$Sr source above the scintillator and the PMT below the scintillator. This design allows for the source and PMT to be moved as one unit, reducing the possibility of misalignment relative to one another, as well as aligning them relative to the scintillator. A SiPM and its readout system was placed at the upstream end of the scintillator while sitting atop a miniature dovetail XYZ translation stage. The translation stage allows for precise coupling of the SiPM relative to the upstream end of the scintillator. This design reduces any misalignment of the scintillator-SiPM interface, which is crucial for maximizing the amount of light collected by the SiPM.

### Assembly of the GlueX Start Counter

### Description & Components

The Rohacell support structure was rigidly attached to a cylindrical chassis. A locking rotation device that is able to rotate in 12° intervals was placed between two square bracket bearings that were centered on a square plate that was attached to the chassis. Ten ST1 and ST2 components were then attached at fixed locations to the lip of the chassis. All of the devices were supported by a stand. There were two identical rings each having 30 holes tapped through, separated by 12° of arc relative to the surface of the rings. Swivel screws with pads were then screwed into the holes of the rings which were placed around the Rohacell. The rings are free-floating, only supported by swivel screws, and placed at two locations along the path of the straight section of the Rohacell support structure. Two pneumatic cylinders, with steel rods that extended to a predetermined stroke length, were controlled by a pressurized air system with solenoid valves. The cylinders were oriented perpendicular to the plane of the table that the stand rested on. They were supported by a bar that was welded to a large existing metal frame. The retractable steel rod of the pneumatic cylinders were extendible so that the tip came into contact with the surface of the scintillator that was installed.

### Installation

To install a scintillator paddle, the pneumatic cylinders were retracted, as well as 2 of the 30 swivel screws that were oriented perpendicular to table. The scintillator slid down the surface of the Rohacell until it was placed as close as possible to the active area of the SiPM. The pneumatic cylinders then extended and held the scintillator in place. Fine adjustments of the scintillator were made so that the best possible alignment was achieved. The alignment of the scintillators with the SiPMs was monitored closely with specialized camera optics. Once the scintillator was in a suitable position, the swivel screws were adjusted to come into contact with the scintillator, and the pneumatic cylinders were then retracted. Upon completing the installation of one paddle, the whole device was rotated by 12° and then another paddle was installed in the exact same manner. This process was repeated until all 30 paddles had been successfully installed. In order to keep all of the scintillators firmly in place in the absence of the rings and plungers, wrapping material was installed. Once the assembly was successfully completed, the GlueX Start Counter underwent extensive testing and calibration.

## 3.9 Readout Electronics

### 3.9.1 Electronics [45]

The main parameters and properties of the electronics are given in Table 3.24.

Table 3.24: Electronics channel counts.

| Item | Description | Quantity |
|---|---|---:|
| GlueX ASIC GASS-2 | Drift chamber preamp 8ch/chip | 2034 |
| Preamp Card FDC wires | 3 ASICs GASS-2, 24 ch, discriminated output | 96 (110) |
| Preamp Card FDC strips | 3 ASICs GASS-2, 24 ch, analog output | 432 (475) |
| Preamp Card CDC wires | 3 ASICs GASS-2, 24 ch, analog output | 149 (165) |
| FANIO (for CAEN 1290) | Clock, synch, trigger signals fan in-out | 1 |
| DISC Discriminator | Leading-edge JLab discriminator, 16 ch | 109 |
| fADC125 V2 | Sampling Flash 125 MHz, 12-bit, 72 ch | 194 |
| fADC250 V2 | Sampling Flash 250 MHz, 12-bit, 16 ch | 324 |
| F1TDC V2 | Pipeline TDC, 57 ps, ECL, 32 ch | 50 |
| F1TDC V3 | Pipeline TDC, 97 ps, LVDS, 48 ch | 48 |
| CAEN VX 1290 | Pipeline TDC, 25 ps, 32 ch | 6 |
| VME64x Crate | 8 (DISC) and 3 (Controls) | 11 |
| VXS Crate | 51 DAQ and 2 Trig | 53 |
| VME Crate controller | Readout Controller (ROC) | 64 |
| TI | Trigger Interface | 52 (56) |
| SD | Signal Distribution | 52 (56) |
| CTP | Crate Trigger Processor | 26 |
| SSP | Sub-system Processor | 8 |
| GTP | Global Trigger Processor | 1 |
| TS | Trigger Supervisor | 1 (2) |
| TD | Trigger Distribution | 9 |
| LV MPV8008 | MPOD 8V, 8 ch, 5A/ch | 24 |
| LV MPV8030 | MPOD 30V, 8 ch, 2.5 A/ch | 1 |
| LV ISEG EHS 201P-F-K | MPOD 100V, 16 ch, 10 mA/ch | 31 |
| LV Chassis | MPOD Chassis / Mini (TAGM) | 7/1 |
| HV A1550P | CAEN +5kV, 1mA, 24 ch | 10 |
| HV A1550N | CAEN −5kV, 1mA, 24 ch | 4 |
| HV A1535SN | CAEN −3.5kV, 3mA, 24 ch | 19 |
| HV Chassis | CAEN HV chassis | 6 |
| Cabling | NEC 2011, NFPA 70, UL CL2 or better | |
| Racks | Hammond C4F247736 24”×36”×44”U w/d/h | 47 |
| | Low racks in the tagger hall | 8 |
| Grounding: Segregated clean and utility grounds separately bonded to hall floor grounding grid | | |
| EMI | FCC Part 15, CISPR 22, Class B | |

---

[45] *SVN revision ID:* tdr_summary_electr.tex 13854 2014-06-12 04:42:15Z gen

### 3.9.2 Overview

The GlueX electronics implements signal conditioning, digitization, processing and read out of the detector signals for level 1 trigger rates of up to 200 kHz without incurring deadtime. A fully pipelined architecture is implemented where the digitized information is stored for several $\mu$s while the level 1 trigger is formed. Multiple events are buffered within the digitizer modules and read out while new events are acquired.

A summary of the characteristics of the GlueX detector subsystems from an electronics viewpoint is shown in figure 3.50.

A fully integrated development was implemented to instrument the various particle detectors in a systematic and common infrastructure. The integrated development considered grounding, electro-magnetic interference (EMI), cabling, power distribution, detector electronics, digitizing modules, packaging, installation and servicing. Guiding the system architecture in such a manner has considerable advantages in minimizing the number of design variants while taking full advantage of the expertise available within the collaboration and JLab, addressing electrical safety code requirements, improving performance, reliability and servicing of the installed instrumentation.

There are three classes of sensors in use with GlueX detectors: PMTs, SiPMs and drift chambers. PMTs are typically powered from commercially available HV power supplies and readout via coaxial cables. The SiPMs (Silicon Photo-Multipliers) are optical sensors which have been developed recently, produced in large quantities for GlueX by Hamamatsu, require custom designed frontend electronics and bias supplies of less than 80 V. The GlueX drift chambers are instrumented with ASICs and preamp cards specifically designed for the CDC and FDC.

#### ASIC and Preamps for the Drift Chambers

An Application Specific Integrated Circuit (ASIC) was developed for application in both the FDC and CDC drift chambers. The ASIC was necessitated by the geometrical constraints presented by the packaging of the FDC with a limited space of 5 mm between the detector layers and within the solenoid volume.

The ASIC (GASS-II) is configurable for the specific application and includes a charge preamplifier, shaping with tail cancellation, switch, driver and discriminator. Configuration is effected at the PCB level during assembly to conform to the FDC and CDC requirements. Figure 3.51 shows the block diagram of the fully differential GASS-II. The GASS-II is characterized by CR-RC$^2$ with the following behavioral Laplace transfer function:

$$\mathcal{L} = \frac{R1}{1 + sR1C1}\left(\frac{R3}{R2}\right)\frac{\frac{1}{sR2C2}}{1 + sR3C2}\frac{1}{(1 + sR4C3)^2},$$

where R1=9.5 k$\Omega$, R2=100 k$\Omega$, R3=R4=16 k$\Omega$, C1=0.65 pF and C2=C3=0.3 pF. This function, together with the transfer functions of the signal cable and of the fADC125 input shaping circuitry fully describe the transfer function of the drift chambers readout chain and can be employed to devise algorithms for data processing. The GASS-II equivalent noise charge is less than 5,000 electrons at 50 pF of detector capacitance with a characteristic slope of 45 e$^-$/ pF. The output level, when in discriminator mode, is LVDS and readily interfaces to the F1TDCV3. Typical characteristics of the GASS-II are:

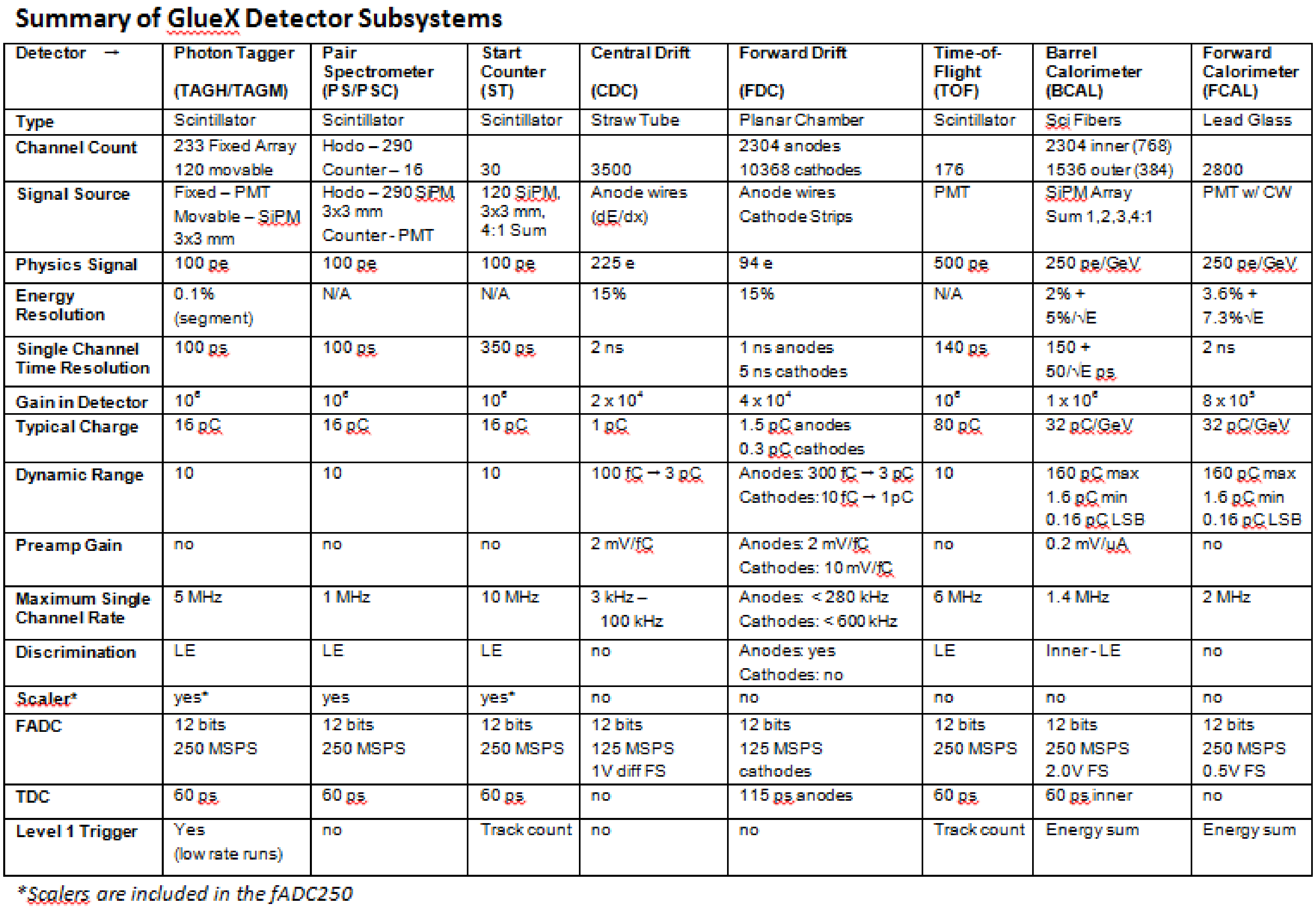

**Summary of GlueX Detector Subsystems**

| Detector → | Photon Tagger (TAGH/TAGM) | Pair Spectrometer (PS/PSC) | Start Counter (ST) | Central Drift (CDC) | Forward Drift (FDC) | Time-of-Flight (TOF) | Barrel Calorimeter (BCAL) | Forward Calorimeter (FCAL) |
|---|---|---|---|---|---|---|---|---|
| **Type** | Scintillator | Scintillator | Scintillator | Straw Tube | Planar Chamber | Scintillator | Sci Fibers | Lead Glass |
| **Channel Count** | 233 Fixed Array<br>120 movable | Hodo – 290<br>Counter – 16 | 30 | 3500 | 2304 anodes<br>10368 cathodes | 176 | 2304 inner (768)<br>1536 outer (384) | 2800 |
| **Signal Source** | Fixed – PMT<br>Movable – SiPM 3x3 mm | Hodo – 290 SiPM 3x3 mm<br>Counter - PMT | 120 SiPM, 3x3 mm, 4:1 Sum | Anode wires (dE/dx) | Anode wires<br>Cathode Strips | PMT | SiPM Array<br>Sum 1,2,3,4:1 | PMT w/ CW |
| **Physics Signal** | 100 pe | 100 pe | 100 pe | 225 e | 94 e | 500 pe | 250 pe/GeV | 250 pe/GeV |
| **Energy Resolution** | 0.1%<br>(segment) | N/A | N/A | 15% | 15% | N/A | 2% +<br>5%/√E | 3.6% +<br>7.3%√E |
| **Single Channel Time Resolution** | 100 ps | 100 ps | 350 ps | 2 ns | 1 ns anodes<br>5 ns cathodes | 140 ps | 150 +<br>50/√E ps | 2 ns |
| **Gain in Detector** | $10^6$ | $10^6$ | $10^6$ | $2 \times 10^4$ | $4 \times 10^4$ | $10^6$ | $1 \times 10^6$ | $8 \times 10^3$ |
| **Typical Charge** | 16 pC | 16 pC | 16 pC | 1 pC | 1.5 pC anodes<br>0.3 pC cathodes | 80 pC | 32 pC/GeV | 32 pC/GeV |
| **Dynamic Range** | 10 | 10 | 10 | 100 fC → 3 pC | Anodes: 300 fC → 3 pC<br>Cathodes: 10 fC → 1pC | 10 | 160 pC max<br>1.6 pC min<br>0.16 pC LSB | 160 pC max<br>1.6 pC min<br>0.16 pC LSB |
| **Preamp Gain** | no | no | no | 2 mV/fC | Anodes: 2 mV/fC<br>Cathodes: 10 mV/fC | no | 0.2 mV/uA | no |
| **Maximum Single Channel Rate** | 5 MHz | 1 MHz | 10 MHz | 3 kHz – 100 kHz | Anodes: < 280 kHz<br>Cathodes: < 600 kHz | 6 MHz | 1.4 MHz | 2 MHz |
| **Discrimination** | LE | LE | LE | no | Anodes: yes<br>Cathodes: no | LE | Inner - LE | no |
| **Scaler*** | yes* | yes | yes* | no | no | no | no | no |
| **FADC** | 12 bits<br>250 MSPS | 12 bits<br>250 MSPS | 12 bits<br>250 MSPS | 12 bits<br>125 MSPS<br>1V diff FS | 12 bits<br>125 MSPS<br>cathodes | 12 bits<br>250 MSPS | 12 bits<br>250 MSPS<br>2.0V FS | 12 bits<br>250 MSPS<br>0.5V FS |
| **TDC** | 60 ps | 60 ps | 60 ps | no | 115 ps anodes | 60 ps | 60 ps inner | no |
| **Level 1 Trigger** | Yes<br>(low rate runs) | no | Track count | no | no | Track count | Energy sum | Energy sum |

**Scalers are included in the fADC250*

Figure 3.50: Summary of GlueX detector subsystems

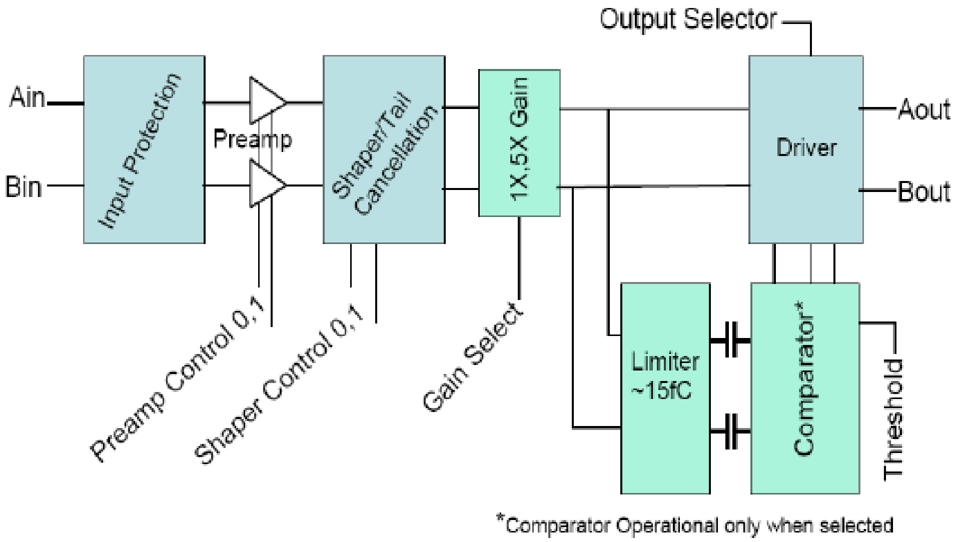

Figure 3.51: ASIC GASS-II block diagram

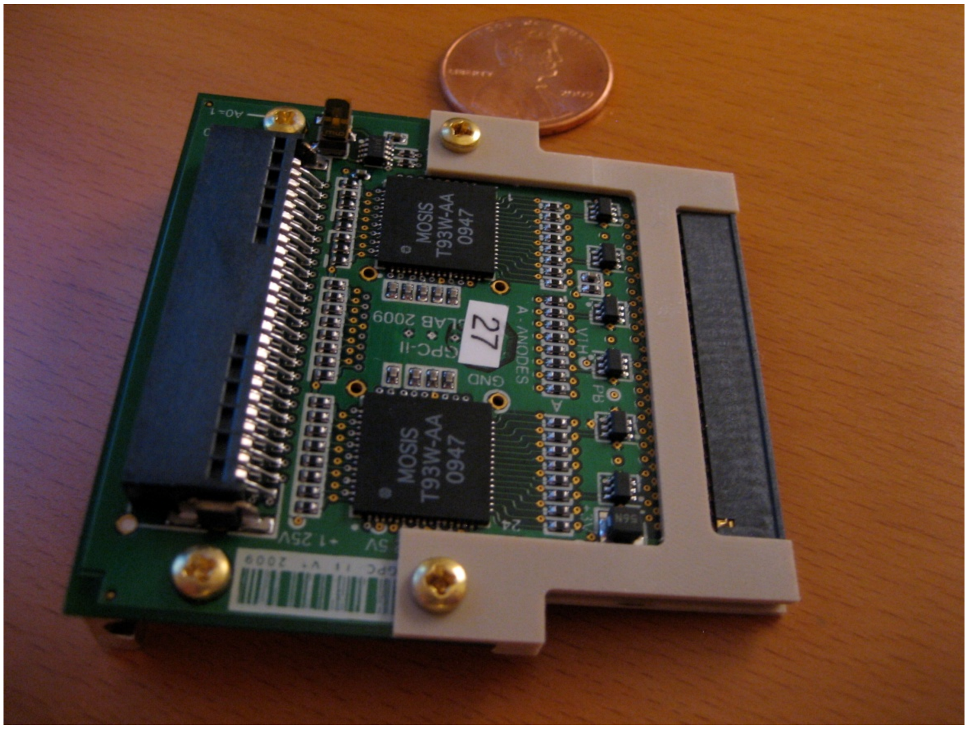

Figure 3.52: The GPC-II preamplifier card for the CDC and the FDC

| ASIC ID | GASS-II |
|---|---|
| Number of channels | 8, differential with input protection |
| Type | Charge amplifier |
| Configuration | Gain, peaking time, discriminator |
| Peaking time | 11ns |
| Discrimination | 20ns pulse width, common threshold input |
| Noise (ENC) | 5,000 $e^-$ at 50pF |
| Package | 64 pins, 10mm X 10mm, QFN, ipac |
| Process | 0.25m, CMOS |
| Manufacturer | MOSIS |
| Die ID, size | V13L-AA design 80773, 7.04mm X 4.8mm |

Table 3.25: Typical characteristics of the GASS-II

A 24-channel preamp card (GPC-II) was developed to serve both the FDC and the CDC so that only a single ASIC and a single preamp card design were needed. This common infrastructure extends to supporting systems such as signal cabling, low voltage supplies, high voltage supplies, distribution, as well as controls. The bottom side of the GPC-II has one additional ASIC along with configuration resistors, which are placed according to the requirements of the CDC and the FDC. Polarity configuration is also set via resistors during assembly, a benefit of the differential topology. The configuration of the 24-Ch GPC-II is as follows:

| Application | Assembly Variant | Input Polarity | Gain (mV/fC) | Dynamic Range (fC) | Peaking Time (ns) | Power (mW/Ch) |
|---|---|---|---|---|---|---|
| CDC Anode | Type I | Negative | 0.57 | 380 | 12.0 | 49 |
| FDC Cathode | Type II | Positive | 2.6 | 130 | 13.8 | 49 |
| FDC Anode | Type III | Negative | 0.77; LVDS Discriminator | 260 | 9.6 | 49 |

Table 3.26: Configuration of the 24-channel GPC-II

To meet the FDC layer spacing requirements, the preamp card is less than 5 mm thick in its installed position. Due to the limited space, cooling of the preamps on the FDC is effected via heat spreader brackets attached to cooling loop pipes and with Fluorinert liquid flow. Due to less restrictive geometrical conditions, cooling by way of forced convection is implemented on the CDC.

Cabling for the 24 differential output signals consists of 0.025 24 pitch 50 wire, twisted and shielded cable, low profile and high density 50-pin ERNI connectors for the preamp side and robust 50-pin 3M shielded connectors for the readout side. The 25th pair is used to capacitively pulse all the 24 channels from signal pulsers designed into the fADC125s and the F1TDCV3s.

Due to geometrical constraints, the preamp cards are plugged into PCBs that are laminated into the FDC. The CDC benefits from the same design as the FDC and employs an interposer board, High Voltage Board (HVB), which also provides high voltage distribution to 24 straw tubes from a single high voltage supply channel. Straw tube connections to the HVB, which are AC-coupled, are effected via coaxial cables with their shields connected to the high voltage input and decoupled to ground for good noise performance. Due to the high input charge from the CDC, divide-by-2 charge division is implemented at the input of every preamp channel. The HVB is shown in fig. 3.53.

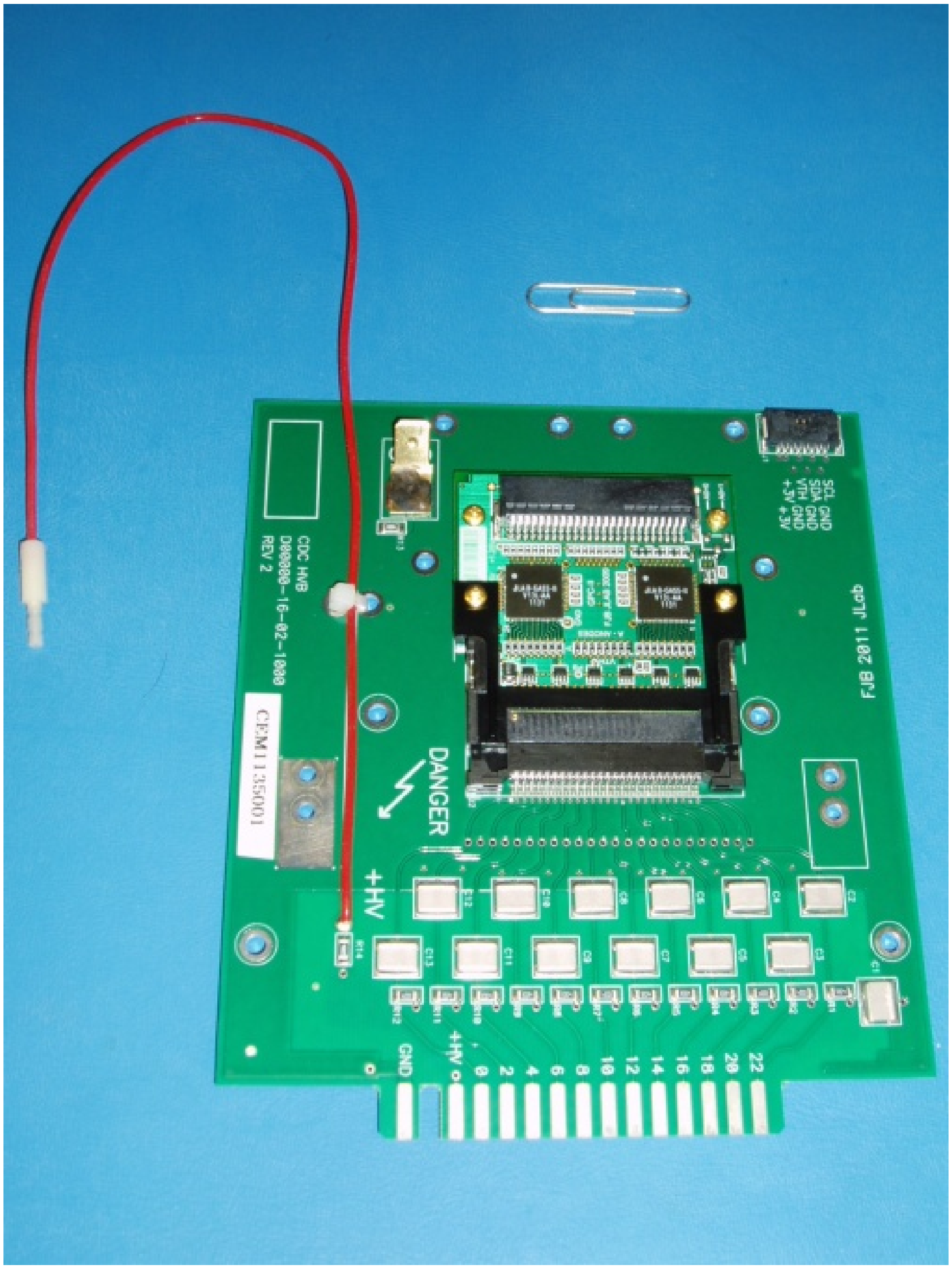

Figure 3.53: The CDC HVB with a preamp card installed

### SiPM Readout

SiPMs are semiconductor optical sensors which replace PMTs in applications requiring insensitivity to magnetic fields. The BCAL, PS, ST and TAGM detectors employ SiPMs in various

| Application | Assembly Variant | Input Polarity | Effective Gain (mV/fC) | Effective Dynamic Range (fC) | Peaking Time (ns) | Power (mW/Ch) |
|---|---|---|---|---|---|---|
| CDC Anode | Type I with HVB | Negative | 0.30 | 740 | 12.0 | 49 |

Table 3.27: Configuration of HVB

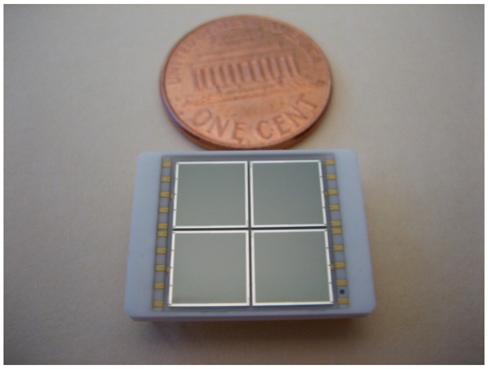

Figure 3.54: BCAL 4x4 SiPM array front view

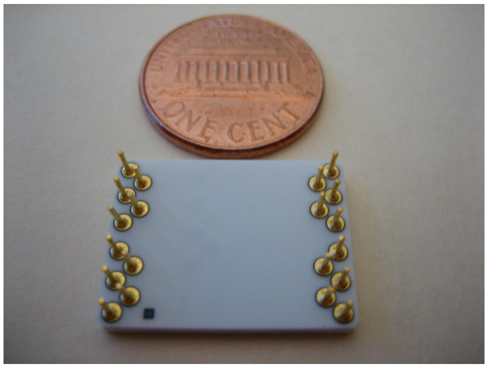

Figure 3.55: BCAL 4x4 SiPM array rear view

configurations, all manufactured by Hamamatsu with 3 mm x 3 mm cells and 50 $\mu$m pixels.

The BCAL SiPM ceramic package was developed jointly with Kyocera to address the thermal and geometrical requirements of the BCAL modules, which require good temperature regulation at 5°C for lower sensor noise. The rear of the package allows for contact to a cooling plate. In order to maintain the SiPM gain constant a two-stage regulation is implemented: liquid cooling flows through a pipe embedded into the cooling plate to effect cooling of the SiPMs in a BCAL module; a thermistor-resistor network, matched to the SiPM temperature characteristic but with a positive +56mV/C slope, compensates each SiPM bias voltage against further temperature non-uniformities. The 4x4 SiPM array is shown in fig. 3.54 (front) and fig. 3.55 (rear). The PS, ST and TAGM employ the same single cell SiPM S10931 from Hamamatsu.

Fig **??** is a diagram of the cooling and readout implementation for the BCAL. Thermal mats are employed to effect low thermal impedance connections between the SiPM and the cooling plate and the readout electronics and the heat spreader, which eventually dissipates excess heat to ambient. The 23U24 PCB holds the SiPM, implements a 16 cell sum and provides bias distribution, with miniature coax cables providing electrical connections. The light guide from the BCAL detector couples light to the SiPMs through a 1 mm gap and the module is permeated with nitrogen to prevent condensation.

The BCAL, PS and ST have bias temperature compensation, where several sensors are biased from a single supply, and share similar readout architectures. The TAGM, however, includes temperature compensation through direct bias setting to each SiPM through DACs. Fig. 3.59 shows a diagram of the SiPM readout architecture: the thermistor, R1 and R2 are chosen to have a +56mV/C slope and, therefore, maintain the SiPM gain (invariant to temperature changes) and provide the required SiPM bias. The anodes of the sensors (pixels or cells) are connected via a shaping network to the transimpedance preamps, which are referenced to ground potential. The shaping network, which is unique to each of the BCAL, PS and ST

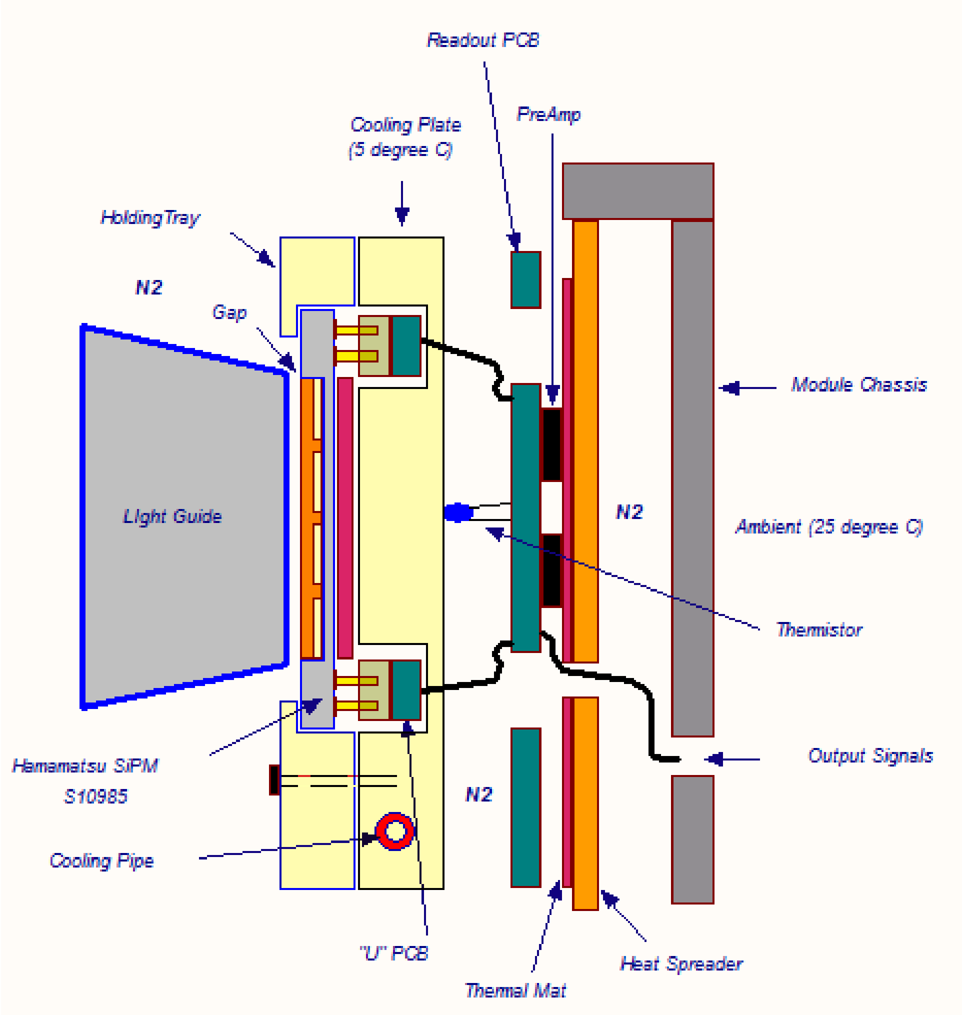

Figure 3.56: Diagram of cooling and readout implementation on the BCAL

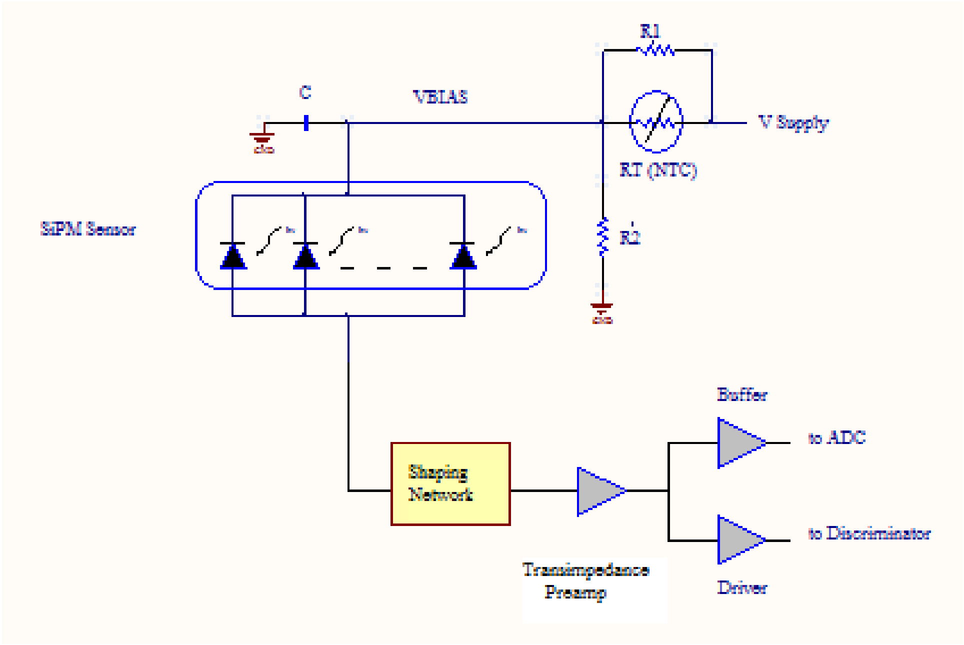

Figure 3.57: The SiPM readout architecture

detectors, optimizes the signal response for the characteristically large SiPM capacitance. The buffer and driver outputs are then coupled to RG-58 type 50 Ω coaxial cables. In the case of the PS, which does not require a TDC, the high gain driver is not implemented. The gain specifications, not including cable losses, are as follows:

| Detector | SiPM Cells per Channel | Transimpedance Gains (mV/A) | Gains wrt 50Ohm (V/V) |
|---|---|---|---|
| BCAL | 16, 32, 48, 64 | 0.081, 0.405 | 1.6, 8.1 |
| PS | 1 | 0.987 | 19.7 |
| ST | 1 | 0.685, 6.85 | 13.7, 137 |

Table 3.28: Gain specifications

SiPMs share directly controlled bias supplies channels as follows:

| Detector | SiPM Cells per Supply Channel |
|---|---|
| BCAL | 160 |
| PS | 5 |
| ST | 4 |
| TAGM | 1 |

Table 3.29: Shared SiPM bias supplies

### Readout Modules

Readout modules were developed within a fully pipelined framework, take full advantage of the VME standard and associated infrastructure, and are widely used at Jlab. A large, fully pipelined, synchronized data acquisition system benefits from a compact and robust distribution of high-speed timing signals. This high-speed distribution is made possible by the use of newly developed extension to the VME64x standard (ANSI/VITA 1.5), which resulted in the VXS standard (ANSI/VITA 41.0). The VXS standard allows for distribution of serial data through the backplane PCB between readout modules located on payload slots, and processing or distribution modules located on switch slots. VXS is backward compatible with VME64x and allows VME modules to be installed on the VXS payload slots. Fig. 3.58 shows the JLab VXS crate. The black connectors seen on the backplane are part of the newly developed VXS with the two centrally located slots (switch slots) allowing for serial communications to each of the other slots in the crate for a total of 21 slots.

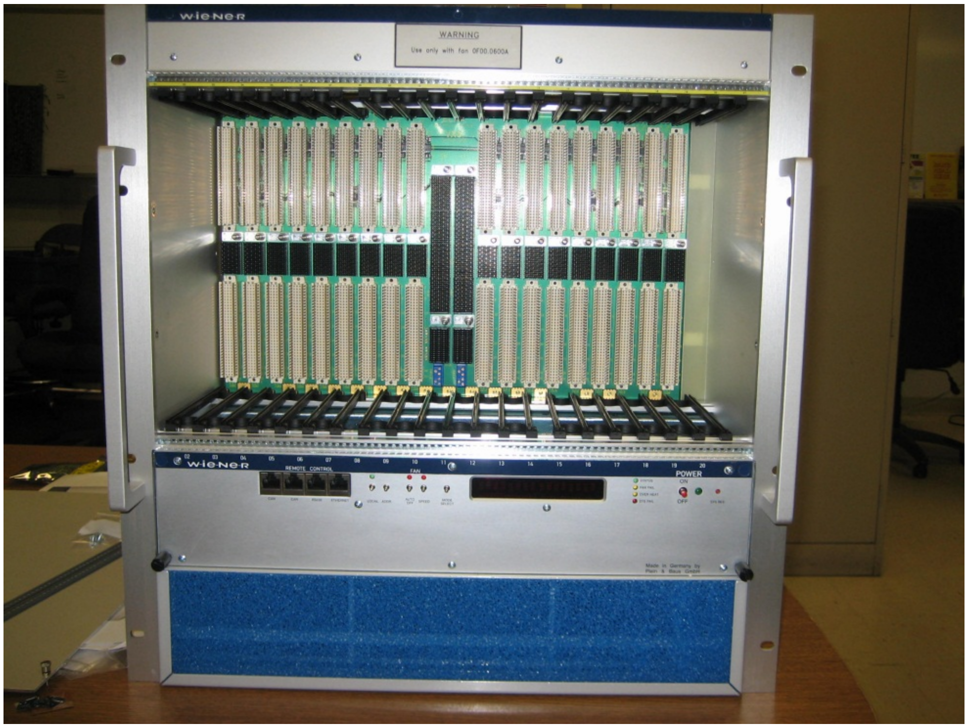

Figure 3.58: The JLab VXS crate

Differential pairings enable high-speed communication and signaling between each slot's VXS connector (P0) and the connectors on the two centrally located switch slots. All of our VXS-compliant readout modules use the differential pairings for clock distribution and synchronization. The fADC250 further utilizes the differential pairings from all the installed modules in a crate to enable collection of trigger data, and subsequent processing and trigger forming.

The VXS crate is manufactured by Wiener, occupies 11 U of rack space and accepts modules with a 6 U form factor. The high-power, low noise, plug-in power supplies are easily serviceable from the rear of the unit. The fan unit has local switches, carries three high-speed fans capable of reaching 6,000 rpm, includes controls and monitoring via Ethernet, and is easily serviceable through the front of the unit. A filter and plenum at the bottom of the unit provide for front filtered air intake, cooling of the readout modules, with the air exiting at the top and rear of the unit. The power supply unit contains its own thermal management.

Five readout modules are used in Hall D: fADC250, fADC125, F1TDCV2, F1TDCV3 and Discriminator. The functionality of these readout modules will be briefly described below. Other modules, which are widely used as part of the trigger and the signal distribution, such as the TI/TD, the SD and the CTP, will be described under the trigger section.

### fADC250

The fADC250 is a 12-bit flash Analog-to-Digital Converter, 6U VXS-compliant module primarily used with detectors that participate in the trigger formation. It employs ADC chips with pipeline architectures for high sample rates at reduced power consumption. The Analog Devices AD9230 contains a rich feature set that includes advanced test vector generation and forms the core of the fADC250. The backend of the module is enhanced with the use of Xilinx XC5VLX110 and XC5VFX70 FPGAs which, by virtue of their vast resources, allows for tailoring of the module functionality through firmware updates via VME. Fig. 3.59 shows the architecture of the fADC250.

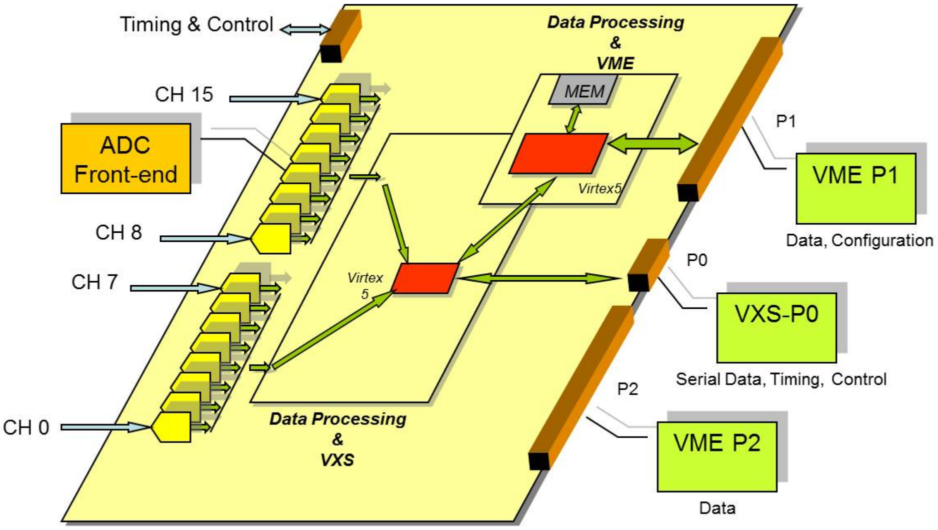

Figure 3.59: The fADC250 architecture

Each of the 16 inputs is DC-coupled through a settable attenuator, via jumper, which allows for operation with bipolar signals at full-scale ranges of 0.5V, 1.0V and 2.0V, while maintaining 50 Ω impedance. The input circuitry is fully differential with individually programmable DACs for setting the offsets and signal conditioning, and is implemented with anti-aliasing filters. Process variations are handled by an active common-mode correction bias derived from the ADC chip.

The first FPGA handles data processing duties, including the trigger sums with user-defined thresholds. The second FPGA handles VME communications through the standard VME P1 and P2 connectors, and VXS signal handling through the P0 connector, which includes clock and synchronization signals and trigger data with the two-switch slots. A JTAG port is available for various testing and configuration protocols.

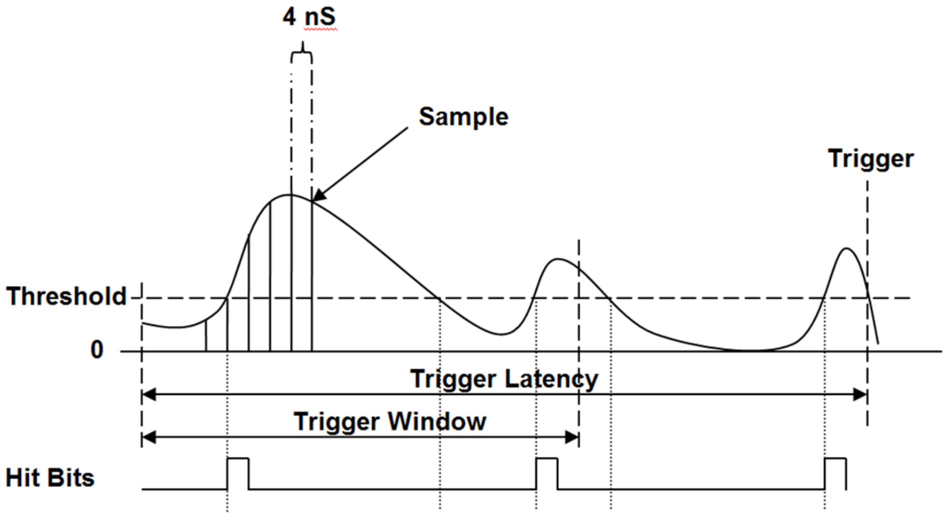

Figure 5.12: Sampling and triggering on the fADC250

Figure 3.60: Sampling and triggering on the fADC250

The sampling, data readout and trigger formation characteristics of the fADC250 are illustrated in fig. 3.60. Data is sampled at 250MHz with a distributed low jitter, less than 15 ps, clock. Signals present at the input of a channel are sampled every 4 ns and stored. This data can be readout via VME or it can be further processed to select hits or energy sums for inputs to the trigger at the 4 ns sampling interval. Hit bits from the 16 channels in a fADC250 are asserted for samples that exceed a programmed threshold. For the case of triggers based on energy sums, the samples from each of the 16 channels are summed together, resulting in a 16-bit word. The choice of data processing, hit bit or energy sum depends on the type of detector.

Once a trigger signal is formed by the global trigger system and distributed back to the fADC250 modules, the data within a selected trigger window is readout through VME. The window is selected relative to a programmable look-back delay specified by the trigger latency. The trigger latency and trigger window quantities are chosen based on the characteristics of the detectors and the various delays and will be determined empirically with great accuracy. The Triggers are also pipelined.

The data to be readout is available through VME under control of the read-out controller (ROC) as raw data from sampling at 250 MSPS, as raw data of N samples in the vicinity of a pulse, or as the sum of N samples in the vicinity of a pulse. The number of samples, N, is programmable by the user. The time information, based on the sampling rate, is obtained by looking for samples forming a rising edge of a pulse and a linear interpolation algorithm provides an estimate of the time the pulse would have crossed a programmable threshold.

The second data path pertains to the trigger formation and is output through the P0 connector and VXS backplane. This serial data stream is processed at 250 MSPS and consists of either the sum of samples, or hit bit patterns. In order to maintain line balancing, the Aurora protocol is implemented over two lanes of the VXS backplane fabric for an aggregate

Figure 3.61: The fADC250

data transfer rate of 4 Gbps. The fADC250 module is shown in Fig. 3.61, and a summary of its specifications in fig. 3.62.

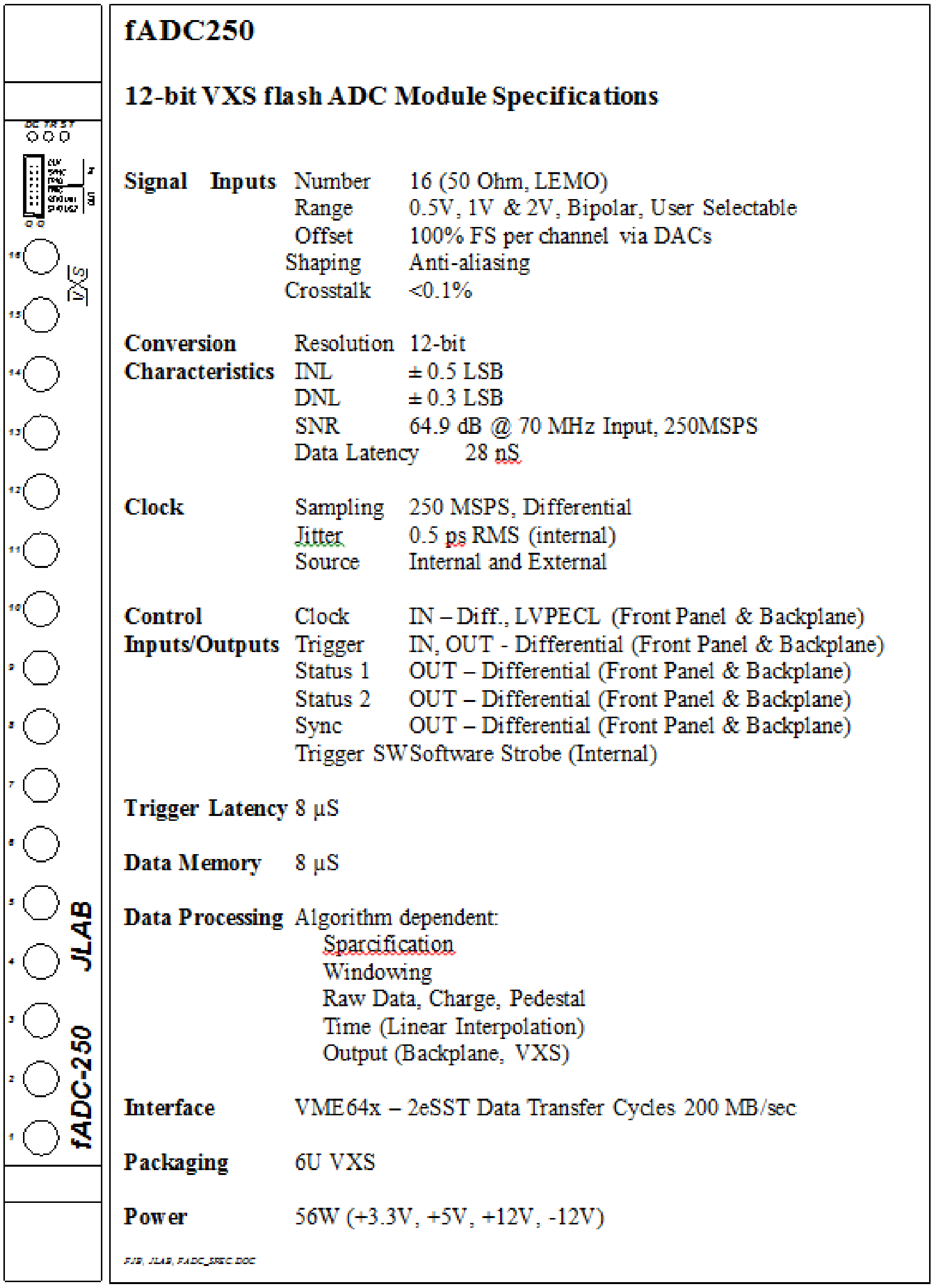

**fADC250**

**12-bit VXS flash ADC Module Specifications**

| | | |
|---|---|---|
| **Signal Inputs** | Number | 16 (50 Ohm, LEMO) |
| | Range | 0.5V, 1V & 2V, Bipolar, User Selectable |
| | Offset | 100% FS per channel via DACs |
| | Shaping | Anti-aliasing |
| | Crosstalk | <0.1% |
| **Conversion Characteristics** | Resolution | 12-bit |
| | INL | ± 0.5 LSB |
| | DNL | ± 0.3 LSB |
| | SNR | 64.9 dB @ 70 MHz Input, 250MSPS |
| | Data Latency | 28 nS |
| **Clock** | Sampling | 250 MSPS, Differential |
| | Jitter | 0.5 ps RMS (internal) |
| | Source | Internal and External |
| **Control Inputs/Outputs** | Clock | IN – Diff., LVPECL (Front Panel & Backplane) |
| | Trigger | IN, OUT - Differential (Front Panel & Backplane) |
| | Status 1 | OUT – Differential (Front Panel & Backplane) |
| | Status 2 | OUT – Differential (Front Panel & Backplane) |
| | Sync | OUT – Differential (Front Panel & Backplane) |
| | Trigger SW | Software Strobe (Internal) |
| **Trigger Latency** | 8 µS | |
| **Data Memory** | 8 µS | |
| **Data Processing** | Algorithm dependent:<br>Sparcification<br>Windowing<br>Raw Data, Charge, Pedestal<br>Time (Linear Interpolation)<br>Output (Backplane, VXS) | |
| **Interface** | VME64x – 2eSST Data Transfer Cycles 200 MB/sec | |
| **Packaging** | 6U VXS | |
| **Power** | 56W (+3.3V, +5V, +12V, -12V) | |

FJB, JLAB, FADC_SPEC.DOC

Figure 3.62: Specifications Summary for the fADC250

### fADC125

The fADC125 is a 12-bit flash Analog-to-Digital Converter, 6U VXS-compliant module used with the FDC and CDC tracking detectors. It employs ADC chips with pipeline architectures for high sample rates at reduced power consumption from Linear Technology. The LTC2283, a two channel device, forms the core of the fADC125. The backend of the module is enhanced with the use of Xilinx XC6SLX25, XC3SD3400 and XCS500 FPGAs which, by virtue of their vast resources, allow for tailoring the functionality of the module with firmware updates via VME. Fig. 3.63 shows the architecture of the fADC125.

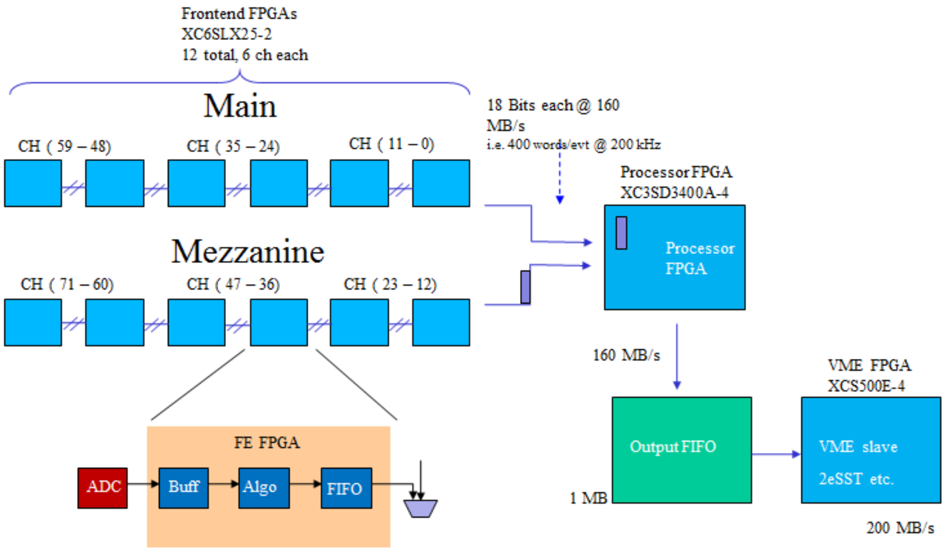

Figure 3.63: The fADC125 architecture

The fADC125 module consists of two PCBs: main and mezzanine. Each of XC6SLX25 FPGAs handles six input channels, or three ADC chips, and data is transferred through serial daisy-chain busses to the XC3SD3400 processor FPGA. Data is first processed through the algorithm loaded onto the frontend FPGAs and buffered into FIFOs for further processing and event building onto the processor FPGA. Communications, clocking and synchronization through VME and the VXS P0 is then handled by the XCS500 FPGA. Firmware and data processing architectures followed the development of the fADC250 and were adapted to this ADC module. The fADC125 module is shown in Fig. 3.64 and a summary of its specifications in fig. 3.65.

### TDCs

The first development of a pipelined module at JLab was the F1TDCV1, which was based on the F1 ASIC developed for the Compass experiment at CERN. Its block diagram in fig. 5.18 shows the F1TDC chip as the core functional element of the F1 series of TDC modules. Newer versions of this TDC were developed to address the needs of Hall D and serves as a single TDC development platform: the F1TDCV2 with 32 ECL-compliant input channels and resolution less than 60 ps; the F1TDCV3 with 48 LVDS-compliant input channels and resolution less than 100ps for the FDC tracking detector, wires only. Each of the modules consists of main

Figure 3.64: The fADC125

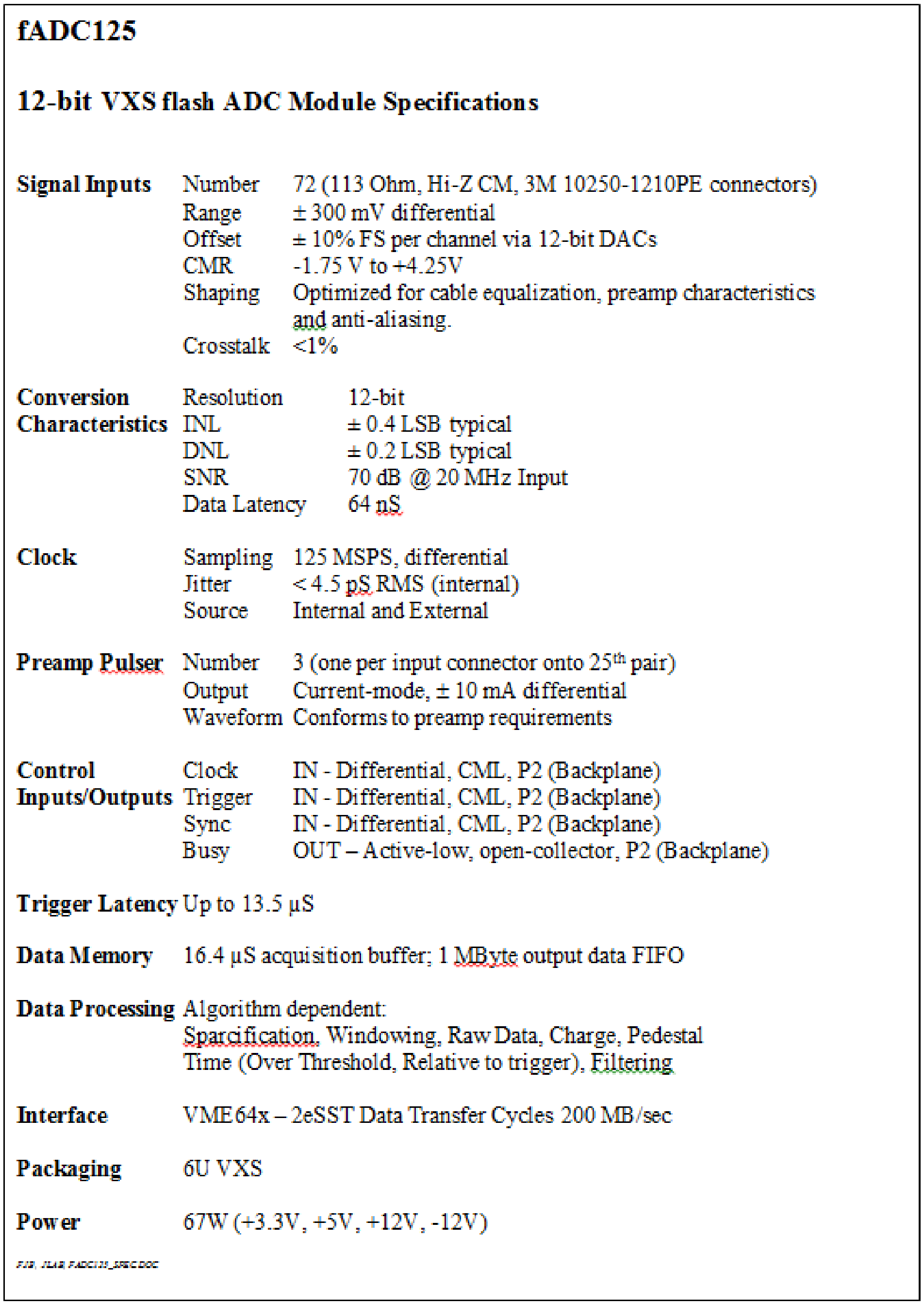

**fADC125**

**12-bit VXS flash ADC Module Specifications**

| | | |
|---|---|---|
| **Signal Inputs** | Number | 72 (113 Ohm, Hi-Z CM, 3M 10250-1210PE connectors) |
| | Range | ± 300 mV differential |
| | Offset | ± 10% FS per channel via 12-bit DACs |
| | CMR | -1.75 V to +4.25V |
| | Shaping | Optimized for cable equalization, preamp characteristics and anti-aliasing. |
| | Crosstalk | <1% |
| **Conversion Characteristics** | Resolution | 12-bit |
| | INL | ± 0.4 LSB typical |
| | DNL | ± 0.2 LSB typical |
| | SNR | 70 dB @ 20 MHz Input |
| | Data Latency | 64 nS |
| **Clock** | Sampling | 125 MSPS, differential |
| | Jitter | < 4.5 pS RMS (internal) |
| | Source | Internal and External |
| **Preamp Pulser** | Number | 3 (one per input connector onto 25th pair) |
| | Output | Current-mode, ± 10 mA differential |
| | Waveform | Conforms to preamp requirements |
| **Control Inputs/Outputs** | Clock | IN - Differential, CML, P2 (Backplane) |
| | Trigger | IN - Differential, CML, P2 (Backplane) |
| | Sync | IN - Differential, CML, P2 (Backplane) |
| | Busy | OUT – Active-low, open-collector, P2 (Backplane) |
| **Trigger Latency** | Up to 13.5 µS | |
| **Data Memory** | 16.4 µS acquisition buffer; 1 MByte output data FIFO | |
| **Data Processing** | Algorithm dependent:<br>Sparcification, Windowing, Raw Data, Charge, Pedestal<br>Time (Over Threshold, Relative to trigger), Filtering | |
| **Interface** | VME64x – 2eSST Data Transfer Cycles 200 MB/sec | |
| **Packaging** | 6U VXS | |
| **Power** | 67W (+3.3V, +5V, +12V, -12V) | |

FJB, JLAB FADC125_SPEC.DOC

Figure 3.65: Specification summary for the fADC125

and mezzanine PCBs. The TOF detector, with its higher resolution requirements, employs the commercially available VX1290A TDC from CAEN with 32 ECL-compliant input channels and has resolution less than 35 ps.

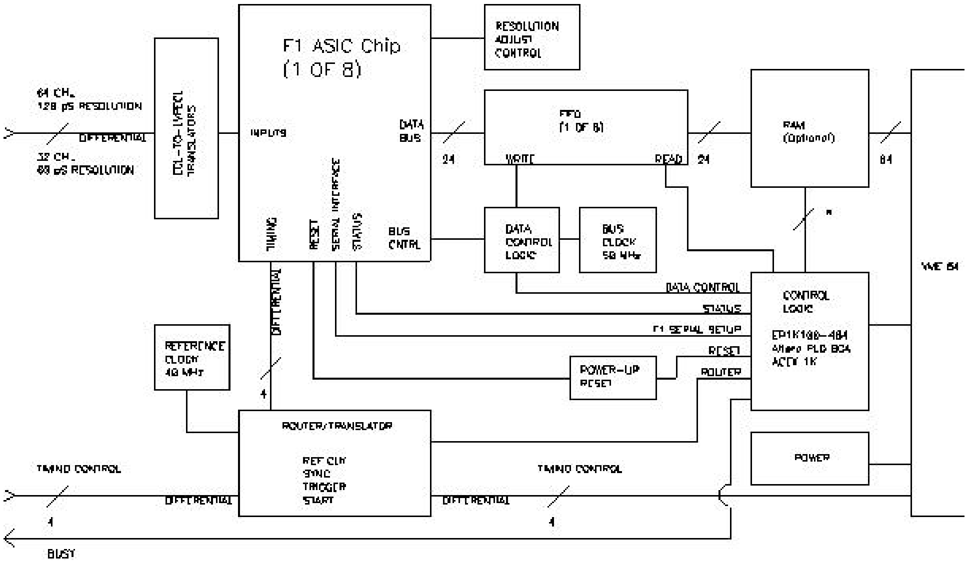

Figure 3.66: Block diagram of the early F1TDCV1

The core of our TDC modules is the F1 TDC chip. A functional block diagram of the F1 ASIC chip is shown in fig. **??**. This chip uses digital delay techniques to measure time by means of a 19-tap asymmetric ring oscillator with delay-locked loop (DLL) control. Each of the pipelined F1 chips provides eight channels nominally at 120 pS LSB or four channels at 60 pS LSB. Internal FIFOs allow for storage of 16 hits per channel in leading and/or trailing edge modes.

A key feature of the F1 chip is a Trigger Matching processing unit, which allows for selection of hits within a programmable time window and latency from the occurrence of a valid trigger input. Hits that fall outside of the window, and latency settings, are suppressed from the output buffer and cleared from the hit FIFO. The trigger matching feature is used in common start/stop and synchronous measurement modes. In common start/stop mode, a Start signal resets the internal measurement counter and a Trigger signal sets the measurement window. Hits falling within these two signals will always be accepted by the trigger matching unit. In synchronous mode, a Synch-Reset signal is used to reset the internal measurement counter and thus synchronize all TDCs in an experiment. Internal start signals are automatically generated at a programmable rate. The trigger matching unit validates hits within the programmed window and latency. Headers and trailers identifying the channel, chip, trigger time and event number can be output to delineate events. The dynamic range is 7.8 $\mu$S at 120 pS LSB and 3.9 $\mu$S at 60 pS.

To ensure stability and measurement reliability, each F1 chip is DLL-regulated against temperature drifts and manufacturing tolerances. The feedback loop employs a phase-frequency detector, a loop filter and a voltage regulator, which drives the substrate or core of the F1 chip. In this manner, delays within the internal Delay Locked Loop (DLL) are kept constant, which translates into a stable LSB resolution or bin size. The F1 chip is configured via a serial interface

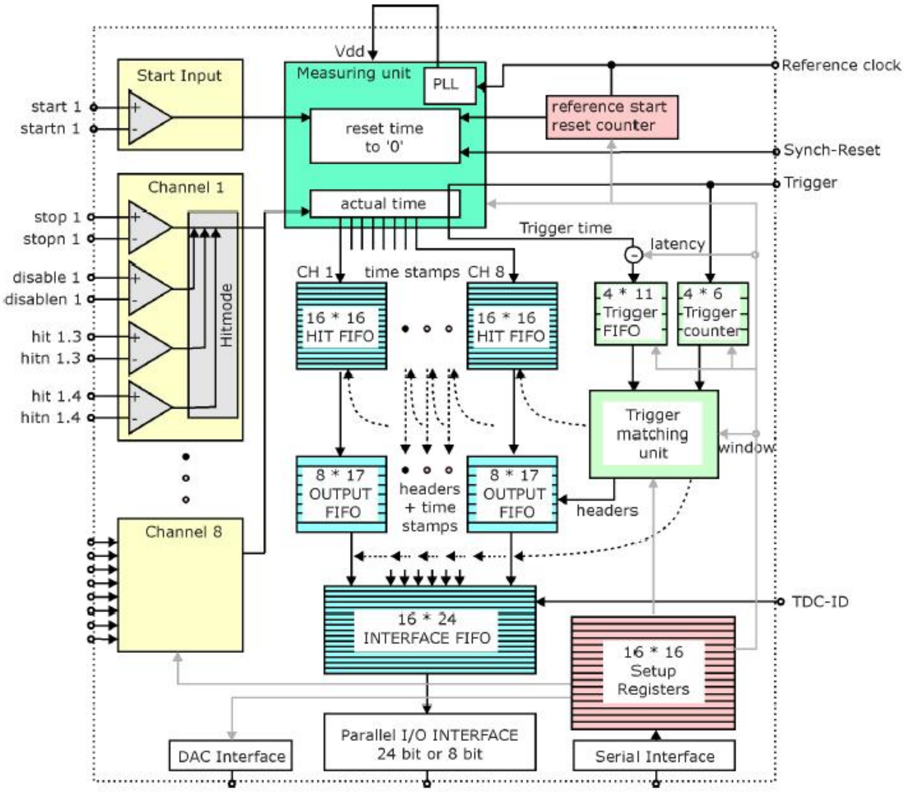

Figure 3.67: F1 ASIC blocki diagram

port, which accesses 16 registers.

Data from each F1 chip is readout via a 24-bit parallel port into a 4 Mbit FIFO. An Altera EP3C80F780 FPGA, with over 2.5 Mbit memory, processes data into event building, VME interfacing, and VXS clock and synchronization tasks. The clock frequency for the F1TDCs is 31.25MHz, which is derived and synchronized from the master 250MHz clock through the TI and the SD modules. Figs. 3.68 and 3.69 show the F1TDCV2 module and its specifications, respectively; figs. 3.70 and 3.71 show the F1TDCV3 module and its specifications, respectively.

#### Discriminator

The VME64x compliant 16-Channel Discriminator/Scaler Board contains 16 non-updating dual-threshold discriminators, programmable digital delays, two 32-bit scalers per discriminator and threshold. The discriminator pulses are output as differential ECL logic levels through two front-panel headers. One group of outputs connect to a TDC and the other group can be used as input to trigger logic. Both TDC and trigger output channels can individually be enabled/disabled, with outputs widths and delays being user programmable. All programming is done through VME registers. Fig. 3.72 shows the block diagram of the JLab discriminator.

All discriminators and logic reside on a 6U standard VME mainboard. Each channel contains two analog receiver fast comparators (discriminators), and pulsers. Each discriminator channel has 2 programmable thresholds which can be programmed from VME. The output pulse width is common to the TDC and trigger discriminator channels separately and is programmable from VME. The digital delay circuit delays each discriminator pulse up to 512 ns in 4 ns steps (used for trigger output path and scaler input path when using an external gate input). It is implemented with a high-speed (250MHz) FIFO for each discriminator channel. The delay is software selectable for the trigger output, trigger scaler input, and TDC scaler input. Each discriminator output pulse is recorded by a 32 bit counter (scaler) which can be gated with the external NIM Gate input. Scalers can be latched, read, and cleared through VME. There is a 23OR 24 (NIM level) ouput that is the logical OR of all the unmasked discriminator outputs. Discriminator outputs are provided as dECL levels on the front panel for interfacing with TDCs and trigger logic. The VME interface is A32/A24/D32 with support for interrupts. The Discriminator module is shown in Fig. 3.73 and its specifications are shown on fig. 3.74.

### 3.9.3 Grounding, Shielding and EMI

A systematic approach to grounding and shielding of equipment was implemented to ensure good performance from the detectors and the electronics. The single-point ground topology provides superior characteristics compared to any other approach and must be considered as extended bonding, which relies on a grounding grid built into the floor of the experimental areas and as shown in fig. 3.75. Grounding is effected by properly segregating and managing different types of sources, loads and their interconnections. Fig. 3.76 illustrates the grounding implementation diagrammatically.

Low noise susceptibility and emissions from the readout of all the detector sub-systems provide the necessary basis for good resolution. Bonding attachments are designated to be used with specific detectors which require very low noise while other bonding pads on the grid are designated to be used with devices which are characteristically noisy, such as pumps and the high power solenoid power supply for example. Wide bandwidth and low impedance bonding is implemented by means of thick cable (4/0). The FDC, for example and noted as

Figure 3.68: F1TDCV2

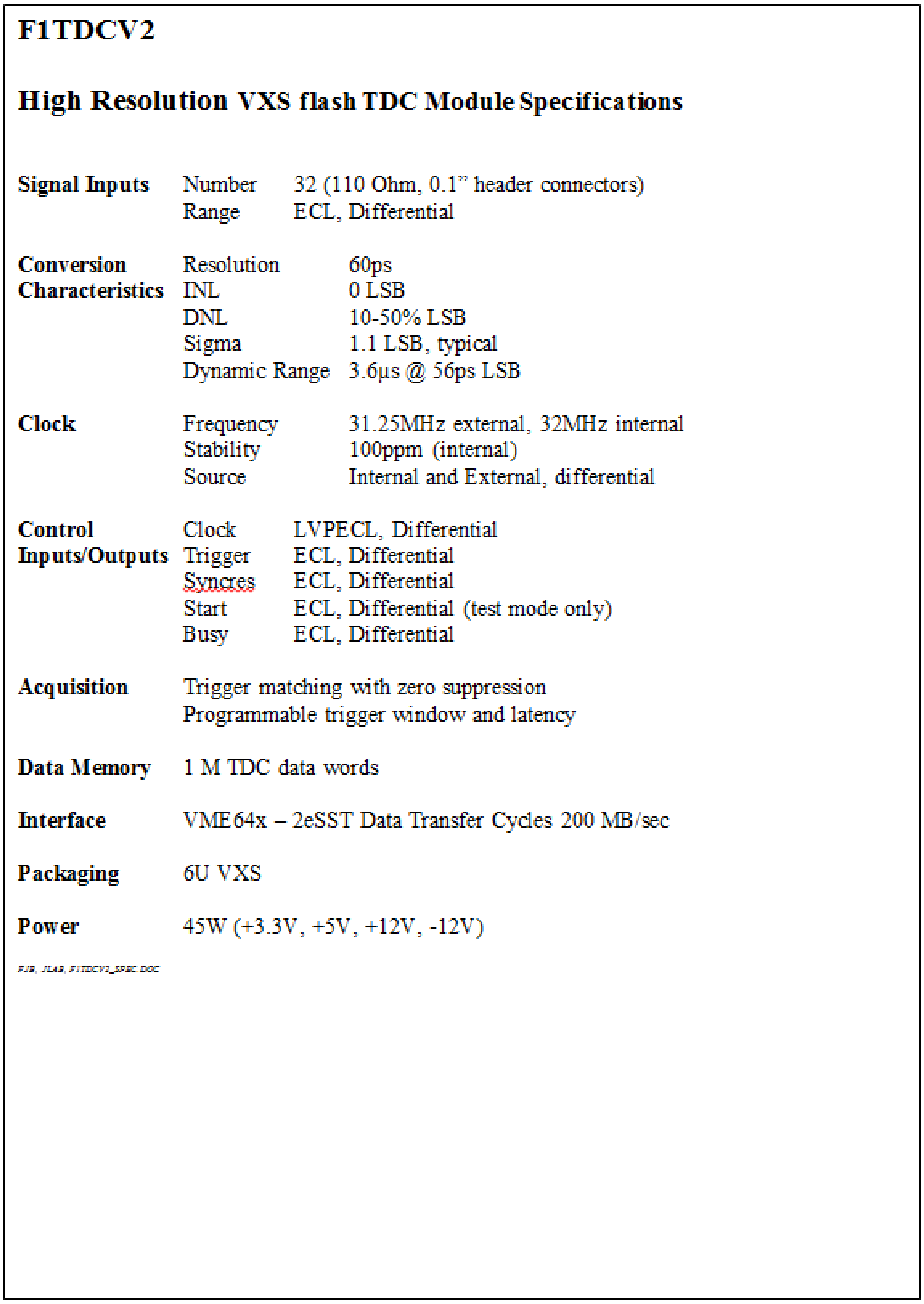

**F1TDCV2**

**High Resolution VXS flash TDC Module Specifications**

| | | |
|---|---|---|
| **Signal Inputs** | Number | 32 (110 Ohm, 0.1" header connectors) |
| | Range | ECL, Differential |
| **Conversion Characteristics** | Resolution | 60ps |
| | INL | 0 LSB |
| | DNL | 10-50% LSB |
| | Sigma | 1.1 LSB, typical |
| | Dynamic Range | 3.6µs @ 56ps LSB |
| **Clock** | Frequency | 31.25MHz external, 32MHz internal |
| | Stability | 100ppm (internal) |
| | Source | Internal and External, differential |
| **Control Inputs/Outputs** | Clock | LVPECL, Differential |
| | Trigger | ECL, Differential |
| | Syncres | ECL, Differential |
| | Start | ECL, Differential (test mode only) |
| | Busy | ECL, Differential |
| **Acquisition** | Trigger matching with zero suppression<br>Programmable trigger window and latency | |
| **Data Memory** | 1 M TDC data words | |
| **Interface** | VME64x – 2eSST Data Transfer Cycles 200 MB/sec | |
| **Packaging** | 6U VXS | |
| **Power** | 45W (+3.3V, +5V, +12V, -12V) | |

*FJB, JLAB, F1TDCV2_SPEC.DOC*

Figure 3.69: F1TDCV2 specifications

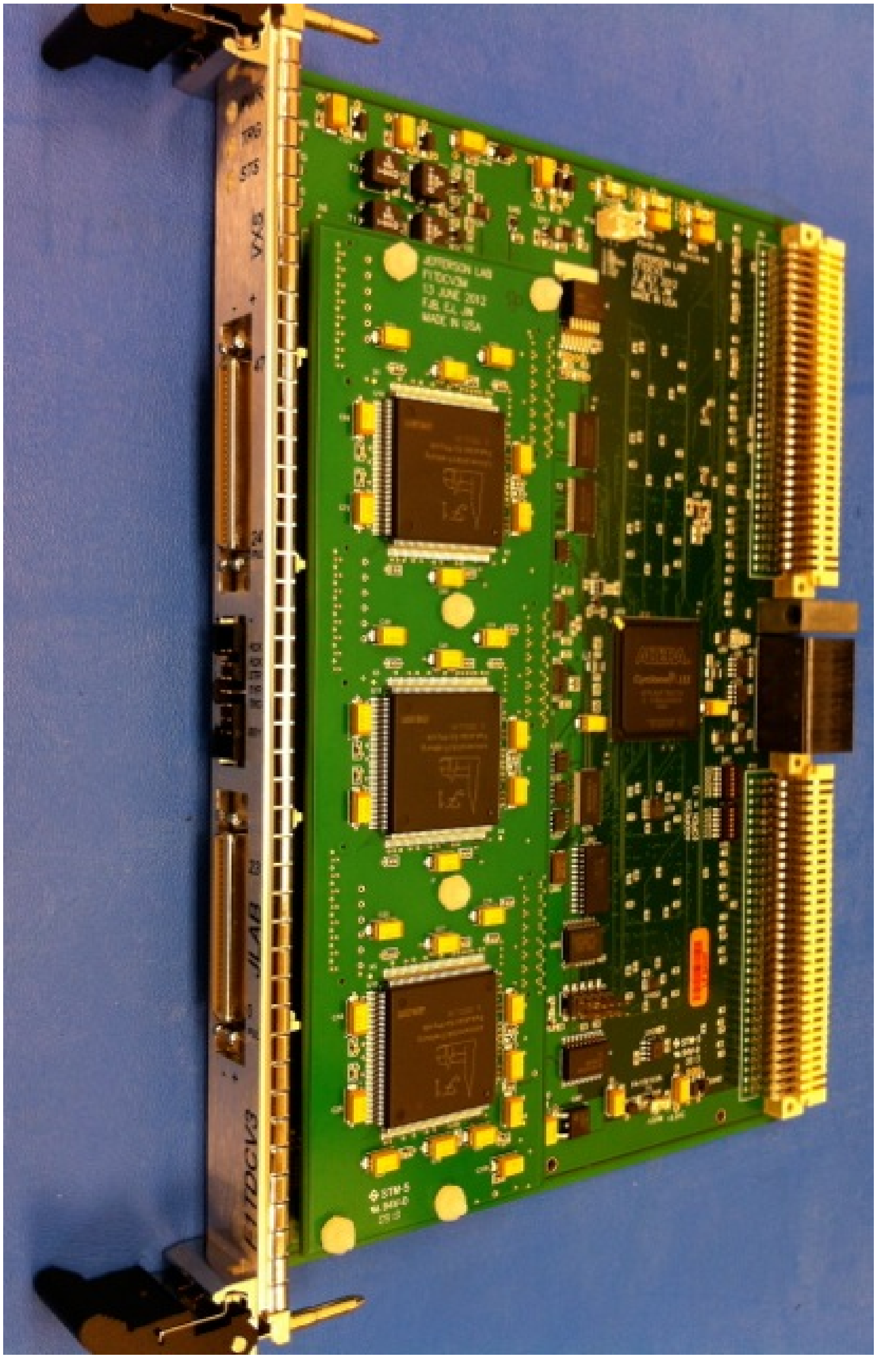

Figure 3.70: F1TDCV3

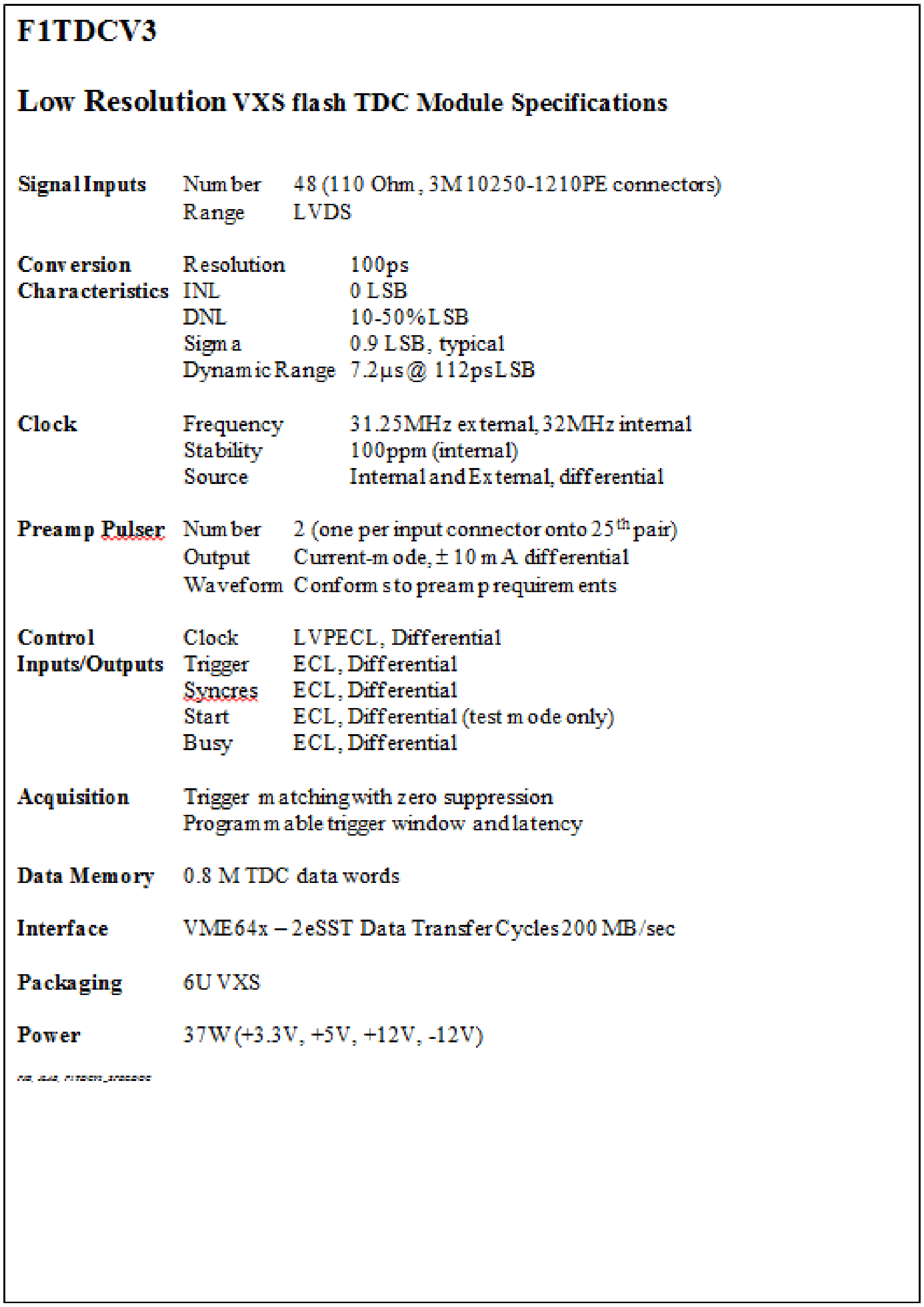

**F1TDCV3**

**Low Resolution VXS flash TDC Module Specifications**

| | | |
|---|---|---|
| **Signal Inputs** | Number | 48 (110 Ohm, 3M 10250-1210PE connectors) |
| | Range | LVDS |
| **Conversion Characteristics** | Resolution | 100ps |
| | INL | 0 LSB |
| | DNL | 10-50% LSB |
| | Sigma | 0.9 LSB, typical |
| | Dynamic Range | 7.2µs @ 112ps LSB |
| **Clock** | Frequency | 31.25MHz external, 32MHz internal |
| | Stability | 100ppm (internal) |
| | Source | Internal and External, differential |
| **Preamp Pulser** | Number | 2 (one per input connector onto 25th pair) |
| | Output | Current-mode, ± 10 mA differential |
| | Waveform | Conforms to preamp requirements |
| **Control Inputs/Outputs** | Clock | LVPECL, Differential |
| | Trigger | ECL, Differential |
| | Syncres | ECL, Differential |
| | Start | ECL, Differential (test mode only) |
| | Busy | ECL, Differential |
| **Acquisition** | Trigger matching with zero suppression<br>Programmable trigger window and latency | |
| **Data Memory** | 0.8 M TDC data words | |
| **Interface** | VME64x – 2eSST Data Transfer Cycles 200 MB/sec | |
| **Packaging** | 6U VXS | |
| **Power** | 37W (+3.3V, +5V, +12V, -12V) | |

Figure 3.71: F1TDCV3 specifications

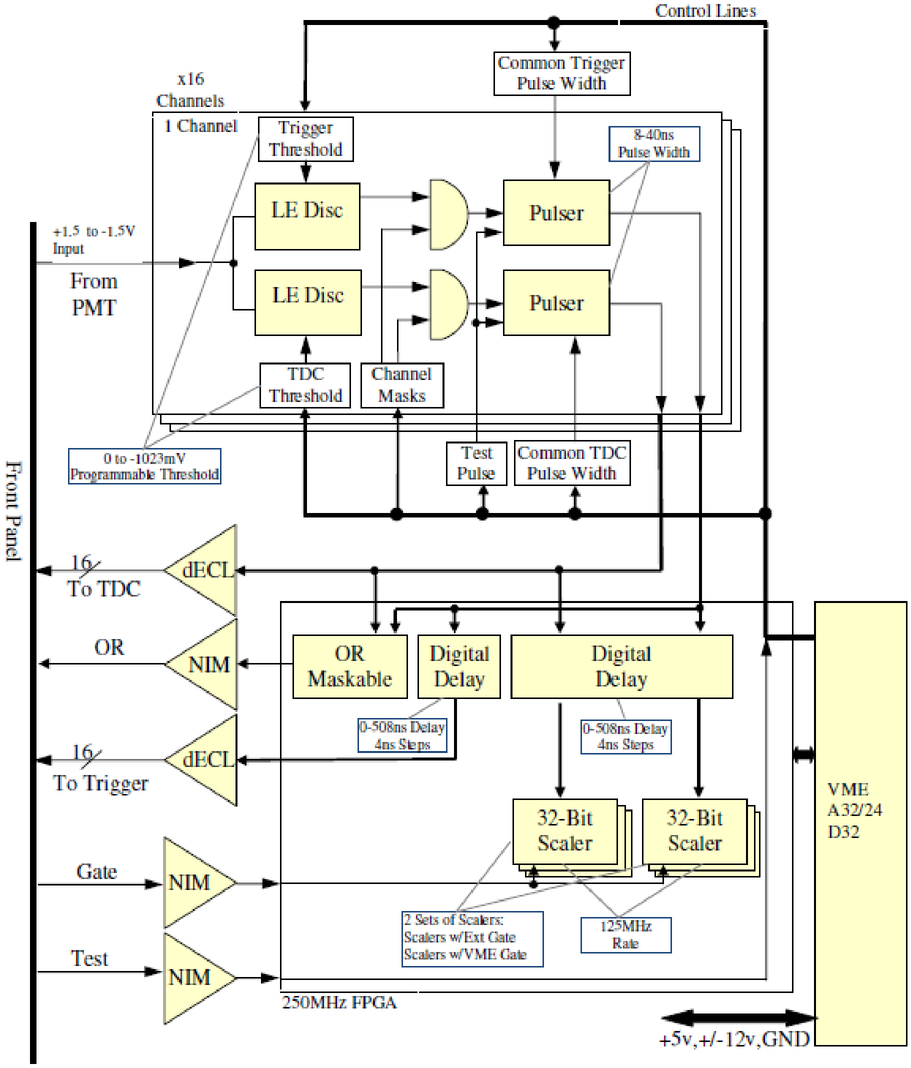

Figure 3.72: JLab discriminator block diagram

Figure 3.73: The JLab 16-ch discriminator

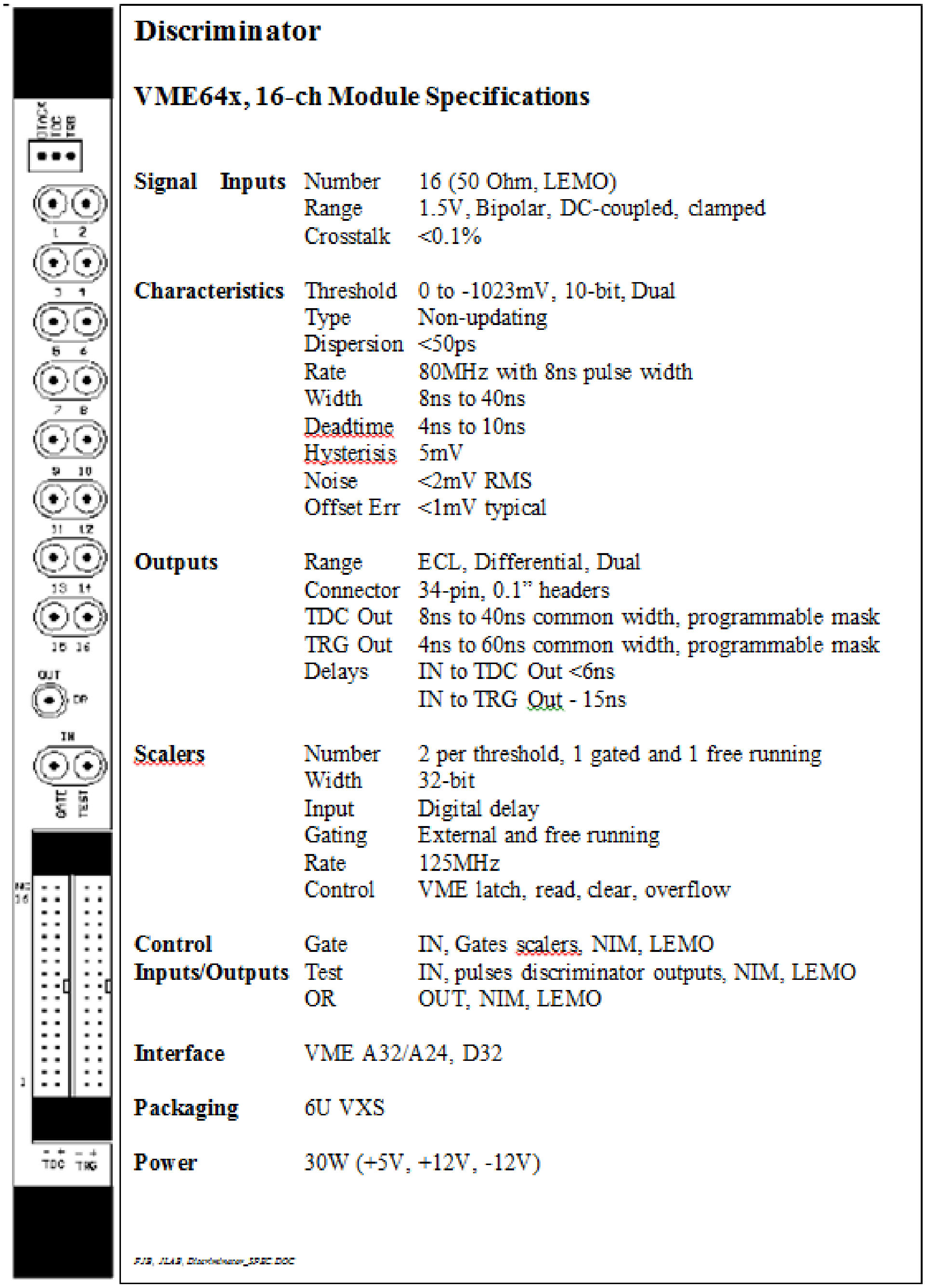

**Discriminator**

**VME64x, 16-ch Module Specifications**

| | | |
|---|---|---|
| **Signal Inputs** | Number | 16 (50 Ohm, LEMO) |
| | Range | 1.5V, Bipolar, DC-coupled, clamped |
| | Crosstalk | <0.1% |
| **Characteristics** | Threshold | 0 to -1023mV, 10-bit, Dual |
| | Type | Non-updating |
| | Dispersion | <50ps |
| | Rate | 80MHz with 8ns pulse width |
| | Width | 8ns to 40ns |
| | Deadtime | 4ns to 10ns |
| | Hysterisis | 5mV |
| | Noise | <2mV RMS |
| | Offset Err | <1mV typical |
| **Outputs** | Range | ECL, Differential, Dual |
| | Connector | 34-pin, 0.1" headers |
| | TDC Out | 8ns to 40ns common width, programmable mask |
| | TRG Out | 4ns to 60ns common width, programmable mask |
| | Delays | IN to TDC Out <6ns<br>IN to TRG Out - 15ns |
| **Scalers** | Number | 2 per threshold, 1 gated and 1 free running |
| | Width | 32-bit |
| | Input | Digital delay |
| | Gating | External and free running |
| | Rate | 125MHz |
| | Control | VME latch, read, clear, overflow |
| **Control Inputs/Outputs** | Gate | IN, Gates scalers, NIM, LEMO |
| | Test | IN, pulses discriminator outputs, NIM, LEMO |
| | OR | OUT, NIM, LEMO |
| **Interface** | VME A32/A24, D32 | |
| **Packaging** | 6U VXS | |
| **Power** | 30W (+5V, +12V, -12V) | |

*FJB, JLAB, Discriminator_SPEC.DOC*

Figure 3.74: JLab discriminator specifications

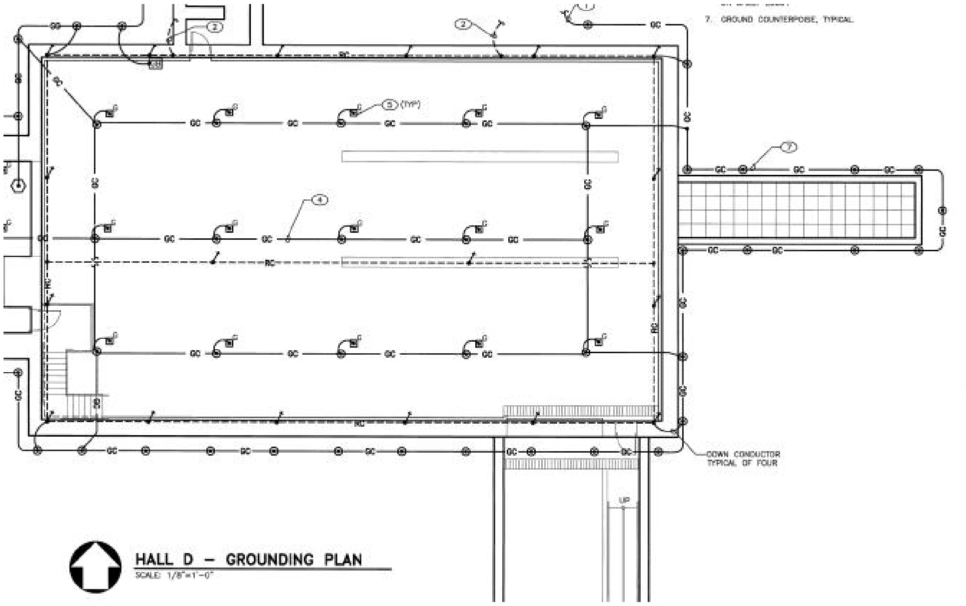

Figure 3.75: Grounding grid in Hall D

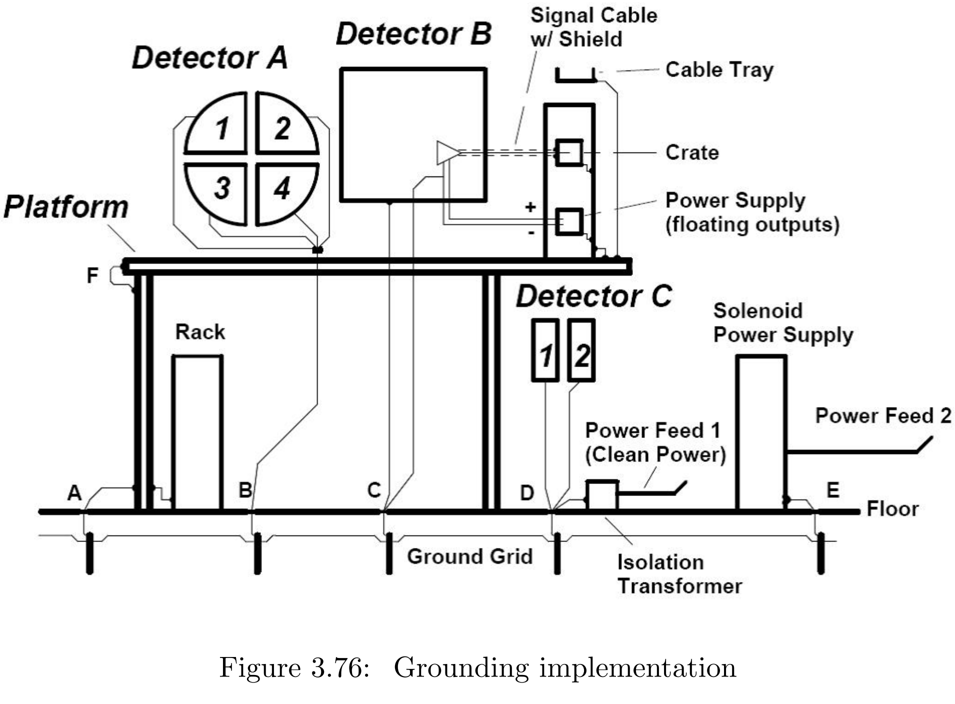

Figure 3.76: Grounding implementation

A in the figure, has all grounds of its four packages connected together at the detector and then bonded to a "clean" ground pad on the grid. Single-point shielding is also employed by by bonding to a pad on the grid. This separates the FDC from noisy loads. Structures, such as the platform, are also bonded to the grid, but are kept separate from the clean detector grounds. Proper AC power distribution with its associated grounds follow a similar approach in segregating equipment based on application. Ground loops are also minimized, except where interconnections are made through coaxial cables.

Due to their required high sensitivity to low-level signals, Electro-Magnetic Interference (EMI and RFI) is a major cause of noise observed in the readout of particle detectors. Good grounding and shielding techniques are complemented by employing equipment with low EMI/RFI characteristics, and by proper placement in the experimental area. In view of such demanding requirements, a sufficiently stringent plan that manages the deployment of equipment in the hall is necessary to ensure good overall performance, and limits the sources of interference. The following commercial standards are adopted in Hall D: FCC part 15 Class B, CISPR 11/ EN 55011 Class B, CISPR 22/ EN 55022 Class B and EN 61000-6-3. It should be noted that some equipment, notably control hardware, do not generally conform to class B, and their placement is segregated from sensitive detectors and electronics.

### HV and LV Systems

The high voltage (HV) and low voltage (LV) systems, including distribution hardware, were implemented to take full advantage of the grounding and shielding architecture described earlier, and in keeping with low noise requirements for good performance of the detectors and readout electronics. As such, all the supplies, with the exception of small modules used with the FCAL, are of the floating type and referenced to the detector ground and ground grid in the experimental hall. The HV and LV systems are based on commercially available units from CAEN and Wiener, respectively.

The HV system consists of the CAEN SY1527 chassis with modules A1550P, A1550N and A1535SN. These modules have floating outputs or returns, clamped to ground, and has interlocks for safety. HV channels are distributed on the CDC HVB, the FDC PCBs, and each channel from the A1535SN modules feeds one PMT.

| Module | Type | Range | Connector | Channels | Detectors |
|---|---|---|---|---|---|
| A1550P | Positive | +5kV, 1mA | Radiall | 24 | CDC, FDC |
| A1550N | Negative | -5kV, 1mA | Radiall | 24 | CDC, FDC |
| A1535SN | Negative | -3.5kV, 3mA | SHV | 24 | TAGH,PSC,TOF |

Table 3.30: HV system

The LV system consists of the Wiener MPOD chassis with low noise modules MPV8008, MPV8030, MPV8120 and ISEG EHS F201x_106 F. These modules have floating outputs clamped to ground and interlocks for safety. All the LV channels are distributed appropriately by detector subsystem and employ custom distribution chassis, or are integrated into the detector readout boards. Bipolar supply requirements are implemented at the hardware level by connecting supply channels in series and referencing the mid-point to the detector ground.

A BCAL distribution chassis is shown in fig. **??** and others are similar.

| Module | Type | Range | Connector | Channels | Detectors | Usage |
|---|---|---|---|---|---|---|
| MPV8008 | Floating | 8V, 5A | D-sub | 8 | TAGM,PS ST,CDC FDC,BCAL | Power |
| MPV8030 | Floating | 30V, 2.5A | D-sub | 8 | FDC, BP | Disc. Vth Power |
| MPV8120 | Floating | 120V, 100mA | D-sub | 8 | TAGM | SiPM Bias |
| ISEG | Floating | 100V, 10mA | Redel | 16 | PS,ST,BCAL | SiPM Bias |

Table 3.31: LV system

Figure 3.77: LV distribution chassis

### Cabling and Racks

Various cable types are employed in Hall D, including RG-58 coaxial for signal transmission, RG-59 coaxial for HV, twisted-pair for signal transmission and multi-wire for HV and LV power distribution and control. Regardless of type, all the cables are shielded with their shields referenced to ground to minimize common-mode noise pickup and emissions and for safety.

An important consideration in large installations is to ensure that there is a good level of fire safety, and limiting the propagation of potential fires by employing appropriately rated cables. Hall D follows the standard National Electrical Code for fire safety (NEC NFPA 70, 2011 Edition) enforced in the USA and UL listing of CL2 cables, or better. Installation is guided by the NECA/NEMA 105-2007 standard for installation of cable tray systems, which is extensively applied throughout the experimental area.

Racks hold the various chassis and crates throughout the experimental areas and are commercial-off-the-shelf (COTS) items. The Hammond C4F247736 is the standard rack in use and was chosen for its welded construction, with grounding studs, robust construction and enough usable height (44U) to hold three chassis while fitting under the platforms. Vertical and horizontal cable managers facilitate cabling and allow for a clean and safe installation. Fig. 3.78 shows the location of the racks in Hall D and fig. 3.79 shows a section of the electronics installation.

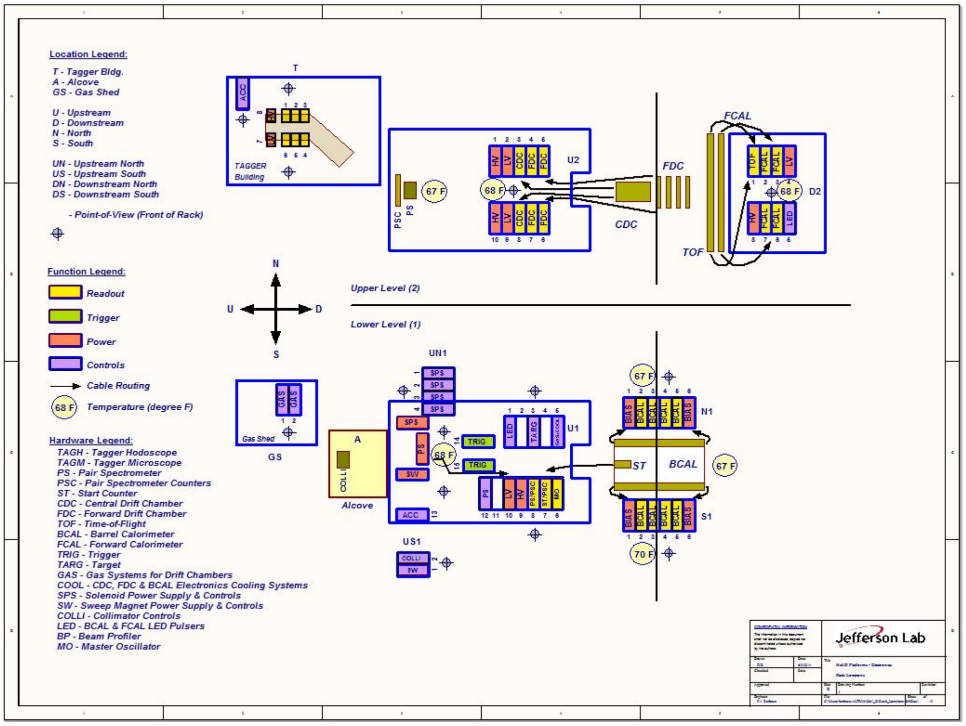

Figure 3.78: Rack locations

Figure 3.79: Electronics installation

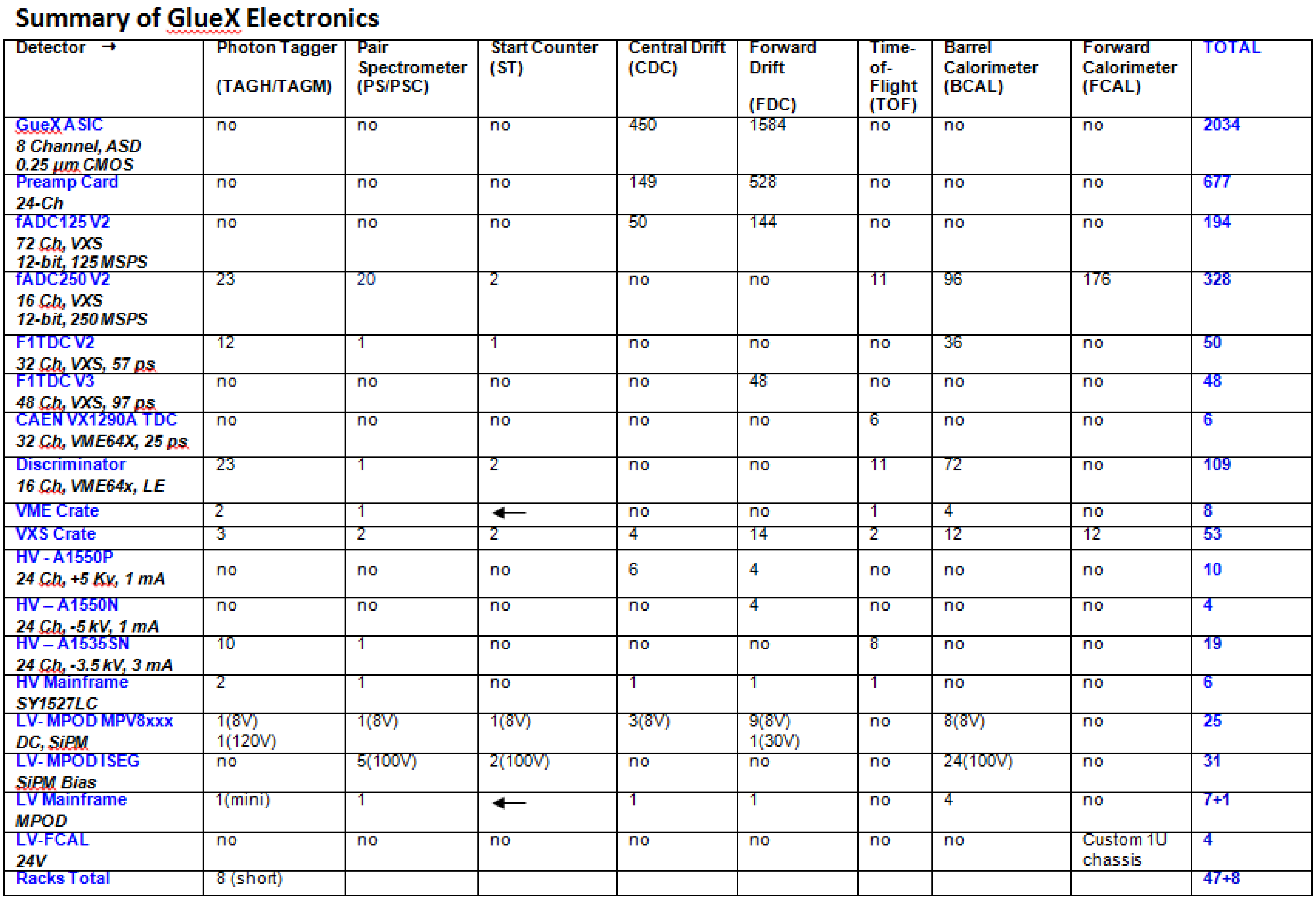

**Summary of GlueX Electronics**

| Detector → | Photon Tagger (TAGH/TAGM) | Pair Spectrometer (PS/PSC) | Start Counter (ST) | Central Drift (CDC) | Forward Drift (FDC) | Time-of-Flight (TOF) | Barrel Calorimeter (BCAL) | Forward Calorimeter (FCAL) | TOTAL |
|---|---|---|---|---|---|---|---|---|---|
| GueX ASIC<br>*8 Channel, ASD*<br>*0.25 μm CMOS* | no | no | no | 450 | 1584 | no | no | no | 2034 |
| Preamp Card<br>*24-Ch* | no | no | no | 149 | 528 | no | no | no | 677 |
| fADC125 V2<br>*72 Ch, VXS*<br>*12-bit, 125 MSPS* | no | no | no | 50 | 144 | no | no | no | 194 |
| fADC250 V2<br>*16 Ch, VXS*<br>*12-bit, 250 MSPS* | 23 | 20 | 2 | no | no | 11 | 96 | 176 | 328 |
| F1TDC V2<br>*32 Ch, VXS, 57 ps* | 12 | 1 | 1 | no | no | no | 36 | no | 50 |
| F1TDC V3<br>*48 Ch, VXS, 97 ps* | no | no | no | no | 48 | no | no | no | 48 |
| CAEN VX1290A TDC<br>*32 Ch, VME64X, 25 ps* | no | no | no | no | no | 6 | no | no | 6 |
| Discriminator<br>*16 Ch, VME64x, LE* | 23 | 1 | 2 | no | no | 11 | 72 | no | 109 |
| VME Crate | 2 | 1 | ← | no | no | 1 | 4 | no | 8 |
| VXS Crate | 3 | 2 | 2 | 4 | 14 | 2 | 12 | 12 | 53 |
| HV - A1550P<br>*24 Ch, +5 Kv, 1 mA* | no | no | no | 6 | 4 | no | no | no | 10 |
| HV – A1550N<br>*24 Ch, -5 kV, 1 mA* | no | no | no | no | 4 | no | no | no | 4 |
| HV – A1535SN<br>*24 Ch, -3.5 kV, 3 mA* | 10 | 1 | no | no | no | 8 | no | no | 19 |
| HV Mainframe<br>*SY1527LC* | 2 | 1 | no | 1 | 1 | 1 | no | no | 6 |
| LV- MPOD MPV8xxx<br>*DC, SiPM* | 1(8V)<br>1(120V) | 1(8V) | 1(8V) | 3(8V) | 9(8V)<br>1(30V) | no | 8(8V) | no | 25 |
| LV- MPOD ISEG<br>*SiPM Bias* | no | 5(100V) | 2(100V) | no | no | no | 24(100V) | no | 31 |
| LV Mainframe<br>*MPOD* | 1(mini) | 1 | ← | 1 | 1 | no | 4 | no | 7+1 |
| LV-FCAL<br>*24V* | no | no | no | no | no | no | no | Custom 1U chassis | 4 |
| Racks Total | 8 (short) | | | | | | | | 47+8 |

Figure 3.80: Summary of installed electronics in Hall D

## 3.10 Trigger

### 3.10.1 Trigger Summary [46]

The main parameters and properties of the TRIGGER are given in Tables 3.32 and 3.33.

Table 3.32: TRIGGER properties.

| Item | Value |
|---|---|
| L1 trigger rate (for high-lumi runs) | <200 kHz |
| L1 algorithm | energy balance in calorimeters (main algorithm), hits count |
| Detectors used in trigger: | |
| energy sum | BCAL, FCAL |
| hit count | TAGM, TAGH, SC, TOF, PSC |
| Trigger latency | $\sim 3.2\mu$s fixed latency |
| L3 trigger rate | 20 kHz |
| Algorithm | Full event reconstruction on L3 farms |
| Number of farm nodes | TBD |

Table 3.33: TRIGGER channel counts.

| L1 modules | Description | Quantity |
|---|---|---|
| Crate Trigger Processor CTP | Sums energies from fADC250-MHz in the crate, form hit pattern | 26 |
| Sub-System Processor SSP | Sums energies from BCAL/FCAL crates, passes hit patterns to GTP | 8 |
| Global Trigger Processor GTP | Runs trigger algorithms | 1 |
| Trigger Supervisor TS | Handles trigger types, distribute triggers and clock | 1 |
| Trigger Distribution TD | Distributes triggers and clock to readout crates | 9 |
| Trigger Interface TI | Receives triggers and clock from SD | 52 (56) |
| Signal Distribution SD | Distributes triggers and clock inside the crate | 52 (56) |

---

[46] *SVN revision ID:* tdr_summary_trig.tex 13854 2014-06-12 04:42:15Z gen

## 3.11 DAQ and Online

### 3.11.1 DAQ and Online Summary [47]

The main parameters and properties of Online Computing including the DAQ are given in Tables 3.34, 3.35 and 3.36. A listing of crates and electronic modules used by the DAQ system are given in Table 3.24.

Table 3.34: Online/DAQ components.

| Item | Value |
|---|---|
| Hall network switch input ports | 1 Gbit/s TCP/IP Ethernet (copper) |
| Hall network switch uplink ports | 10 Gbit/s TCP/IP Ethernet (fiber) |
| Counting House main switch ports | 1 Gbit/s and 10 Gbit/s Ethernet (copper,fiber) |
| DAQ interconnect protocol in Counting House | TCP/IP over 40 Gbit/s Infiniband |
| DAQ base architecture | CODA3, 2-stage event building |
| Pre/post level 3 event monitoring | 20 kHz |
| Raid to silo network connection | Dual 10 Gbit/sec Ethernet (fiber) |
| Operating system on Counting House computers | RHEL6 (eventually RHEL7) |

Table 3.35: Online/DAQ channel counts.

| Item | Description | Quantity |
|---|---|---|
| Cisco 24-port endpoint switches | ROC and control uplinks | 12 |
| Cisco switch | Main Ethernet switch | 1 |
| Mellenox Infiniband switch | Central Infiniband switch | 1 |
| 32-port Digi terminal servers | Provides remote RS232 access | 8 |
| Netapps file server | Central file server | 1 |
| 16-core Dell servers | First stage event builders | 6 |
| 32-core Dell servers | Second stage event builder | 1 |
| RAID servers (150 hours storage) | Local event data storage | 2 @ 75 TB |
| Multi-core Dell servers | Online computing | 21 |

Table 3.36: DAQ rates.

| Item | Low Luminosity | High Luminosity |
|---|---|---|
| L1 Trigger rate | 20 kHz | 200 kHz |
| Average physics event size | 15 kB | 15 kB |
| Data rate (front-end) | 300 MB/s | 3000 MB/s |
| Data rate (tape) | 300 MB/s | 300 MB/s |

---

[47] *SVN revision ID:* tdr_summary_online.tex 13854 2014-06-12 04:42:15Z gen

## 3.12 Slow Controls

### 3.12.1 Slow Controls Summary [48]

The main parameters and properties of the Slow Controls are given in Tables 3.37 and 3.38.

Table 3.37: Slow Control properties.

| Item | Value |
|---|---|
| SCADA architecture foundation | EPICS |
| Display management framework | CSS BOY |
| Alarm handler | CSS BEAST |
| EPICS Archiving | JLab MYA |
| PLC Allen-Bradley communication protocol | EtherNet/IP |
| Communication protocol with Wiener chassis | SNMP |
| Communication protocol with CAEN chassis | Proprietary CAEN protocol over Ethernet |
| Communication protocol with FCAL bases | Custom protocol over Ethernet/CAN bridge |
| Communication protocol with microscope boards | Custom protocol over Ethernet |

Table 3.38: Slow Controls channel counts.

| Item | Description | Quantity |
|---|---|---|
| 16-core Dell Linux servers | EPICS softIOCs | 2 |
| 8-core Dell Linux servers | EPICS softIOCs | 1 |
| MOXA single board Linux computer | EPICS softIOC | 1 |
| VME Linux controllers | EPICS IOC | 3 |
| Allen-Bradley ControlLogix PLC CPU | Solenoid magnet controls | 1 |
| Allen-Bradley ControlLogix EN2T communication modules | Solenoid magnet controls | 4 |
| Allen-Bradley CompactLogix PLC CPUs | Detector controls | 5 |
| Allen-Bradley Point I/O PLC communication modules | Solenoid and detector controls | 7 |
| National Instruments PXI chassis | Solenoid magnet DAQ | 1 |
| RTA Serial-to-EtherNet/IP bridge modules | Magnet and detector controls | 8 |
| RTA Modbus-to-EtherNet/IP bridge modules | Magnet and detector controls | 1 |
| Anagate CAN-to-Ethernet bridge modules | Controls of FCAL PMT bases | 7 |

---

[48] *SVN revision ID:* tdr_summary_controls.tex 13854 2014-06-12 04:42:15Z gen

# Appendix A

# Calibration

# Appendix B

# Performance

## B.1 Tracking

# Bibliography

[1] G. McNicoll, “A study of photon sensitivity in the Hall D detector,” Tech. Rep. GlueX-doc-**36**, Carnegie Mellon University, 2000. `http://argus.phys.uregina.ca/cgi-bin/private/DocDB/ShowDocument?docid=36`.

[2] J. Kuhn and C. A. Meyer, “Acceptance Study for the GlueX detector system,” Tech. Rep. GlueX-doc-**264**, 2004. `http://argus.phys.uregina.ca/cgi-bin/private/DocDB/ShowDocument?docid=264`.

[3] C. A. Meyer, “A study of timing resolutions on particle identification in the HALL Ddectector at jefferson lab,” Tech. Rep. GlueX-doc-**14**, Carnegie Mellon University, 1999. `http://argus.phys.uregina.ca/cgi-bin/private/DocDB/ShowDocument?docid=14`.

[4] C. A. Meyer and P. Eugenio, “A Study of Compined $K$–$\pi$ Separation using Time–of–Flight Counters and a Gas Čerenkov Detector,” Tech. Rep. GlueX-doc-**15**, Carnegie Mellon University, 1998. `http://argus.phys.uregina.ca/cgi-bin/private/DocDB/ShowDocument?docid=15`.

[5] T. Sjostrand, L. Lonnblad, and S. Mrenna, “PYTHIA 6.2: Physics and manual,” `arXiv:hep-ph/0108264`.

[6] R. Brun *et al.*, 1986. GEANT3, CERN-DD/EE/84-1.

[7] M. Adinolfi, F. Ambrosino, A. Antonelli, M. Antonelli, F. Anulli, *et al.*, “The KLOE electromagnetic calorimeter,” *Nucl.Instrum.Meth.* **A461** (2001) 344.

[8] M. Adinolfi, F. Ambrosino, A. Antonelli, M. Antonelli, F. Anulli, *et al.*, “The KLOE electromagnetic calorimeter,” *Nucl.Instrum.Meth.* **A482** (2002) 364–386.

[9] M. Adinolfi, F. Ambrosino, A. Antonelli, M. Antonelli, F. Anulli, *et al.*, “The KLOE electromagnetic calorimeter,” *Nucl.Instrum.Meth.* **A494** (2002) 326–331.

[10] A. Antonelli, M. Antonelli, G. Barbiellini, M. Barone, S. Bertolucci, *et al.*, “Measurements of light yield, attenuation length and time response of long samples of ’blue’ scintillating fibers,” *Nucl.Instrum.Meth.* **A370** (1996) 367–371.

[11] R. Wigmans, *Calorimetry: Energy measurement in particle physics*, vol. 107 of *International Series of Monographs on Physics*. Oxford University Press, 2000.

[12] E. Chudakov *et al.*, "Summary of Hall D Subsystems," Specification D00000-00-00-S006, Jefferson Lab, May, 2013.
`https://misportal.jlab.org/jlabDocs/document.seam?id=79548`.

[13] J. Lagner, "Hall D GlueX Detector Barrel Calorimeter Sub-Assembly," Drawing D00000-01-07-1000, Jefferson Lab, Apr., 2009.
`https://misportal.jlab.org/jlabDocs/document.seam?id=65967`.

[14] Brian Klein *et. al*, "B-CAL Progress and Construction Report," Tech. Rep. GlueX Technical Note **333**, 2004.
`http://argus.phys.uregina.ca/cgi-bin/private/DocDB/ShowDocument?docid=333`.

[15] B. Klein and Z. Papandreou, "GlueX BCAL Construction Video Guide," Tech. Rep. GlueX-doc-**1144**, University of Regina, Oct., 2008.
`http://argus.phys.uregina.ca/cgi-bin/private/DocDB/ShowDocument?docid=1144`.

[16] B. Klein, "BCAL Electroneumatic Press Photos," Tech. Rep. GlueX-doc-**1187**, University of Regina, Jan., 2009.
`http://argus.phys.uregina.ca/cgi-bin/private/DocDB/ShowDocument?docid=1187`.

[17] B. Klein, "BCAL Electroneumatic Press Operation Videos," Tech. Rep. GlueX-doc-**1188**, University of Regina, Jan., 2009.
`http://argus.phys.uregina.ca/cgi-bin/private/DocDB/ShowDocument?docid=1188`.

[18] Z. Papandreou and D. Kolybaba, "Barrel calorimeter module construction procedure manual and procedures," Tech. Rep. GlueX-doc-**1573**, University of Regina, Aug., 2010.
`http://argus.phys.uregina.ca/cgi-bin/private/DocDB/ShowDocument?docid=1573`.

[19] E. Smith, "Acceptance Studies for the Production Light Guides of the BCAL," Tech. Rep. GlueX-doc-**1784**, Jefferson Lab, June, 2011.
`http://argus.phys.uregina.ca/cgi-bin/private/DocDB/ShowDocument?docid=1784`.

[20] C. Hutton, "Hall D GlueX Barrel Detector Light Guide A," Drawing D00000-01-07-2057, Jefferson Lab, Mar., 2012.
`https://misportal.jlab.org/jlabDocs/document.seam?id=69828`.

[21] C. Hutton, "Hall D GlueX Barrel Detector Light Guide B," Drawing D00000-01-07-2058, Jefferson Lab, Mar., 2012.
`https://misportal.jlab.org/jlabDocs/document.seam?id=69829`.

[22] C. Hutton, "Hall D GlueX Barrel Detector Light Guide C," Drawing D00000-01-07-2059, Jefferson Lab, Mar., 2012.
`https://misportal.jlab.org/jlabDocs/document.seam?id=69830`.

[23] C. Hutton, "Hall D GlueX Barrel Detector Light Guide D," Drawing D00000-01-07-2060, Jefferson Lab, Mar., 2012.
https://misportal.jlab.org/jlabDocs/document.seam?id=69831.

[24] C. Hutton, "Hall D GlueX Barrel Detector Light Guide E," Drawing D00000-01-07-2061, Jefferson Lab, Mar., 2012.
https://misportal.jlab.org/jlabDocs/document.seam?id=69832.

[25] C. Hutton, "Hall D GlueX Barrel Detector Light Guide F," Drawing D00000-01-07-2062, Jefferson Lab, Mar., 2012.
https://misportal.jlab.org/jlabDocs/document.seam?id=69833.

[26] C. Hutton, "Hall D GlueX Barrel Detector Light Guide G," Drawing D00000-01-07-2063, Jefferson Lab, Mar., 2012.
https://misportal.jlab.org/jlabDocs/document.seam?id=69834.

[27] C. Hutton, "Hall D GlueX Barrel Detector Light Guide H," Drawing D00000-01-07-2064, Jefferson Lab, Mar., 2012.
https://misportal.jlab.org/jlabDocs/document.seam?id=69835.

[28] C. Hutton, "Hall D GlueX Barrel Detector Light Guide J," Drawing D00000-01-07-2065, Jefferson Lab, Mar., 2012.
https://misportal.jlab.org/jlabDocs/document.seam?id=69836.

[29] C. Hutton, "Hall D GlueX Barrel Detector Light Guide K," Drawing D00000-01-07-2066, Jefferson Lab, Mar., 2012.
https://misportal.jlab.org/jlabDocs/document.seam?id=69837.

[30] J. Fochtman, "BCAL Light Guide Installation and Rework," Procedure D00000-01-07-P003, Jefferson Lab, June, 2013.
https://misportal.jlab.org/jlabDocs/document.seam?id=75344.

[31] E. Smith, "Test of wrapping on BCAL light guides," Tech. Rep. GlueX-doc-**1948**, Jefferson Lab, Mar., 2012.
http://argus.phys.uregina.ca/cgi-bin/private/DocDB/ShowDocument?docid=1948.

[32] E. Smith, "Procedure for Gluing Light Guides onto Bcal modules," Traveler GEV12-HALLD-BCAL-GUIDES, Jefferson Lab, Feb., 2013.
https://pansophy.jlab.org/pansophy/Travelers/TRAVELER_INDEX.cfm?project=GEV12&area=GEV12&system=HALLD.

[33] Y. Qiang, C. Zorn, F. Barbosa, and E. Smith, "Radiation Hardness Tests of SiPMs for the JLab Hall D Barrel Calorimeter," *Nucl.Instrum.Meth.* **A698** (2013) 234–241, arXiv:1207.3743 [physics.ins-det].

[34] Hamamatsu, "MPPC Multi-Pixel Photon Counter," data sheet, Jan, 2008.

[35] E. Smith, "Hall D BCAL Readout: Silicon Photomultiplier Array Specification," Specification D00000-01-07-S004 Rev-B, Jefferson Lab, June, 2012.
https://misportal.jlab.org/jlabDocs/document.seam?id=70738.

[36] **GlueX Collaboration** Collaboration, F. Barbosa *et al.*, "Silicon photomultiplier characterization for the GlueX barrel calorimeter," *Nucl.Instrum.Meth.* **A695** (2012) 100–104.

[37] F. Barbosa *et al.*, "Test Results for the 80 First Article Samples of the Hamamatsu Array," Tech. Rep. GlueX-doc-**1777**, Jefferson Lab, June, 2011. `http://argus.phys.uregina.ca/cgi-bin/private/DocDB/ShowDocument?docid=1777`.

[38] O. Soto, R. Rojas, S. Kuleshov, H. Hakobyan, A. Toro, and W. Brooks, "Characterization of novel Hamamatsu Multi Pixel Photon Counter (MPPC) arrays for the GlueX experiment," *Nucl. Instrum. Meth. A* **732** (2013) 431–436.

[39] Y. Qiang, C. Zorn, F. Barbosa, and E. Smith, "Neutron radiation hardness tests of SiPMs," *AIP Conf.Proc.* **1560** (2013) 703–705.

[40] C. Z. E.S. Smith, Y. Qiang, "Status of understanding of Radiation Damage to SiPMs," Tech. Rep. GlueX-doc-**2059**, Jefferson Lab, July, 2010. `http://argus.phys.uregina.ca/cgi-bin/private/DocDB/ShowDocument?docid=2059`.

[41] P. Lightfoot, G. Barker, K. Mavrokoridis, Y. A. Ramachers, and N. Spooner, "Characterisation of a silicon photomultiplier device for applications in liquid argon based neutrino physics and dark matter searches," *JINST* **3** (2008) P10001, `arXiv:0807.3220 [physics.ins-det]`.

[42] Z. Papandreou *et al.*, "Cosmic Ray Tests and Light Output from BCAL," Tech. Rep. GlueX-doc-**1864**, University of Regina and Jefferson Lab, Nov., 2011. `http://argus.phys.uregina.ca/cgi-bin/private/DocDB/ShowDocument?docid=1864`.

[43] J. McKisson, "BCAL Temperature Compensation Calculations," Tech. Rep. GlueX-doc-**2394**, Jefferson Lab, Feb., 2014. `http://argus.phys.uregina.ca/cgi-bin/private/DocDB/ShowDocument?docid=2394`.

[44] E. Anassontzis, P. Ioannou, C. Kourkoumelis, G. Vasileiadis, G. Voulgaris, *et al.*, "Relative gain monitoring of the GlueX calorimeters," *Nucl.Instrum.Meth.* **A738** (2014) 41–49.

[45] Z. Papandreou, B. Leverington, and G. Lolos, "Spectral response of scintillating fibres," *Nucl. Instrum. Meth. A* **596** (2008) 338.

[46] E. Smith, "Scintillation Fibers for the Barrel Calorimeter," Specification D00000-01-07-S001 Rev-A, Jefferson Lab, May, 2008. `https://misportal.jlab.org/jlabDocs/document.seam?id=70607`.

[47] B. Giebrecht *et. al*, "Performance of 'first-article' scintillating fibres for the GlueX Barrel Calorimeter," Tech. Rep. GlueX-doc-**1317**, University of Regina, Dec., 2009. `http://argus.phys.uregina.ca/cgi-bin/private/DocDB/ShowDocument?docid=1317`.

[48] Z. Papandreou, "BCAL Scintillating Fibre Performance: Half Way Milestone," Tech. Rep. GlueX-doc-**1647**, University of Regina, Dec., 2010. `http://argus.phys.uregina.ca/cgi-bin/private/DocDB/ShowDocument?docid=1647`.

[49] Z. Papandreou, "Fibre QA for Shipments 28 and 29," Tech. Rep. GlueX-doc-**1809**, University of Regina, Sept., 2011. `http://argus.phys.uregina.ca/cgi-bin/private/DocDB/ShowDocument?docid=1809`.

[50] Z. Papandreou, "Performance of Kuraray SCSF-78MJ scintillating fibres for the GlueX Barrel Calorimeter," Tech. Rep. GlueX-doc-**1956**, University of Regina, Apr., 2012. `http://argus.phys.uregina.ca/cgi-bin/private/DocDB/ShowDocument?docid=1956`.

[51] A. Baulin *et al.*, "Attenuation length and spectral response of Kuraray SCSF-78MJ scintillating fibres," *Nucl.Instrum.Meth.* **A715** no. 0, (2013) 48 – 55. `http://www.sciencedirect.com/science/article/pii/S016890021300315X`.

[52] T. Beattie *et al.*, "Light yield of Kuraray SCSF-78MJ scintillating fibers for the Gluex barrel calorimeter," *Nucl.Instrum.Meth.* **A767** no. 0, (2014) 245 – 251. `http://http://www.sciencedirect.com/science/article/pii/S0168900214009735`.

[53] Z. Papandreou, B.D. Leverington and Lolos, G.J., "Spectral response of scintillating fibres," Tech. Rep. GlueX-doc-**1072**, University of Regina, June, 2008. `http://argus.phys.uregina.ca/cgi-bin/private/DocDB/ShowDocument?docid=1072`.

[54] Kuraray, "Fiber Spectra from Lot 72," tech. rep., October, 2009. Private communication.

[55] B. Leverington *et al.*, "Performance of the prototype module of the gluex electromagnetic barrel calorimeter," *Nucl.Instrum.Meth.* **A596** no. 3, (2008) 327 – 337. `http://www.sciencedirect.com/science/article/pii/S0168900208013077`.

[56] B.D. Leverington *et al.*, "Performance of the prototype module of the GlueX electromagnetic barrel calorimeter," Tech. Rep. GlueX-doc-**1071**, University of Regina, June, 2008. `http://argus.phys.uregina.ca/cgi-bin/private/DocDB/ShowDocument?docid=1071`.

[57] S. Katsaganis and Z. Papandreou, "Standalone Simulations for the Barrel Calorimeter: Double-Clad Fibres," Tech. Rep. GlueX-doc-**1871**, University of Regina, Dec., 2011. `http://argus.phys.uregina.ca/cgi-bin/private/DocDB/ShowDocument?docid=1871`.

[58] G. Koleva, "BCAL Prototype Beam Test at the M11 Channel at TRIUMF," Master's thesis, University of Regina, 2006.

[59] R. Jones, 2001. The HDGeant Monte Carlo Program.

[60] **Particle Data Group** Collaboration, J. Beringer *et al.*, "Review of Particle Physics (RPP)," *Phys.Rev.* **D86** (2012) 010001.

[61] Z. Papandreou, "BCAL Calorimetry Response," Tech. Rep. GlueX-doc-**840**, University of Regina, Jan., 2008. `http://argus.phys.uregina.ca/cgi-bin/private/DocDB/ShowDocument?docid=840`.

[62] A. Dzierba, Z. Papandreou *et al.*, "BCAL Facts: What we know and how we know," Tech. Rep. GlueX-doc-**842**, University of Indiana and University of Regina, July, 2007. `http://argus.phys.uregina.ca/cgi-bin/private/DocDB/ShowDocument?docid=842`.

[63] B. Leverington, "BCAL Sampling Fraction ...," Tech. Rep. GlueX-doc-**827**, University of Regina, Jan., 2007. `http://argus.phys.uregina.ca/cgi-bin/private/DocDB/ShowDocument?docid=827`.

[64] M. Antonelli, G. Barbiellini, S. Bertolucci, C. Bini, C. Bloise *et al.*, "The electromagnetic calorimeter of the KLOE experiment at DANE," *Nucl.Instrum.Meth.* **A379** (1996) 511–514.

[65] I. S. A. Semenov, "Photon-Neutron Separation with BCAL," Tech. Rep. GlueX-doc-**1865**, Jefferson Lab, Nov., 2011. `http://argus.phys.uregina.ca/cgi-bin/private/DocDB/ShowDocument?docid=1865`.

[66] G. Lolos *et al.*, "Proposal for Beam Test of a GlueX Barrel Calorimeter Prototype in Hall B," Tech. Rep. GlueX-doc-**1900**, Jefferson Lab, Mar., 2012. `http://argus.phys.uregina.ca/cgi-bin/private/DocDB/ShowDocument?docid=1900`.

[67] T. Beattie and J. Stevens, "Boosted Decision Tree for the BCAL Cluster Recontruction," Tech. Rep. GlueX-doc-**2550**, University of Regina and MIT, 2014. `http://argus.phys.uregina.ca/cgi-bin/private/DocDB/ShowDocument?docid=2550`.

[68] Y. Van Haarlem, C. Meyer, F. Barbosa, B. Dey, D. Lawrence, V. Razmyslovich, E. Smith, G. Visser, *et al.*, "The GlueX Central Drift Chamber: Design and Performance," *Nucl.Instrum.Meth.* **A622** (2010) 142–156, `arXiv:1004.3796 [nucl-ex]`.

[69] S. Roth and R. Schumacher, "A computer-controlled tension monitoring system for drift chamber wires," *Nucl.Instrum.Meth.* **A369** (1996) 215–221.

[70] R. Veenhof, *The GARFIELD Program, Simulation of Gaseous Detectors*. CERN, 1984. `http://garfield.web.cern.ch/garfield/`.

[71] H. C. Fenker, J. Thomas, M. Brooks, D. Lee, and G. Mills, "Precision interpolating pad chambers," *Nucl.Instrum.Meth.* **A367** (1995) 285–289.